

# **Statics and Dynamics Simulation of a Multi-Tethered Aerostat System**

by

**Xiaohua Zhao**

**B.Sc., Nanjing University of Aeronautics & Astronautics, 1994**

**A Thesis Submitted in Partial Fulfillment of the  
Requirements for the Degree of**

**MASTER OF APPLIED SCIENCE**

**in the Department of Mechanical Engineering**

© Xiaohua Zhao, 2004

University of Victoria

All right reserved. This thesis may not be reproduced in whole or in part, by photocopy or other means, without the permission of the author.

Supervisor: Dr. M. Nahon

## **Abstract**

A new radio telescope composed of an array of antennas is under development at the National Research Council. Each antenna includes a large scale multi-tethered aerostat system to hold the telescope receiver at the reflector focus. This receiver is located at the confluence point of the tethers.

Starting from a previously developed dynamics simulation of the triple-tethered aerostat system, an existing statics model of the same system is incorporated into the simulation to provide an initial equilibrium condition for the dynamics. A spherical aerostat is used in both models. The two models show a very good match with each other after being merged together. This combined computer model is further developed to study the use of six tethers and the use of a streamlined aerostat instead of a spherical one. In the case of the six-tethered system, two topics were investigated: using the six tethers to control the position of the airborne receiver only; and using the six tethers to control the orientation of the receiver as well as its position. A streamlined aerostat is also modelled by a component breakdown method and incorporated into the triple-tethered system to replace the spherical one.

The main findings from the simulation results are as follows: (1) the six-tethered system with reductions in the tether base radius and the tether diameter exhibited increased stiffness compared to the triple-tethered system when used to control the receiver position only; (2) the six-tethered system showed difficulty achieving

satisfactory control for both the position and orientation of the receiver; (3) the streamlined aerostat showed no oscillations typical of a spherical one but the system requires more power to control in the presence of wind turbulence.

## Table of Contents

<b>Abstract .....</b>	<b>ii</b>
<b>Table of Contents .....</b>	<b>iv</b>
<b>List of Tables .....</b>	<b>vii</b>
<b>List of Figures.....</b>	<b>viii</b>
<b>Acknowledgements .....</b>	<b>x</b>
<b>Dedication.....</b>	<b>xii</b>
<b>Chapter 1 Introduction.....</b>	<b>1</b>
1.1 Background.....	1
1.2 Related Work .....	5
1.3 Research Focus .....	8
<b>Chapter 2 Kinematics .....</b>	<b>10</b>
2.1 Reference Frames.....	10
2.2 Translational Kinematics .....	12
2.3 Orientations and Rotational Transformations .....	13
2.3.1 The $Z$ - $Y$ - $X$ Euler Angle Set and its Transformations .....	14
2.3.2 The $Z$ - $Y$ - $Z$ Euler Angle Set and its Transformations .....	16
<b>Chapter 3 Statics .....</b>	<b>18</b>
3.1 Model Overview and Problem Description .....	18
3.1.1 The Aerostat Model .....	19
3.1.2 The Payload Platform Model .....	20
3.1.3 The Cable Model.....	20
3.2 Fitzsimmons' Statics Solution .....	22
3.3 Implementation and Modifications of Fitzsimmons' Solution .....	36
3.4 Verification of the Statics Model.....	38

<b>Chapter 4 Six-Tethered System .....</b>	<b>42</b>
4.1 Dynamics of the Triple-Tethered System .....	42
4.2 Redundantly Actuated System .....	47
4.2.1 Actuation Redundancy .....	48
4.2.2 Redundancy in Statics .....	49
4.2.3 Constrained Optimization Problem .....	50
4.2.4 Nonlinear Optimizer CFSQP .....	50
4.2.5 Implementation in the Statics .....	52
4.2.6 Dynamics of the Six-Tethered System .....	55
4.2.7 Statics Results and Verification .....	55
4.2.8 Optimization Results and Discussion .....	57
4.2.9 Dynamics Results and Discussion .....	64
4.3 Determinate System .....	68
4.3.1 Purpose .....	69
4.3.2 The 6-DOF Payload Platform Model .....	69
4.3.2.1 Statics .....	70
4.3.2.2 Dynamics .....	71
4.3.3 Results and Discussion .....	74
<b>Chapter 5 Incorporation of a Streamlined Aerostat .....</b>	<b>83</b>
5.1 Vehicle Introduction .....	83
5.2 Modelling the TCOM 71M Aerostat .....	86
5.2.1 Reference Frames .....	87
5.2.2 Scaled Parameters .....	88
5.2.2.1 Moments and Products of Inertia .....	89
5.2.2.2 The Center of Mass .....	91
5.2.2.3 The Leash Attachment Point .....	91
5.2.3 Estimated Center of Buoyancy .....	92
5.2.4 Aerostat Component Breakdown .....	93
5.2.4.1 The Hull .....	93
5.2.4.2 The Fins .....	97

5.2.4.3	The Bulge.....	98
5.2.5	Added Mass and Moments.....	99
5.3	Model Validation .....	101
5.4	Implementation and Incorporation.....	103
5.4.1	Statics .....	104
5.4.2	Dynamics .....	106
5.5	Results & Discussions.....	108
<b>Chapter 6</b>	<b>Conclusions.....</b>	<b>116</b>
6.1	Conclusions.....	116
6.2	Future Work.....	118
<b>Bibliography</b>	<b>.....</b>	<b>121</b>

## List of Tables

Table 3.1 Spherical aerostat properties.....	19
Table 3.2 Cable properties .....	21
Table 3.3 Conditions of simulation cases .....	39
Table 4.1 Parameter changes .....	55
Table 4.2 Objective functions for no-wind analysis .....	57
Table 4.3 Case number definitions for Figure 4.7 .....	61
Table 4.4 Payload position errors for the redundantly actuated system .....	65
Table 4.5 Simulation conditions .....	74
Table 5.1 The TCOM 71M aerostat parameters [17], [36].....	85
Table 5.2 Balloon properties [39] .....	88
Table 5.3 Ratios between the two vehicles .....	90
Table 5.4 Moments and product of inertia.....	90
Table 5.5 Parameters of the fins and the bulge.....	99
Table 5.6 Aerostat pitch angles under different conditions .....	105
Table 5.7 Payload position errors .....	109

## List of Figures

Figure 1.1 An example of present-day steerable telescope.....	2
Figure 1.2 LAR Portrait View [5].....	3
Figure 1.3 LAR Concept [7].....	4
Figure 2.1 Reference frames .....	11
Figure 2.2 The body-fixed frame for a streamlined aerostat .....	12
Figure 2.3 Z-Y-X Euler Angles [25].....	14
Figure 3.1 Cable segment model (statics).....	21
Figure 3.2 Flowchart of statics solution by Fitzsimmons.....	24
Figure 3.3 The strained cable profile .....	25
Figure 3.4 Tethers in a 3-D space .....	27
Figure 3.5 Tether segment analysis .....	29
Figure 3.6 Tether profile calculation (Block D in Figure 3.2).....	30
Figure 3.7 Approximation used in tether analysis .....	32
Figure 3.8 Leash analysis.....	33
Figure 3.9 Wind models.....	37
Figure 3.10 Errors of the CP when using statics solution as the initial states .....	40
Figure 4.1 Cable segment model (dynamics) .....	43
Figure 4.2 The tethered aerostat system model in 2-D [24] .....	44
Figure 4.3 Controller 2-D illustration [24] .....	46
Figure 4.4 Matching simulations for the six-tethered spherical aerostat system .....	56
Figure 4.5 Tether tensions in statics using different objective functions .....	59
Figure 4.6 Results for different objective functions, $\theta_{za} = \theta_{za} = 0$ .....	60
Figure 4.7 Dynamics simulation results of the payload position using different objective functions for the statics initial condition.....	62
Figure 4.8 Dynamics simulation results of the tether tensions using different objective functions for the statics initial condition.....	63
Figure 4.9 Payload motion for $\theta_{za} = \theta_{az} = 0$ .....	66



Figure 4.10 Tether tension for $\theta_{za} = \theta_{az} = 0$ .....	66
Figure 4.11 Payload motion for $\theta_{za} = 60^\circ$ , $\theta_{az} = 0$ .....	67
Figure 4.12 Tether tension for $\theta_{za} = 60^\circ$ , $\theta_{az} = 0$ .....	67
Figure 4.13 The Airborne platform view [5] .....	68
Figure 4.14 2-D illustration of the winch controller .....	73
Figure 4.15 Payload platform orientation .....	76
Figure 4.16 Payload position error.....	77
Figure 4.17 Tether tensions.....	79
Figure 4.18 Top view of the six-Tether configuration.....	80
Figure 5.1 The TCOM 71M aerostat [35].....	84
Figure 5.2 The structure of the TCOM 71M aerostat .....	87
Figure 5.3 Reference frames of the aerostat .....	87
Figure 5.4 Tethered balloon layout [39] .....	89
Figure 5.5 Modelling the hull .....	94
Figure 5.6 Center of pressure of the hull .....	96
Figure 5.7 Center of pressure of the fin .....	98
Figure 5.8 Normal force coefficient and pitching moment coefficient about the nose of the TCOM 71M.....	102
Figure 5.9 Aerodynamic model of [36] compared with wind tunnel data [36] .....	103
Figure 5.10 External forces applied to the aerostat.....	107
Figure 5.11 Aerostat translational motion for $\theta_{za} = \theta_{az} = 0$ .....	110
Figure 5.12 Aerostat rotational motion for $\theta_{za} = \theta_{az} = 0$ .....	110
Figure 5.13 Payload position error for $\theta_{za} = \theta_{az} = 0$ .....	111
Figure 5.14 Tether tensions for $\theta_{za} = \theta_{az} = 0$ .....	111
Figure 5.15 Aerostat translational motion for $\theta_{za} = 60^\circ$ , $\theta_{az} = 0$ .....	112
Figure 5.16 Aerostat rotational motion for $\theta_{za} = 60^\circ$ , $\theta_{az} = 0$ .....	112
Figure 5.17 Payload position error for $\theta_{za} = 60^\circ$ , $\theta_{az} = 0$ .....	113
Figure 5.18 Winch tensions for $\theta_{za} = 60^\circ$ , $\theta_{az} = 0$ .....	113

## Acknowledgements

I would like to thank many people who helped me fulfill my M.A.Sc. study. First, and above all, Dr. Meyer Nahon for his enthusiastic and extraordinary supervision and guidance during these years. I have learnt a great deal from him. I would also express my heartfelt gratitude to Dr. Zuomin Dong, Dr. Brad Buckham and Dr. Wu-Sheng Lu for being in my thesis committee and offering their observations and suggestions. Their efforts added new insights into my work. I would like to extend my sincere appreciation to Dr. Joeleff Fitzsimmons for his contribution to my work.

I am very grateful to Prof. Yuncheng Xia, Prof. Yongzhang Shen, Prof. Daiye Lin and Prof. Zhenqiu Yang. Not only did they teach me academic knowledge during my years in Nanjing, but also taught me to be a better person by their own examples, and gave me fatherly moral support ever since I lost my father in 1998.

I would also like to thank Juan Carretero, Gabriele Gilardi, Casey Lambert, Sheng Wan, Rong Zheng, Xiang Diao, Lu Liu and Ruolong Ma, Andy Yu and Kevin Deane-Freeman for sharing their knowledge and helping on many occasions. Thanks to Lei Hong, Nina Ni, Huiyan Zhou, Juan Liu, Shaun Georges and Richard Barazzuol for cheering me on and helping me get through hard times. Special thanks to Manjinder Mann for his immense patience and support.

I am forever indebted to my parents. My father, Chuanyuan Zhao, had always encouraged and fully supported me. I will always have him in my heart. As well, my mother has always been extremely patient and supportive in all my endeavors. Their love

has always been the greatest inspiration for me. I am also thankful to my brother Bo and sister Xiaoyu for their constant support.

Apart from the people mentioned above, many others have helped along the way. I cannot name all here, but I remain indebted to them.

My deep thanks to all for making my life so much fuller!

## **Dedication**

To those who have loved me so much...

# **Chapter 1 Introduction**

## **1.1 Background**

The latest developments in astronomy have motivated astronomers worldwide to plan for the next generation of radio telescopes. It is now believed that a new radio telescope with unprecedented sensitivity will be needed to study the earliest universe. This proposed revolutionary radio telescope will have an effective collecting area of one million square metres, much greater than that of the largest radio telescope in service. The astronomy community around the globe has aimed to build such a radio telescope in the next decade. This international project is known as the Square Kilometre Array (SKA) [1]. A Memorandum of Agreement on this international SKA project has been signed by a number of organizations from several countries including Australia, Canada, China, India, the Netherlands, and the U.S.A. [2].

The SKA will consist of an array of stations, spread over an area one thousand kilometres in diameter. Each station of the array will be a telescope in its own right, with an aperture up to 200 metres.

The size of each telescope will be much larger than the present-day fully steerable radio telescopes (Figure 1.1 shows the 25 m dishes of the Very Large Array in New

Mexico [3]). For this reason, it would not be cost effective to build the Square Kilometre Array with conventional technology. A new means must be established to construct a very large aperture radio telescope like this. Research and development activities are ongoing at several international centres. In Canada, the Large Adaptive Reflector (LAR) approach is under study as a solution [4]. This development work is funded by National Research Council, Canada (NRCC), and coordinated by Dominion Radio Astrophysical Observatory (DRAO) with collaborators in universities and industry [5].

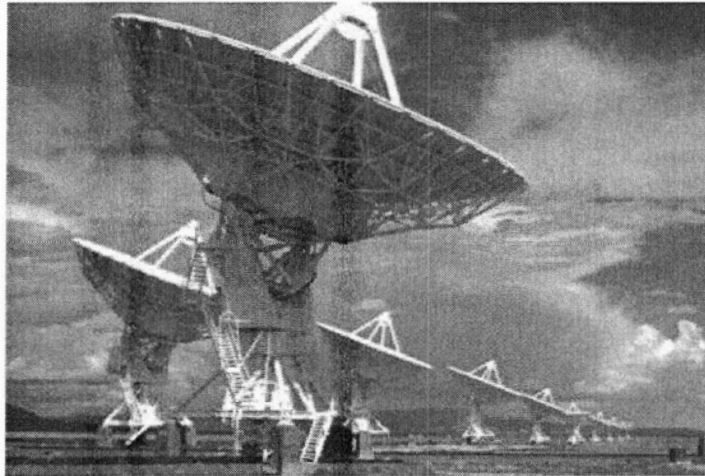


Figure 1.1 An example of present-day steerable telescope  
(The Very Large Array of fully steerable telescopes in New Mexico [3])

The LAR, proposed by Legg of NRCC's Herzberg Institute of Astrophysics (HIA) and shown diagrammatically in Figure 1.2, is a long focal-length (about 500 metres), large diameter (about 200 metres) parabolic reflector which requires an airborne platform to support the focal receiver [4]. An array of about 50 LARs would be used to build the SKA. The reflector is composed of many flat panels, which are supported by the

ground. The shape of the reflecting surface can be adjusted by actuators under the panels. Steering is realized by adjusting the shape of the reflector and the position of the airborne platform where the receiver feed is located. A key challenge to implement the LAR design is to accurately control the position of the airborne platform. This subsystem is the focus of this thesis. The receiver's position will be controlled by three or more cables and winches, and an aerostat will be used to provide lifting force for the system.

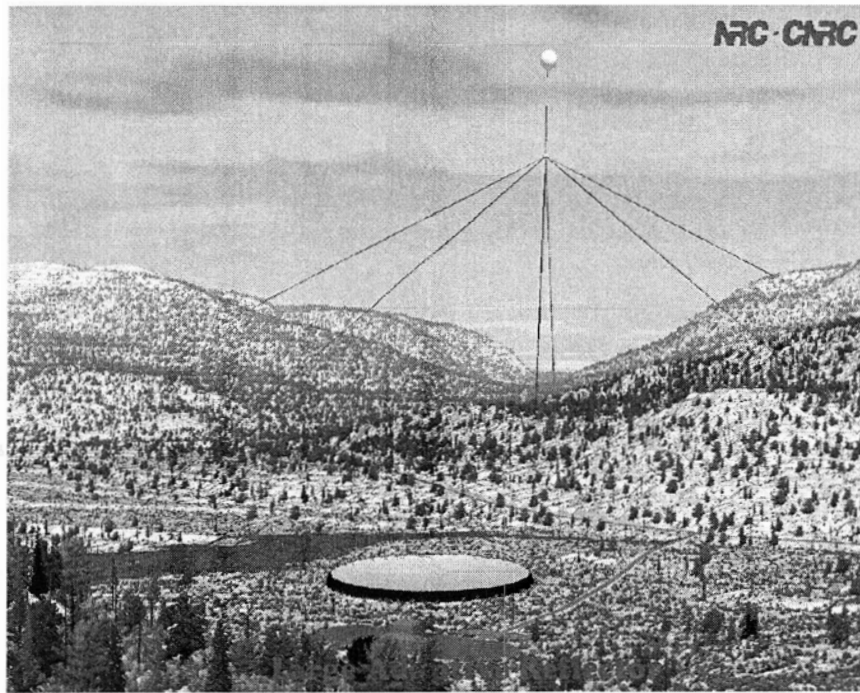


Figure 1.2 LAR Portrait View [5]

Using tensioned cables to support the airborne platform places this system in a class of structures known as tension structures. The advantages of such a system include [6]:

- 1) The structure has a high ratio of payload to structural weight;

- 2) The cables are highly tensioned by the aerostat lift at static equilibrium. This stiffens the structure, reduces deflection due to perturbations, and stabilizes the structure;
- 3) The structure is easily reconfigurable by changing the cable lengths;
- 4) The environmental loads are efficiently carried by direct tensile stress, without bending.

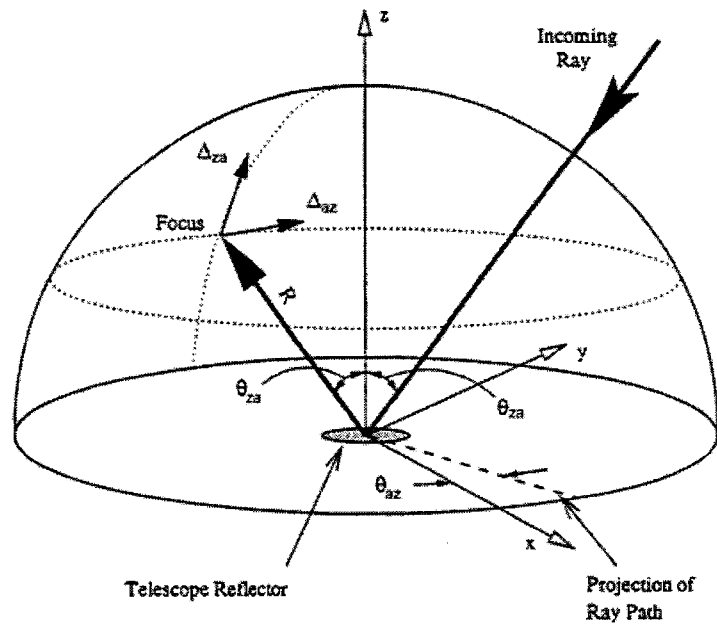


Figure 1.3 LAR Concept [7]

Figure 1.3 shows the geometry of the LAR. The airborne platform will be at the focus of the reflector. The focal plane is the  $\Delta_{za}$ - $\Delta_{az}$  plane.  $\theta_{za}$  is the zenith angle of the airborne platform, and  $\theta_{az}$  is its azimuth angle.  $R$  is the distance from the center of



reflector to the focus, and would vary with zenith and azimuth angles. This study focuses on the performance of the system with a goal of keeping the airborne platform positioned on the surface of a hemisphere of constant radius  $R = 500$  m. Figure 1.2 illustrates the portrait view of such a radio telescope antenna system with six tethers and a spherical aerostat.

A computer simulation of this system will be presented to study the statics and dynamics of the system. Considering the scale of the system, a computer simulation is an inexpensive and valuable tool to perform preliminary study of the system when compared to building prototypes. It can provide good insight into the behaviour of the system and help with the system design.

## 1.2 Related Work

Analysing this novel multi-tethered system requires a consideration of the statics and dynamics of cables and aerostats. Cable structures are considered to be difficult to analyze because of their nonlinear behaviour. For most realistic problems, it is typically not considered practical to obtain statics, dynamics and displacement solutions using a continuous cable model. For this reason the cables are usually analysed numerically using discrete models such as lumped mass or rod models. A rod model consists of rods connected by frictionless hinges at the endpoints to form a chain [8]. A lumped mass model, originally proposed by Walton and Polacheck [9], consists of point masses connected by weightless rigid or flexible links [9] [10] [11] [12]. Forces acting on each rod or segment are applied at the endpoints to set up motion equations in three-dimension. The motion of the system is obtained by integrating the motion equations.

Both modelling methods are widely used in study of cable systems. Sanders [8] showed a finite difference formulation to develop the discretized equations of motion for a towed system. Kamman et al. [10], [12], and Buckham, et al. [11] employed lumped mass or lumped parameter models in their simulation of towed cable systems. These results showed simulation results that were qualitatively and quantitatively reasonable. Lumped mass modelling is the method used in this work.

Since the decision of whether to use a streamlined or spherical aerostat for LAR has not yet been finalized, both types of aerostats are studied in this work. The dynamics of a spherical aerostat are straightforward because of its uniform shape. It is more difficult to analyze the dynamics characteristics of a streamlined aerostat.

The analysis of the dynamics of aerostats and airships requires knowledge of aerodynamic forces and moments applied on an aerostat or airship. Aerodynamic forces and moments of the hull of an aerostat or airship can be calculated based on its geometry and flow characteristics [13]. This method of analysis was developed by Allen and Perkins [14] from Munk's normal-force and potential-flow equations for airship bodies [15]. Jones and DeLaurier based their estimation techniques of aerostats and airships' aerodynamic properties [13] on a semiempirical airship model that included a consideration of the hull-fin mutual interference factors and added mass for greater accuracy.

Tethered aerostat systems have received limited attention. Previous studies have been concerned mainly with single-tethered systems. Jones and Schroeder presented some dynamic simulations of tethered/moored streamlined aerostat system [16], [17], [18], which were mainly focused on the verification of aerodynamic characteristics of the

streamlined aerostat model, with no discussion of the tether's dynamics or closed loop control of the tethered system.

Some work was performed in the early 70's by the US Air Force, comparing a multi-tethered aerostat system to a single tethered arrangement [19], [20]. They found the multi-tethered system greatly reduced the motion dispersions of the system.

Some investigations have been carried out during the past a few years on tethered spheres. Results demonstrate that a tethered sphere will oscillate strongly at a saturation amplitude of close to two diameters peak-to-peak in a steady fluid flow. The oscillations induce an increase in drag and tether angle on the order of around 100% over what is predicted using steady drag measurements. The in-line oscillations vibrate at twice the frequency of the transverse motion [21], [22].

In Canada, scientists and engineers from research institutes, universities and industry are working together to develop the LAR concept. Veidt, Dewdney, and Fitzsimmons of NRCC's HIA, worked on the steady-state stability analysis of the multi-tethered LAR aerostat platform [7], [23]. Their steady-state analysis results showed that this tethered aerostat system will operate reliably in moderate weather condition. Nahon later performed a dynamics simulation of the triple-tethered spherical aerostat system [24]. The numerical simulation results presented there indicate that the spherical aerostat system can be accurately controlled in the presence of disturbances due to turbulence. These encouraging results have led to this work, which is a further study of the multi-tethered aerostat system. It is worth noting that Fitzsimmons' work is used as the basis for the initial determination of equilibrium state in this study. Detailed descriptions of this

will be given in Chapter 3. As well, Nahon's work is used as the basis for the dynamics work in this study, and this will be further discussed in Chapter 4.

### 1.3 Research Focus

The studies presented in this work are intended to provide preliminary insight into the LAR system, and thus help the design of the system.

The specific topics covered are an analysis of the six-tethered system with a spherical aerostat and triple-tethered system with a streamlined aerostat. In the six-tethered system case, two operational modes are studied: redundantly-actuated and determinate. In the redundantly-actuated mode, the six main tethers are used to control the payload position only; in the determinate mode, the six tethers are used to control both the position and orientation of the payload platform. Statics analyses are used to provide initial states for the dynamics simulation. Dynamics simulations are carried out for different system configurations.

Studying the dynamics of this complex system involves transforming quantities of interest between different reference frames. Chapter 2 explains the relationship between frames and describes the transformations used in this work.

Chapter 3 discusses the statics analysis adopted from Fitzsimmons and the changes made to it in order to be incorporated into the dynamics work.

The six-tethered system is covered in Chapter 4. We first introduce Nahon's dynamics model of the triple-tethered system with a spherical aerostat. Then the redundantly-actuated six-tethered system is discussed and a variety of objective functions are evaluated to solve the underdetermined statics problem. Dynamics simulation results

are presented as well. In addition, we study the determinate six-tethered system in which the position and orientation of the payload platform are controlled by changing the length of the tethers. Some results are shown to illustrate the findings. It is worth mentioning that the vortex-induced oscillations typical of the spherical aerostat are not included in the spherical aerostat model.

In Chapter 5, we deal with the incorporation of a streamlined aerostat to replace the spherical one in the triple-tethered system. Modelling of the streamlined aerostat is covered and validation results are presented. Simulation results are then discussed.

Finally, Chapter 6 gives an overview the work accomplished. Conclusions and recommendations for future work are presented there.

## Chapter 2 Kinematics

When formulating mechanics problems, a number of reference frames must be used to specify relative positions and velocities, components of vectors (e.g. forces, velocities, accelerations). As well, formulae for transforming quantities of interest from one frame to another must be available.

### 2.1 Reference Frames

An inertial reference frame is essential to dynamic problems, while other frames are usually also defined for the convenience of the problem at hand. In this study, the reference frames include an inertial frame and a number of body-fixed frames. All frames used are right-handed.

The inertial reference frame,  $O_I X_I Y_I Z_I$ , shown in Figure 2.1, is fixed to the ground with its origin  $O_I$  at the center of the reflector, and  $O_I Z_I$  directed vertically up.  $O_I X_I Y_I$  defines the horizontal plane, with  $O_I X_I$  pointing to the base of the first tether and  $O_I Y_I$  defined to complete a right-handed coordinate system.

The body-fixed frames are defined to describe motions of bodies such as tether elements, the payload platform, and the aerostat in the system. Figure 2.1 illustrates

body-fixed frames for various moving bodies. Frame  $O_{ti}X_{ti}Y_{ti}Z_{ti}$  is attached to tether element  $i$ , while frame  $O_aX_aY_aZ_a$  moves with the aerostat, and frame  $O_pX_pY_pZ_p$  is embedded in the payload platform.

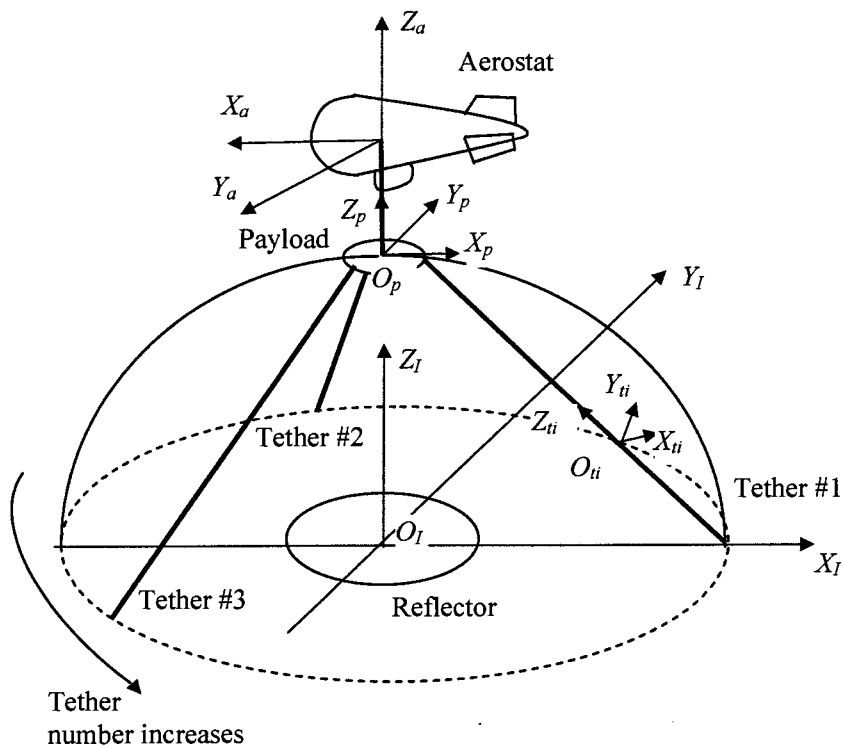


Figure 2.1 Reference frames

Frame  $O_{ti}X_{ti}Y_{ti}Z_{ti}$  is the body-fixed frame for tether  $i$  element, where  $i = 1, \dots, n_t$  where  $n_t$  is the total number of tether elements.  $O_{ti}$  is located at the lower end of the element, axes  $O_{ti}X_{ti}$  and  $O_{ti}Y_{ti}$  are the local normal and binormal direction, and axis  $O_{ti}Z_{ti}$  is tangent to the element.

Frame  $O_aX_aY_aZ_a$ , when used with a spherical aerostat, is defined such that when the aerostat is in its equilibrium condition directly above the center of reflector  $O_I$ , the axes

$O_a X_a$ ,  $O_a Y_a$  and  $O_a Z_a$  are aligned with those of the inertial frame.

When a streamlined aerostat is used, the body-fixed frame is defined as shown in Figure 2.2, with its origin at the center of mass of the aerostat. The  $X_a$ -axis points forward, the  $Y_a$ -axis points left and the  $Z_a$ -axis points upwards. Also shown in Figure 2.2 are the components of the aerostat's angular velocity  $p$ ,  $q$ ,  $r$ .

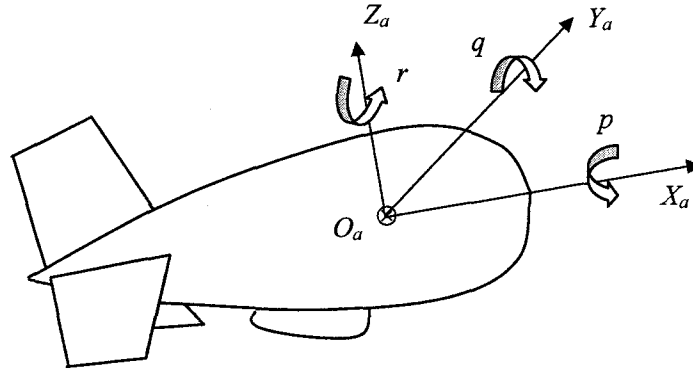


Figure 2.2 The body-fixed frame for a streamlined aerostat

The payload platform's body-fixed frame  $O_p X_p Y_p Z_p$  has its origin at the center of mass,  $O_p Z_p$  is directed upwards and perpendicular to the disk plane  $O_p X_p Y_p$ . Axes  $O_p X_p$  and  $O_p Y_p$  are aligned with  $O_I X_I$  and  $O_I Y_I$  respectively, when the disk is in its equilibrium configuration above the center of reflector as shown in Figure 2.1.

## 2.2 Translational Kinematics

The position of an object is usually expressed in terms of the relation of a particular reference point on the object to the origin of a reference frame. For example, the position of the payload platform is expressed by the position vector of its center of mass with



respect to the origin of the inertial frame  $O_I X_I Y_I Z_I$  (Figure 2.1), and expressed as components in the inertial frame, i.e.,

$${}^I \mathbf{r} = \begin{bmatrix} {}^I r_x \\ {}^I r_y \\ {}^I r_z \end{bmatrix}$$

Similarly, position vectors expressed in the inertial frame are used to denote the positions of the aerostat, and all the cable nodes. In some cases, it is more convenient to express the position of an object in a local body-fixed frame. For example, the position of the above-mentioned point on the payload platform may be expressed in the aerostat body-fixed frame as

$${}^B \mathbf{r} = \begin{bmatrix} {}^B r_x \\ {}^B r_y \\ {}^B r_z \end{bmatrix}$$

The leading superscript ' $B$ ' stands for the *Body*-fixed frame.

The translational velocities can be naturally expressed by the time derivatives of position vectors. As well, the translational accelerations would be represented by second time derivatives of the position vectors.

## 2.3 Orientations and Rotational Transformations

The orientation of one reference frame with respect to another can be represented using Euler angles. For convenience, two sets of angles,  $Z$ - $Y$ - $X$  and  $Z$ - $Y$ - $Z$  Euler angles [25], are chosen to describe the orientations. The orientation of the body-fixed frame of the payload platform is represented by a set of  $Z$ - $Y$ - $Z$  Euler angles. In all other cases, a  $Z$ - $Y$ - $X$  Euler angle set is used.

### 2.3.1 The Z-Y-X Euler Angle Set and its Transformations

The Z-Y-X Euler angles describing the orientation of a body-fixed frame with respect to the inertial frame are obtained by the following three rotations (Figure 2.3), starting with a frame coincident with the inertial frame:

- 1) A rotation by  $\psi$  about the Z-axis;
- 2) A rotation by  $\theta$  about the Y-axis which results from the previous rotation;
- 3) A rotation by  $\phi$  about the X-axis resulting from the last rotation.

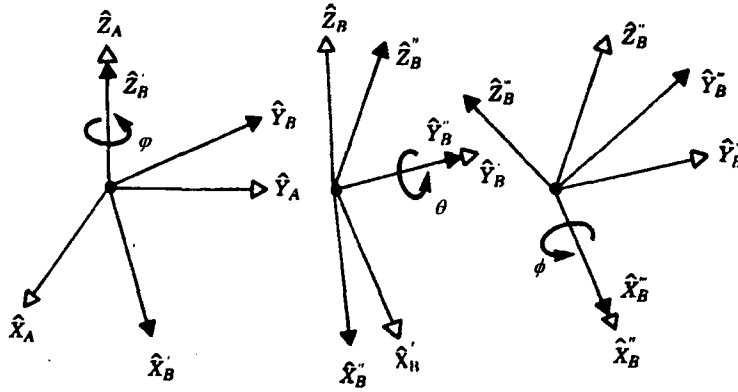


Figure 2.3 Z-Y-X Euler Angles [25]

The resulting rotation matrix which maps vector components in the body-fixed frame to components in the inertial frame is as follows:

$${}^I_B \mathbf{T}_{ZYX} = \begin{bmatrix} \cos \theta \cos \psi & \sin \phi \sin \theta \cos \psi - \cos \phi \sin \psi & \cos \phi \sin \theta \cos \psi + \sin \phi \sin \psi \\ \cos \theta \sin \psi & \sin \phi \sin \theta \sin \psi + \cos \phi \cos \psi & \cos \phi \sin \theta \sin \psi - \sin \phi \cos \psi \\ -\sin \theta & \sin \phi \cos \theta & \cos \phi \cos \theta \end{bmatrix} \quad (2.1)$$

A feature of rotation matrices is that they are orthogonal, and the inverse is therefore

simply given by the transpose.

$${}^B\mathbf{T}_{ZYX}^{-1} = {}^I\mathbf{T}_{ZYX}^T$$

When applied to the tether element local frame, the Euler angle  $\psi$  is set to zero since the torsion of the tether is not considered in the tether model. We then get a simpler form of the rotation matrix

$${}^I\mathbf{T}_{ZYX} = \begin{bmatrix} \cos\theta & \sin\phi\sin\theta & \cos\phi\sin\theta \\ 0 & -\cos\phi & -\sin\phi \\ -\sin\theta & \sin\phi\cos\theta & \cos\phi\cos\theta \end{bmatrix} \quad (2.2)$$

Transformations between the angular velocities  $p, q, r$  (see Figure 2.2) and time derivatives of Euler angles  $\dot{\theta}, \dot{\phi}$  and  $\dot{\psi}$  are necessary for the dynamics analysis. When employing a Z-Y-X Euler angle set, the kinematic relations are:

$$\dot{\phi} = p + (\sin\phi\tan\theta)q + (\cos\phi\tan\theta)r$$

$$\dot{\theta} = (\cos\phi)q - (\sin\phi)r$$

$$\dot{\psi} = (\sin\phi\sec\theta)q + (\cos\phi\sec\theta)r$$

Or, in matrix form

$$\begin{bmatrix} \dot{\phi} \\ \dot{\theta} \\ \dot{\psi} \end{bmatrix} = \begin{bmatrix} 1 & \sin\phi\tan\theta & \cos\phi\tan\theta \\ 0 & \cos\phi & -\sin\phi \\ 0 & \sin\phi/\cos\theta & \cos\phi/\cos\theta \end{bmatrix} \begin{bmatrix} p \\ q \\ r \end{bmatrix} \quad (2.3)$$

Based on this transformation matrix, we see that this Euler angle set becomes degenerate when  $\theta = 90^\circ$ . However, this condition is never reached in our simulations.

It should be noted that this transformation is not orthogonal. The corresponding inverse transformation is as follows:

$$\begin{bmatrix} p \\ q \\ r \end{bmatrix} = \begin{bmatrix} 1 & 0 & -\sin \theta \\ 0 & \cos \phi & \cos \theta \sin \phi \\ 0 & -\sin \phi & \cos \theta \cos \phi \end{bmatrix} \begin{bmatrix} \dot{\phi} \\ \dot{\theta} \\ \dot{\psi} \end{bmatrix} \quad (2.4)$$

### 2.3.2 The Z-Y-Z Euler Angle Set and its Transformations

The Z-Y-Z Euler angles are obtained by the following three rotations, starting with a frame coincident with the inertial frame:

- 1) A rotation by  $\alpha$  about the Z-axis;
- 2) A rotation by  $\beta$  about the Y-axis which results from the previous rotation;
- 3) A rotation by  $\gamma$  about the Z-axis resulting from the last rotation.

The resulting rotation matrix which maps vector components in the body-fixed frame to components in the inertial frame is as follows:

$${}^I_B \mathbf{T}_{ZYZ} = \begin{bmatrix} \cos \alpha \cos \beta \cos \gamma - \sin \alpha \sin \gamma & -\cos \alpha \cos \beta \sin \gamma - \sin \alpha \cos \gamma & \cos \alpha \sin \beta \\ \sin \alpha \cos \beta \cos \gamma + \cos \alpha \sin \gamma & -\sin \alpha \cos \beta \sin \gamma + \cos \alpha \cos \gamma & \sin \alpha \sin \beta \\ -\sin \beta \cos \gamma & \sin \beta \sin \gamma & \cos \beta \end{bmatrix} \quad (2.5)$$

The transformations between the angular velocities in the body-fixed frame and the time derivative of Euler angles are as follows:

$$\begin{bmatrix} \dot{\alpha} \\ \dot{\beta} \\ \dot{\gamma} \end{bmatrix} = \begin{bmatrix} -\cos \gamma / \sin \beta & \sin \gamma / \sin \beta & 0 \\ \sin \gamma & \cos \gamma & 0 \\ \cos \gamma / \tan \beta & -\sin \gamma / \tan \beta & 1 \end{bmatrix} \begin{bmatrix} p \\ q \\ r \end{bmatrix} \quad (2.6)$$

and

$$\begin{bmatrix} p \\ q \\ r \end{bmatrix} = \begin{bmatrix} -\sin \beta \cos \gamma & \sin \gamma & 0 \\ \sin \beta \sin \gamma & \cos \gamma & 0 \\ \cos \beta & 0 & 1 \end{bmatrix} \begin{bmatrix} \dot{\alpha} \\ \dot{\beta} \\ \dot{\gamma} \end{bmatrix} \quad (2.7)$$

The Z-Y-Z Euler angles were used for the payload platform because they are well suited to its movements: the first two angles represent “pointing” of the axis of symmetry of the platform, and the last angle represents rotations about that axis. This Euler angle set becomes degenerate when  $\beta = 0$ , which is in the system’s workspace. To avoid this condition, we used  $\beta = 10^{-4}$  deg instead for those cases.

## **Chapter 3 Statics**

Statics consists of the study of bodies in equilibrium, while dynamics is concerned with their motion. In order to design and control a system, it is important to understand the system's dynamic behaviour. In this work, dynamics simulation is carried out to study the system's response to certain inputs and/or disturbances. Since a system will not only respond to inputs (disturbances are a kind of input), but also to its initial condition, it is necessary to separate the effects of the initial condition from the motion response. Thus, we are interested in obtaining a solution to the statics equilibrium, which can be used as a stable initial condition for the dynamics simulation.

### **3.1 Model Overview and Problem Description**

The multi-tethered aerostat system, as shown in Figure 1.2, consists of:

- 1) The payload platform;
- 2) A spherical or streamlined aerostat; and
- 3) Cables, including a leash tying the aerostat to the payload platform, and a group of tethers (three or six in this work) attaching the payload platform to the ground.

The focal length of the reflector is fixed at  $R = 500$  metres in this study. Thus, the zenith angle and the azimuth angle define the desired payload platform position (Figure 1.3). Determination of the system's equilibrium for a given position of the payload platform (and given orientations when applicable) requires us to obtain the equilibrium configuration of all the bodies in the system. Before explaining the solution procedure for this problem, the system model is first explained.

### 3.1.1 The Aerostat Model

The aerostat is modelled as a body with six degrees of freedom (DOFs), three translational DOFs and three rotational DOFs. The translational DOFs are represented by the position of the mass center of the aerostat in the inertial frame; the rotational DOFs are represented by the  $Z$ - $Y$ - $X$  Euler angle set. The aerostat is subject to gravity, aerodynamic forces and buoyancy provided by the lighter-than-air gas, which is helium in this study.

In Chapters 3 and 4, the investigation focuses on the use of a spherical aerostat. This aerostat has the properties listed in Table 3.1 [24]. The properties of the streamlined aerostat will be discussed in Chapter 5.

Table 3.1 Spherical aerostat properties

Diameter	19.7 m
Mass	610 kg
Buoyancy	40,870 N

### 3.1.2 The Payload Platform Model

The payload platform is subject to gravity, aerodynamic drag and tensions in the tethers attached to it. It is treated differently in different simulation cases. In the triple-tethered system or the six-tethered redundantly actuated system which will be discussed later, it is modelled as a point mass with three translational DOFs, specified by the  $X, Y, Z$  position of the platform in the inertial frame. In the six-tethered determinate system, it is modelled as a 6-DOF body with both translational and rotational DOFs. The three rotational DOFs are defined by the three  $Z$ - $Y$ - $Z$  Euler angle set:  $\alpha, \beta, \gamma$ . The aerodynamic forces are calculated by modelling the payload platform as a sphere of 6 m diameter, with a mass of 500 kg and a drag coefficient of 0.15.

### 3.1.3 The Cable Model

When modelling the cables, it is assumed that the effects of bending and torsion are small and need not be included in the model. The cable model consists of straight-line but elastic segments joined by frictionless revolute joints, as shown in Figure 3.1. The unstretched lengths of the main tethers are to be solved for in the statics while the leash has a prescribed unstretched length of 100 m. Each main cable is modelled to have 10 segments and the leash is modelled to have 2 segments. These segments are treated as the combination of a spring and a damper, with the mass lumped at the center. Forces applied to each segment, including tension, weight, aerodynamic drag are considered in the equilibrium calculation.



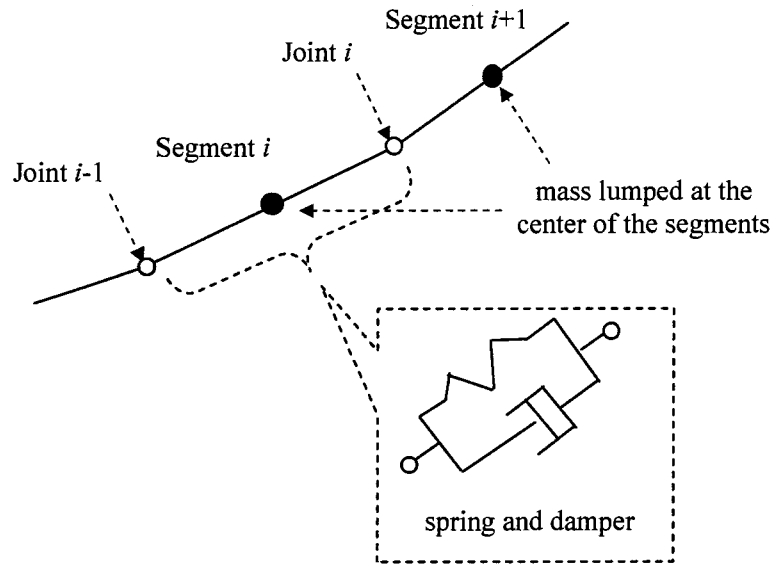


Figure 3.1 Cable segment model (statics)

The cable properties in this study for the triple-tethered system are listed as in Table 3.2 [24]. The cable properties for the six-tethered system will be discussed later in Chapter 4.

Table 3.2 Cable properties

Diameter	0.0185 m
Young's modulus	$16.67 \times 10^9$ N/m <sup>2</sup>
Leash length	100 m
Density	840 kg/m <sup>3</sup>
Normal drag coefficient	1.2

In the statics problem, every mass of the cable, the payload platform and the aerostat must be in equilibrium. This equilibrium requires that the vector resultant of all forces

acting on each body is zero ( $\Sigma \mathbf{F} = \mathbf{0}$ ). In addition, for any bodies with rotational DOFs, such as the payload platform in a six-tethered system and the aerostat, the vector resultant of all moments must also be zero ( $\Sigma \mathbf{M} = \mathbf{0}$ ). The force equilibrium equations, and the moment equilibrium equations when applicable, constitute the statics problem for the system.

Fitzsimmons, et al. [23] presented a steady-state analysis of the LAR system using this model. Part of the code developed in that work has been adopted and modified for the purposes of this work. In the following section, Fitzsimmons' statics solution is discussed, as it relates to the triple-tethered aerostat system with a spherical aerostat. Later, in Chapters 4 and 5, the extension of this solution to other cases will be discussed.

### 3.2 Fitzsimmons' Statics Solution

The first attempt to solve the statics problem for this system was based on simply writing the force/moment balance equations for all masses in the system, and then using a nonlinear equation solver to find the mass positions. This proved to yield an ill-conditioned Jacobian matrix and could only be solved for very elastic tethers. After some fruitless effort in this direction, this approach was abandoned and instead Fitzsimmons' statics solution was used.

Fitzsimmons [23] solved the statics problem for a triple-tethered system configuration by finding the tether profiles under a prescribed steady wind condition. In the configuration considered, all tethers, including the leash, meet at the confluence point (CP) --- the center of mass of the payload platform. The information to be determined includes the unstretched tether lengths, positions of all objects in the system. To do this

requires that we first specify the necessary system information, which are the desired CP position, tether winch positions, tether properties, numbers of nodes in each tether, aerostat characteristics etc.

Fitzsimmons' approach obtains the tether profiles one by one. For each tether, a no-wind analysis is used to provide an initial guess of unstretched lengths and winch forces. The winch force is then adjusted to achieve position coincidence of the tether top node and the CP. Once this is accomplished for all tethers, the resultant force at the CP is checked. If it is not zero, the unbalanced resultant force is used to adjust the unstretched lengths of tethers, and the tether profile calculations are repeated. This process continues until the algorithm has converged (i.e., the resultant force at the CP is close enough to zero).

Figure 3.2 illustrates this procedure. The shadowed blocks in the diagram are the main parts that will later require modifications in order to adapt Fitzsimmons' approach to the six-tethered aerostat system. The steps (blocks in Figure 3.2) are explained in more detail as follows:

### **Block A**

Initialize parameters. These parameters include: the number of tethers; tether properties; the length of the leash; locations of the base of each tether from the origin (center of reflector); payload properties; the specified CP position defined by a zenith angle, an azimuth angle, and a focal length  $R$ ; the steady wind condition; and the aerostat characteristics.

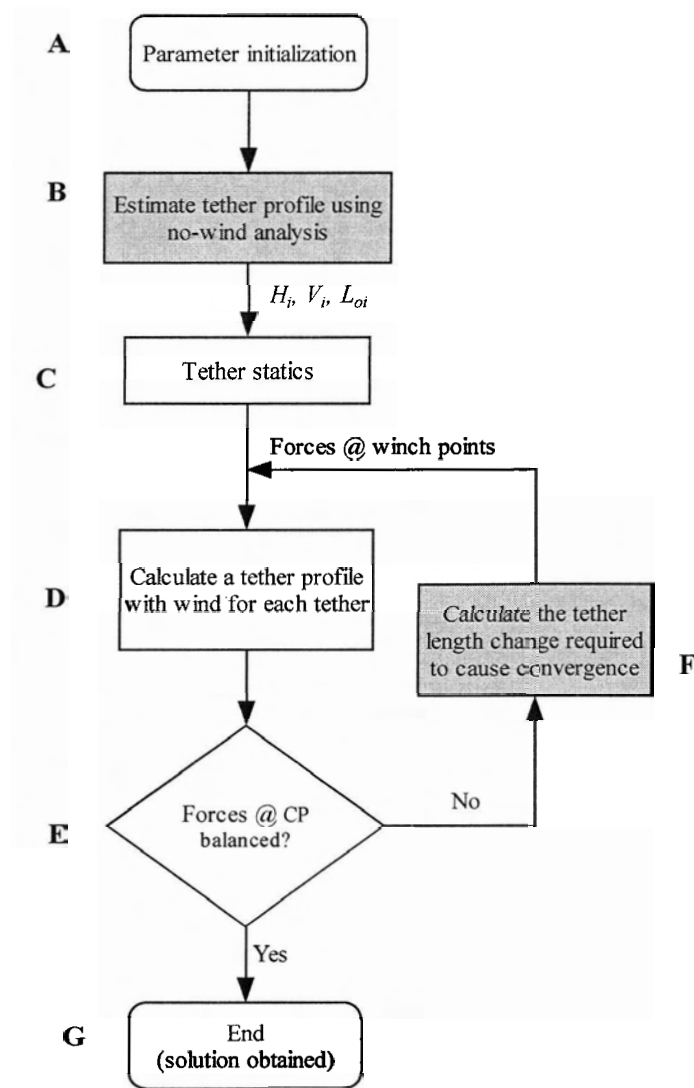


Figure 3.2 Flowchart of statics solution by Fitzsimmons

### **Block B**

Using a no-wind analysis [23], find an approximate solution to the tether unstretched lengths and forces at the upper ends. In the absence of environmental loads, the tension of a single suspended cable at both ends can be obtained if the position of both ends and the

unstretched length of the cable are prescribed [26].

Figure 3.3 shows the  $i$ -th elastic cable suspended in a vertical plane, which is the configuration we are interested in. Assuming that the unstretched length of the cable is  $L_{0i}$ , the cross-sectional area of the unstretched cable is  $A_0$ , the Young's modulus of the cable is  $E$ , and the cable end positions are  $(0, 0)$  and  $(l_i, h_i)$  in a reference frame as shown in Figure 3.3, the solutions for the horizontal and the vertical components of the tension at the top end,  $H_i$  and  $V_i$  respectively, can be obtained from the following two nonlinear algebraic equations [26]:

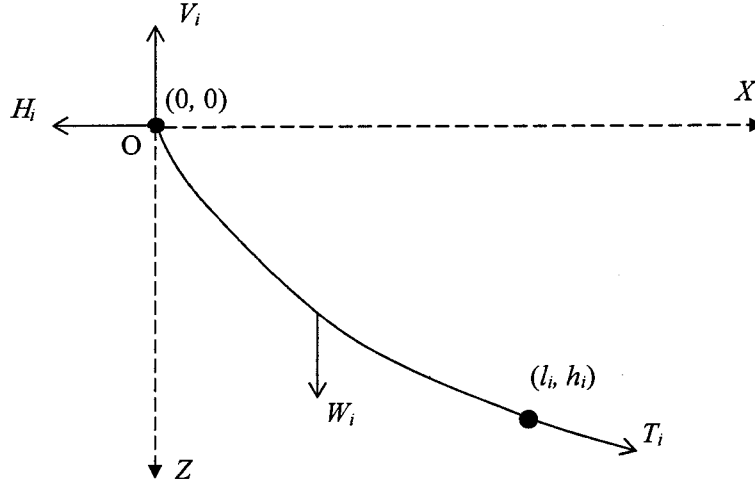


Figure 3.3 The strained cable profile

$$\begin{aligned}
 l_i &= \frac{H_i L_{0i}}{EA_0} + \frac{H_i L_{0i}}{W_i} \left[ \sinh^{-1} \frac{V_i}{H_i} - \sinh^{-1} \left( \frac{V_i - W_i}{H_i} \right) \right], \quad i = 1, 2, 3 \\
 h_i &= \frac{W_i L_{0i}}{EA_0} \left( \frac{V_i}{W_i} - \frac{1}{2} \right) + \frac{H_i L_{0i}}{W_i} \left\{ \left[ 1 + \left( \frac{V_i}{H_i} \right)^2 \right]^{1/2} - \left[ 1 + \left( \frac{V_i - W_i}{H_i} \right)^2 \right]^{1/2} \right\}
 \end{aligned} \tag{3.1}$$

where  $W_i$  is the weight of the tether which is a function of  $L_{0i}$ .

The equilibrium requires that the resultant of all forces acting at the CP is zero. This leads to three equilibrium force equations at the CP

$$\Sigma F_x = 0, \quad \Sigma F_y = 0, \quad \Sigma F_z = 0$$

We can expand these as components in the inertial frame  $O_I X_I Y_I Z_I$  as follows:

$$\begin{aligned} \sum_{i=1}^3 H_{xi} &= 0 \\ \sum_{i=1}^3 H_{yi} &= 0 \\ \sum_{i=1}^3 V_i + W_p + T_{lz} &= 0 \end{aligned} \tag{3.2}$$

where  $H_{xi}$ ,  $H_{yi}$ , are the components of  $H_i$  along  $X_I$ - and  $Y_I$ -directions;  $W_p$  is the payload weight; and  $T_{lz}$  is the  $Z_I$ -component of the leash tension which is purely vertical in the no-wind case. It should be noted that  $T_{lz}$  can be easily obtained as the weight and lift of the aerostat and weight of the leash are known. Assembling the three force equilibrium Equations (3.2) and the tether static equilibrium Equations (3.1) together --- nine equations in total, we can solve for the nine unknowns,  $H_i$ ,  $V_i$  and  $L_{0i}$  ( $i = 1, 2, 3$ ) of the tethers, using a Newton-Raphson nonlinear equation solver [27].

The Newton-Raphson solver must be given an initial guess for the unknowns before it begins iterating. The initial guess for the variables  $H_i$  and  $V_i$  ( $i = 1, 2, 3$ ) was found by first solving for an approximation to the tether tensions  $T_i$  ( $i = 1, 2, 3$ ) using

$$\begin{bmatrix} \frac{d_{x1}}{d_1} & \frac{d_{x2}}{d_2} & \frac{d_{x3}}{d_3} \\ \frac{d_{y1}}{d_1} & \frac{d_{y2}}{d_2} & \frac{d_{y3}}{d_3} \\ \frac{d_{z1}}{d_1} & \frac{d_{z2}}{d_2} & \frac{d_{z3}}{d_3} \end{bmatrix} \begin{bmatrix} T_1 \\ T_2 \\ T_3 \end{bmatrix} = \begin{bmatrix} 0 \\ 0 \\ -T_{lz} - W_p \end{bmatrix} \tag{3.3}$$

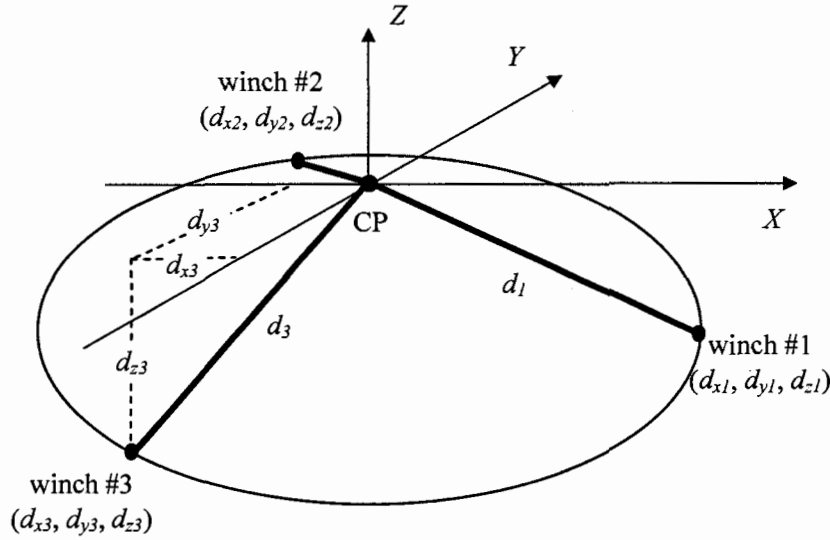


Figure 3.4 Tethers in a 3-D space

where  $(d_{xi}, d_{yi}, d_{zi})$  is the ground end position of tether  $i$ ,  $i = 1, 2, 3$ , in the inertial frame with its origin at the center of payload (Figure 3.4) and  $d_i = \sqrt{d_{xi}^2 + d_{yi}^2 + d_{zi}^2}$ . Then, using those values of  $T_i$ , the horizontal and vertical components were found from

$$\begin{bmatrix} H_{x1} & H_{x2} & H_{x3} \\ H_{y1} & H_{y2} & H_{y3} \\ V_1 & V_2 & V_3 \end{bmatrix} = \begin{bmatrix} \frac{d_{x1}}{d_1} & \frac{d_{x2}}{d_2} & \frac{d_{x3}}{d_3} \\ \frac{d_{y1}}{d_1} & \frac{d_{y2}}{d_2} & \frac{d_{y3}}{d_3} \\ \frac{d_{z1}}{d_1} & \frac{d_{z2}}{d_2} & \frac{d_{z3}}{d_3} \end{bmatrix} \begin{bmatrix} T_1 \\ T_2 \\ T_3 \end{bmatrix} \quad (3.4)$$

The initial guess for the unstretched lengths  $L_{0i}$  ( $i = 1, 2, 3$ ) are assumed to be

$$L_{0i} = 0.99d_i \quad i = 1, 2, 3 \quad (3.5)$$

### **Block C**

We can now find the winch force,  $T_i$ , for each tether. This is done by considering the

equilibrium of external forces acting on each tether (see Figure 3.3):

$$\mathbf{T}_i + \mathbf{H}_i + \mathbf{V}_i + \mathbf{W}_i = \mathbf{0} \quad (3.6)$$

where  $\mathbf{T}_i$ ,  $\mathbf{H}_i$ ,  $\mathbf{V}_i$  and  $\mathbf{W}_i$  are the vector form of the scalar forces  $T_i$ ,  $H_i$ ,  $V_i$  and  $W_i$  respectively. The forces  $H_i$  and  $V_i$ , acting at the top node are known from Block B, while the weight of the tether  $W_i$  is known from the tether properties and unstretched length  $L_0$  calculated from Block B.

#### **Block D**

Using the unstretched length from the no-wind analysis of Block B and the winch force from Block C, we can now calculate the profile of each tether in the presence of the prescribed wind. Each tether profile, including the profile of the leash is solved independently, segment by segment starting from the far-from-CP end and ending at the CP end (all tethers meet at the CP). The tether profile calculation is illustrated in the flowchart shown in Figure 3.6.

The steps shown in Figure 3.6 are explained as follows:

- D1. For each segment, we use the known tension at the segment end far from the CP to calculate the tension at the segment end close to the CP, as well as the orientation of the segment.

Figure 3.5 shows the forces acting on the first segment of a tether attached to the ground. Since the unstretched length of the tether is fixed, the unstretched length of each segment is known; the weight  $\mathbf{W}_1$  is known;  $\mathbf{D}_1$ , the aerodynamic drag of the first segment, is a function of the tether position and orientation, when the wind is known. Angles  $\beta_1$ ,  $\Gamma_1$  as shown in Figure 3.5 define the orientation of



the tether segment (a third angle is not necessary as we ignore the torsion in the segment). Thus, when  $\mathbf{T}_{winch}$  (with components  $T_{x0}$ ,  $T_{y0}$ ,  $T_{z0}$ ) is known,  $\mathbf{T}_1$  (with components  $T_{x1}$ ,  $T_{y1}$ ,  $T_{z1}$ ), and  $\beta_l$ ,  $\Gamma_l$  can be derived from the equilibrium condition. Summing up all the forces applied to the segment and moments about the center of mass (CM in Figure 3.5) of the segment in the inertial frame, we have

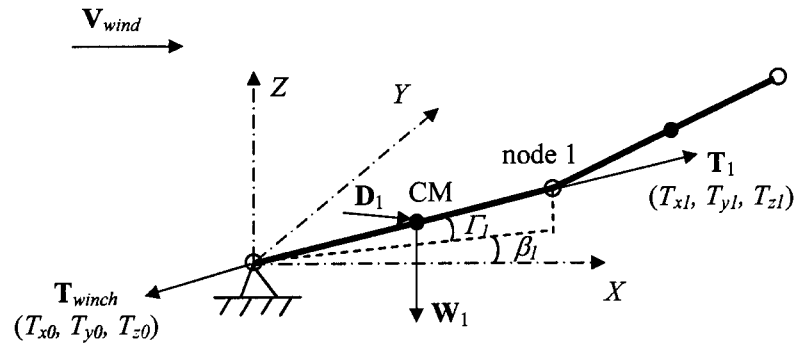


Figure 3.5 Tether segment analysis

$$\begin{aligned}
 T_{x0} + T_{x1} + D_{x1} &= 0 \\
 T_{y0} + T_{y1} + D_{y1} &= 0 \\
 T_{z0} + T_{z1} + W_1 &= 0 \\
 T_{z0} \cos \Gamma_l \cos \beta_l - T_{x0} \sin \Gamma_l - T_{z1} \cos \Gamma_l \cos \beta_l + T_{x1} \sin \Gamma_l &= 0 \\
 T_{x0} \cos \Gamma_l \sin \beta_l - T_{y0} \cos \Gamma_l \cos \beta_l - T_{x1} \cos \Gamma_l \sin \beta_l + T_{y1} \cos \Gamma_l \cos \beta_l &= 0
 \end{aligned} \tag{3.7}$$

where the distance from the winch to the center of mass and that from node 1 to the center of mass are equal and cancel out in the moment equations. The drag forces  $D_{x1}$  and  $D_{y1}$  are nonlinear functions of  $\beta_l$  and  $\Gamma_l$ . The 5 unknowns:  $T_{x1}$ ,  $T_{y1}$ ,  $T_{z1}$ ,  $\beta_l$ ,  $\Gamma_l$  can then be solved from the 5 nonlinear equations in Equations (3.7) using the Newton-Raphson nonlinear equation solver [27].

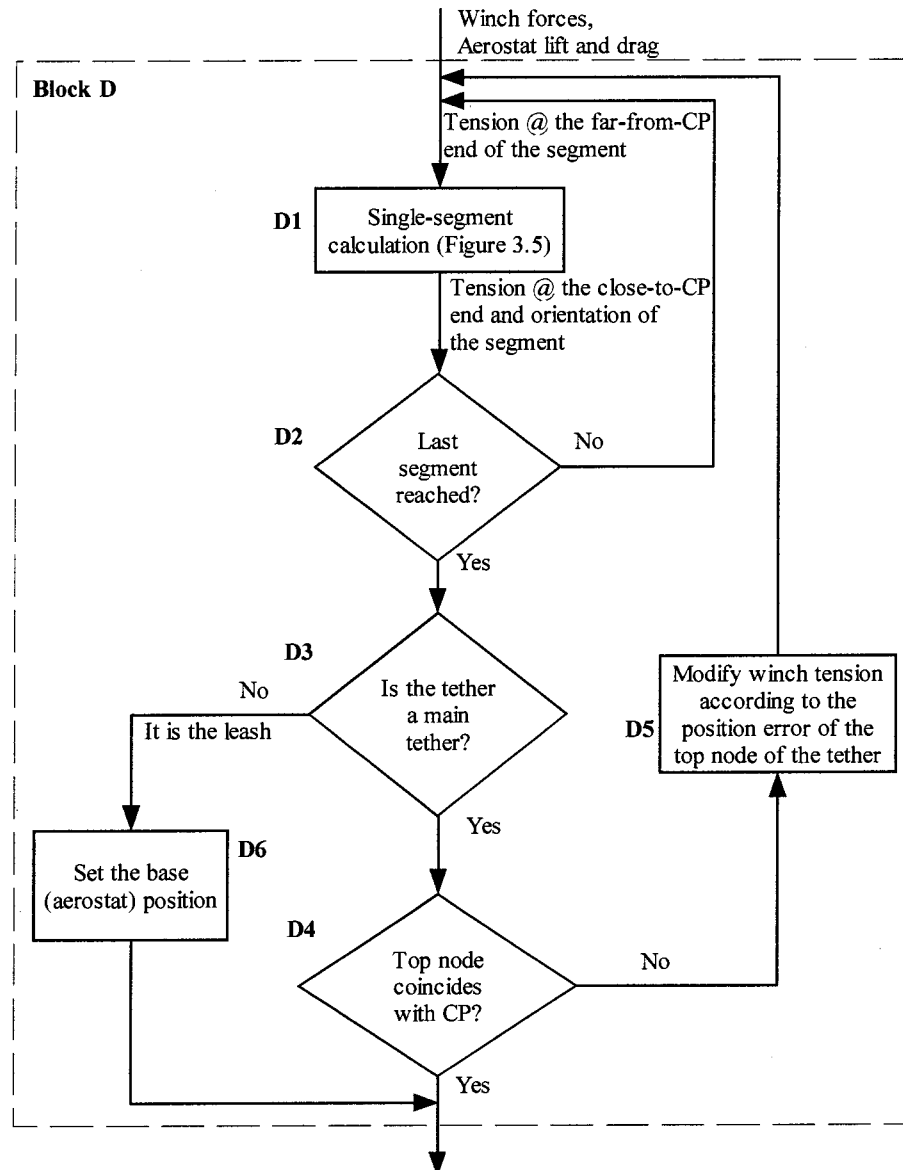


Figure 3.6 Tether profile calculation (Block D in Figure 3.2)

- D2. Starting from the end which is the farthest from the CP, the single-segment calculation of Block D1 is repeated until the segment connected to the CP is reached. With tensions at all ends and the orientations of all segments obtained, the

tether profile is known, and the position of the end attached to the CP, can be calculated from the unstretched length solved from the no-wind analysis and the Young's modulus of the tether.

- D3. Check whether the tether is a main tether or the leash --- the leash is a special case as its unstretched length is known a priori.
- D4. If the tether is a main tether, check whether the position of its top end, denoted as  $(x_i, y_i, z_i)$  for the  $i$ -th tether, coincides with that of the CP  $(x_{CP}, y_{CP}, z_{CP})$  within a certain tolerance:

$$\sqrt{(x_i - x_{CP})^2 + (y_i - y_{CP})^2 + (z_i - z_{CP})^2} \leq \varepsilon_p \quad (3.8)$$

where  $\varepsilon_p$  is set to 0.001 m, which is about one millionth of the distance from the winch to the CP.

Because the no-wind solution of the tension at the base end was used, the position of the top end of the tether will probably not coincide with the position of the CP at the first iteration.

- D5. Adjust the winch tension according to the position error. The adjustment made at the winch relies on an approximation of the relation between the tether tension and the change of tether length after being stretched. This approximation is based on the assumption that the tether is straight.

Under this assumption, tether  $i$  with an unstretched length of  $L_{0i}$  and a straight-line distance between the two ends of  $d_i$  will have a tension of

$$T_i = EA_0 \frac{d_i - L_{0i}}{L_{0i}} = EA_0 \left( \frac{d_i}{L_{0i}} - 1 \right) \quad (3.9)$$

Figure 3.7 illustrates the rationale of the algorithm. The top end of the tether in this step is shown as point P. The tension in the tether can be expressed in vector form as

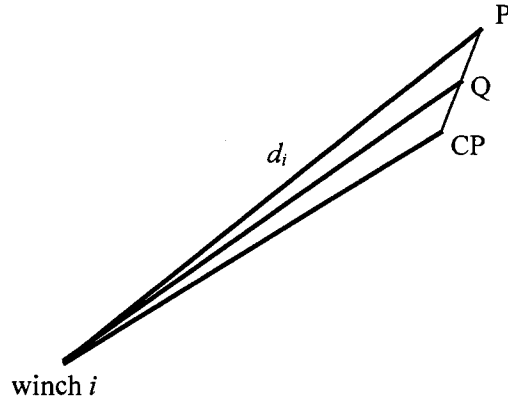


Figure 3.7 Approximation used in tether analysis

$$\mathbf{T}_i = -T_i \frac{\mathbf{P}_i}{\|\mathbf{P}_i\|} = -EA_0 \left( \frac{\|\mathbf{P}_i\|}{L_{0i}} - 1 \right) \frac{\mathbf{P}_i}{\|\mathbf{P}_i\|} \quad (3.10)$$

where  $\mathbf{P}_i$  is the position vector from winch location  $i$  to P. When point P does not coincide with its desired position --- the CP, an adjustment is made to the winch tension. This adjustment is intended to move the top end to point Q, which is between point P and the CP. If the position vector from the winch  $i$  to the CP is  $\mathbf{P}_{0i}$ , then the position vector from the winch location  $i$  to Q, can be expressed as

$$\mathbf{Q}_i = \mathbf{P}_i + \alpha (\mathbf{P}_{0i} - \mathbf{P}_i) = \alpha \mathbf{P}_{0i} + (1 - \alpha) \mathbf{P}_i \quad (3.11)$$

where  $\alpha$  is a number between 0 and 1. Therefore, we know the resulting change in the tension when we move the top node from P to Q:

$$\Delta \mathbf{T}_i = EA_0 \left\{ \left( \frac{\|\mathbf{P}_i\|}{L_{0i}} - 1 \right) \frac{\mathbf{P}_i}{\|\mathbf{P}_i\|} - \left( \frac{\|\mathbf{Q}_i\|}{L_{0i}} - 1 \right) \frac{\mathbf{Q}_i}{\|\mathbf{Q}_i\|} \right\} \quad (3.12)$$

In Fitzsimmons' statics solution,  $\alpha$  in Equation (3.8) is set to 0.75 initially. If the convergence proceeds smoothly, this will allow point P to reach the CP after a number of iterations. Some rules are used to increase or decrease  $\alpha$  during the iterations if the convergence is not smooth. These rules improve convergence and robustness of the algorithm.

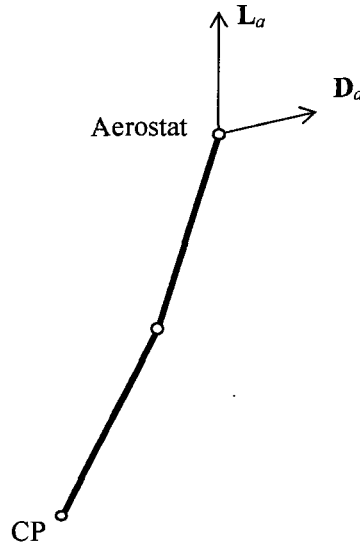


Figure 3.8 Leash analysis

- D6. For the leash, the solution is not iterative. Figure 3.8 illustrates the leash analysis. The leash is modelled as two segments. The aerostat's lift,  $\mathbf{L}_a$ , and drag,  $\mathbf{D}_a$ , can be obtained from the prescribed wind condition and the aerostat properties. Similar to the tethers attached to the ground, we start the calculation at the segment farthest from the CP. Once the tether segment calculation is completed, the tensions at the

CP end and the leash profile are obtained. The aerostat position in the inertial frame can be obtained from the CP position and the relative position of the aerostat end from the CP.

### **Block E**

At the output of Block D, the top end of all three tethers and the lower end of the leash now all meet at the CP. The tension that each cable exerts on the CP is also known. In equilibrium, the resultant force at the CP should be zero within a certain tolerance:

$$\sqrt{(\Sigma F_x)^2 + (\Sigma F_y)^2 + (\Sigma F_z)^2} \leq \varepsilon_f \quad (3.13)$$

where  $\varepsilon_f$  is set to 1.5 N, and relaxed to 5.0 N when the number of iterations has exceeded 50.

Since each tether has been analyzed independently, using a value of the unstretched length determined from the no-wind analysis, the resultant force will, in general, not be zero at the first iteration.

### **Block F**

The resultant force at the CP is used to generate a length adjustment for each tether. The algorithm used relies on an approximation of the relation between the change in tension due to a change in the unstretched length of a tether, based on the assumption that the tether is straight --- without considering the effects of weight and wind.

If a tether in Figure 3.4 has an unstretched length of  $L_{0i}$ , and a straight-line distance between its two ends of  $d_i$ , then a change in the unstretched length of  $\Delta L_{0i}$ , will lead to a change in the tension in the tether  $\Delta T_i$  of

$$\Delta T_i = EA_0 \left( \frac{d_i - (L_{0i} + \Delta L_{0i})}{L_{0i} + \Delta L_{0i}} - \frac{d_i - L_{0i}}{L_{0i}} \right) = -EA_0 \frac{d_i \Delta L_{0i}}{L_{0i} (L_{0i} + \Delta L_{0i})} \quad (3.14)$$

In this analysis, a reference frame with its origin at the CP (Figure 3.4) is employed. For each tether, the winch point is located at  $(d_{xi}, d_{yi}, d_{zi})$ . When the unstretched length has a change of  $\Delta L_{0i}$ , the force changes in the  $X$ -,  $Y$ - and  $Z$ -directions as in Figure 3.4,  $\Delta T_{xi}$ ,  $\Delta T_{yi}$ ,  $\Delta T_{zi}$ , are

$$\begin{aligned} \Delta T_{xi} &= -EA_0 \frac{d_{xi} \Delta L_{0i}}{L_{0i} (L_{0i} + \Delta L_{0i})} \\ \Delta T_{yi} &= -EA_0 \frac{d_{yi} \Delta L_{0i}}{L_{0i} (L_{0i} + \Delta L_{0i})} \\ \Delta T_{zi} &= -EA_0 \frac{d_{zi} \Delta L_{0i}}{L_{0i} (L_{0i} + \Delta L_{0i})} \end{aligned} \quad (3.15)$$

Therefore, when the resultant force at the CP is not zero, we assume that we can adjust the unstretched length of tether  $i$  by an amount  $\Delta L_{0i}$ , so that the resultant force change corresponding to the length changes will cancel out the unbalanced force at the CP. The desired unstretched length changes are found from the following equations:

$$\begin{aligned} \sum_{i=1}^3 H_{xi} + D_{px} + T_{lx} - EA_0 \sum_{i=1}^3 \frac{d_{xi} \Delta L_{0i}}{L_{0i} (L_{0i} + \Delta L_{0i})} &= 0 \\ \sum_{i=1}^3 H_{yi} + D_{py} + T_{ly} - EA_0 \sum_{i=1}^3 \frac{d_{yi} \Delta L_{0i}}{L_{0i} (L_{0i} + \Delta L_{0i})} &= 0 \\ \sum_{i=1}^3 V_i + W_p + T_{lz} - EA_0 \sum_{i=1}^3 \frac{d_{zi} \Delta L_{0i}}{L_{0i} (L_{0i} + \Delta L_{0i})} &= 0 \end{aligned} \quad (3.16)$$

where  $H_{xi}$ ,  $H_{yi}$ ,  $V_i$  are the  $X_I$ -,  $Y_I$ - and  $Z_I$ -components of the tension of tether  $i$ ,  $D_{px}$  and  $D_{py}$  are the  $X_I$ - and  $Y_I$ -components of the aerodynamic drag on the payload, and  $T_{lx}$ ,  $T_{ly}$  and  $T_{lz}$  are the  $X_I$ -,  $Y_I$ - and  $Z_I$ -components of the leash tension. This is a system of 3 nonlinear equations in 3 unknowns  $\Delta L_{01}$ ,  $\Delta L_{02}$  and  $\Delta L_{03}$ .

This problem is solved by the same Newton-Raphson algorithm as was used in Block B [27]. The program returns to Block D with the new unstretched lengths of the tethers  $L_{oi} + \Delta L_{oi}$ .

### **Block G**

Once the resultant force at the CP satisfies Inequality (3.13), we have a solution for the equilibrium. The obtained tether profile information can then be used to provide an initial condition for the dynamics simulation.

## **3.3 Implementation and Modifications of Fitzsimmons' Solution**

Fitzsimmons' statics solution was incorporated into our simulation for the case of a triple-tethered system. In doing so, Block A (parameter initialization) in Figure 3.2 was modified to accept parameters already defined in our main program and the result of Block G was modified to provide initial condition for the dynamics simulation which will be discussed in Chapter 4.

Some other modifications to Fitzsimmons' model were needed to incorporate his solution into our work, and these are now discussed.

### **Wind Model**

The wind model in Fitzsimmons' work was modified to match the one used in the dynamics model [24]. In Fitzsimmons' wind model, illustrated on the left of Figure 3.9, the wind speed is constant with height. By contrast, the wind model in the dynamics, illustrated on the right of Figure 3.9, uses a power law profile [24] defined by



$$U = U_g \left( \frac{h}{z_g} \right)^{0.19} \quad (3.17)$$

The constant profile used in Fitzsimmons' work was therefore replaced by the power-law profile which is a more reasonable representation of the wind conditions over rural terrain. Unless otherwise mentioned, this power-law wind profile is used throughout this study and sometimes only the full wind speed  $U_g$  is mentioned.

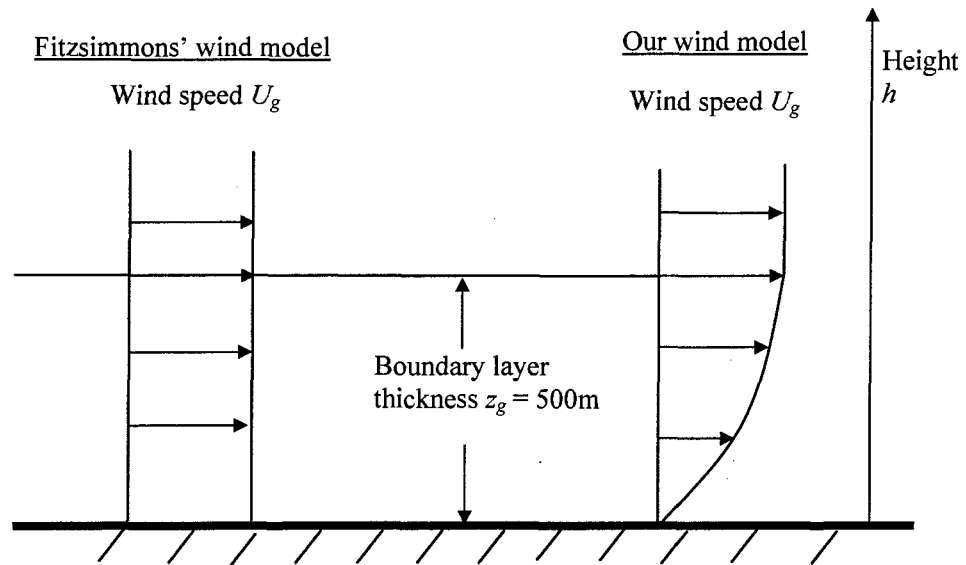


Figure 3.9 Wind models

### Jacobian Matrix Calculations

In Blocks B, D (D1 in Figure 3.6) and F of the solution procedure (Figure 3.2), a Newton-Raphson method [27] is used to solve a system of nonlinear algebraic equations. This requires a calculation of the Jacobian matrix of the system of equations.

In Fitzsimmons' implementation, this Jacobian matrix was approximated using a finite difference scheme. To improve the robustness and speed of the solution, the finite difference approximations of the Jacobian matrices were replaced by exact analytical calculations in our implementation of the Newton-Raphson algorithm.

Further changes to Fitzsimmons' statics solution will be discussed in Chapter 4 and 5 as they are related to configurations other than the three-tether spherical aerostat configuration --- specifically, the six-tether spherical aerostat or the three-tether streamlined aerostat configurations.

### **3.4 Verification of the Statics Model**

Model verification is of great importance for simulation studies, as conclusions based on an inaccurate model will be flawed. Fitzsimmons verified his work by comparing results from different methods of analysis [23]. When incorporating his work into ours, we had to ensure that we did not introduce errors. Our verification was done in a few ways.

The first verification was done to compare the statics results after incorporation into our software to those from Fitzsimmons' original version for the same set of conditions. This verification work was done without introducing the modifications discussed in Section 3.3. The comparison between the statics results, showed the two sets of results to be identical to 8 significant figures. This gives us confidence that errors were not introduced when incorporating Fitzsimmons' work into ours.

Our next validation consisted of running the open-loop dynamic simulations [24] (to be discussed in Chapter 4) with the initial conditions generated by the statics analysis,

including the modifications of Section 3.3. This allowed us to see whether the statics analysis generates a true equilibrium condition for the specified set of parameters. If it does, the dynamics simulations should show the system staying at that equilibrium, within acceptable errors; otherwise, the system will deviate from the statics solution, presumably toward the true equilibrium. The conditions of configurations tested are listed in Table 3.3. The wind condition used in all cases is identical. The power-law wind profile defined by Equation (3.17) is used. The mean wind speed is 10 m/s, and the wind angle of  $180^\circ$  is defined as the angle from the positive  $X$ -axis to the wind vector in the horizontal  $XY$ -plane. The initial conditions for the dynamics simulation are the results obtained from the statics solver.

Table 3.3 Conditions of simulation cases

Case No.	Zenith angle ( $^\circ$ )	Azimuth angle ( $^\circ$ )	Wind condition
1	0	0	Power-law wind profile with a mean wind speed of 10 m/s and a wind angle of $180^\circ$
2	60	0	
3	60	60	

Figure 3.10 shows the resulting errors, plotted as errors of the CP position in and out of the focal plane --- the plane tangent to the hemisphere (shown as the  $\Delta_{zd}$ - $\Delta_{az}$  plane in Figure 1.3). From the results, we can see that:

- 1) In the focal plane, the worst case is Case 2 with about 1.5 mm error; the error out of the focal plane is worst for Case 3 at about 3 mm. It should be noted that the scale of the multi-tethered aerostat system is on the order of 1 km, and

the expected positioning accuracy is to be about 1 m, therefore these errors are very small.

- 2) The position errors are slightly higher for the asymmetrical Cases 2 and 3 than for the symmetric Case 1, and the error oscillations are worse for Cases 2 and 3 as well. This is likely due to the higher stiffness of the system in Case 1.

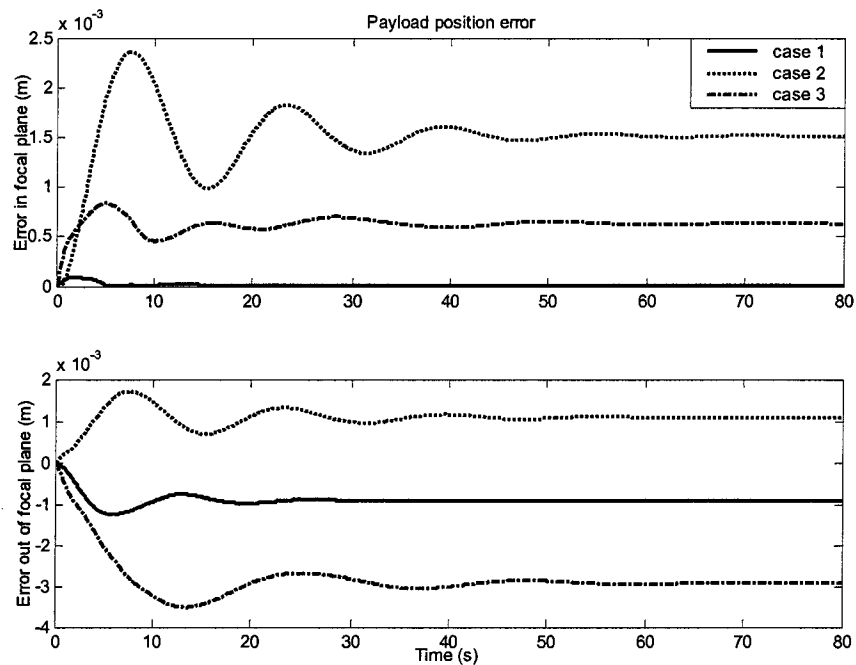


Figure 3.10 Errors of the CP when using statics solution as the initial states

The dynamics and statics models demonstrate a very good match. The slight differences can be explained by the remaining model differences between the two models. For example, in the dynamics model, the mass of each segment is split into two halves and lumped at the segment ends. By contrast, the statics model lumps the segment's mass

at the midpoint of the segment. The close match between the results of the dynamics and statics models, each of which was developed by different people, gives us confidence that both models are good representations of the system.

## **Chapter 4 Six-Tethered System**

The computer model of a triple-tethered system developed by Nahon [24] showed that the payload platform position could be controlled accurately by three tethers in the presence of disturbances. However, there are some advantages to using more than three tethers. For example, six tethers might allow us to also control the orientation of the airborne platform. Alternatively, six tethers could be used for redundant control of the position of the platform. These are the issues studied in this chapter.

### **4.1 Dynamics of the Triple-Tethered System**

In Section 3.1, a statics model of the triple-tethered aerostat system with a spherical aerostat was described. In Nahon's work [24], a similar physical model of the triple-tethered spherical aerostat system was used to obtain the system's dynamic equations of motion and solve for the time histories of the system's motion. The only difference between the two models is in the way in which the mass of each cable segment is lumped. Figure 4.1 shows how this is done in the dynamics simulation of [24]. The key difference from the approach shown in Figure 3.1 is that the mass of each element is split in half and

each half is lumped at the end points of the element. Motion equations are formulated for the nodes where the mass is lumped.

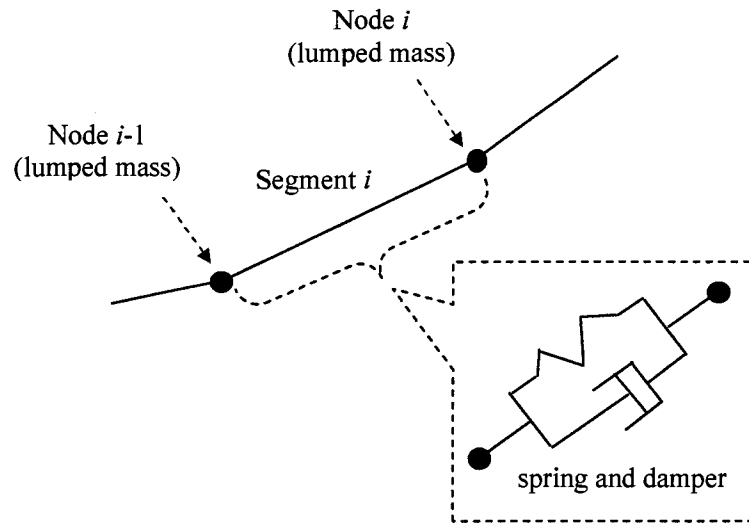


Figure 4.1 Cable segment model (dynamics)

A wind model is also incorporated in [24] to determine the effect of the turbulent wind on the tethered aerostat system. This wind model consists of a mean wind profile (as shown in right half of Figure 3.9) with turbulent gusts superimposed.

All bodies in the system model, including the cable nodes, the payload platform, and the aerostat, are modelled as bodies with only translational DOFs. The motion equations governing the motion of the system are set up by applying Newton's second law of motion ( $\Sigma \mathbf{F} = m\mathbf{a}$ ) to each body to relate its acceleration vector and the vector resultant of all forces applied to it [24].

In Nahon's work [24], the spherical aerostat is modelled as a point mass with three translational DOFs (Figure 4.2). Forces applied to the aerostat include weight  $\mathbf{W}_a$ ,

buoyancy  $\mathbf{B}_a$ , aerodynamics drag  $\mathbf{D}_a$  and the leash tension  $\mathbf{T}_l$  and damping force  $\mathbf{P}_l$  which are the internal forces of the top most segment of the leash. Considering added mass, its motion equation can be expressed as:

$$\mathbf{B}_a + \mathbf{W}_a + \mathbf{D}_a + \mathbf{T}_l + \mathbf{P}_l = (m_a + m_{aa})\mathbf{a}_a \quad (4.1)$$

where  $m_a$  and  $m_{aa}$  are the mass and added mass of the aerostat.

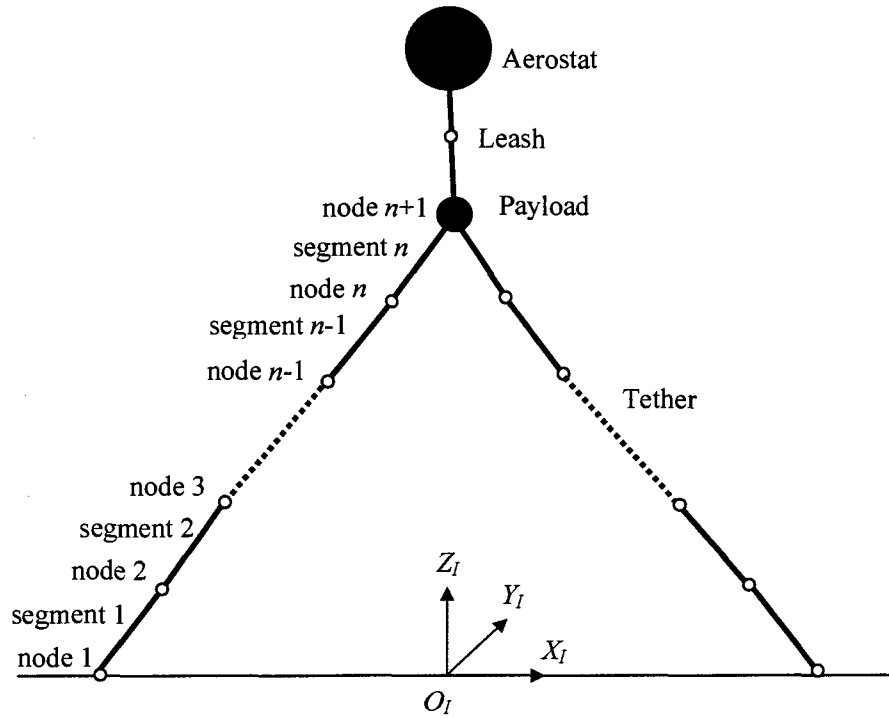


Figure 4.2 The tethered aerostat system model in 2-D [24]

The payload is also modelled as a point mass. Forces applied to it include its weight  $\mathbf{W}_p$ , aerodynamic drag  $\mathbf{D}_p$  and cable forces from the segments attached to it which



are the tensions  $\mathbf{T}_i$  and damping forces  $\mathbf{P}_i$ , where  $i = 1, \dots, 4$ , from all 4 cables, including the leash. The motion equation can be summed up as

$$\mathbf{W}_p + \mathbf{D}_p + \sum_{i=1}^4 (\mathbf{T}_i + \mathbf{P}_i) = (m_p + m_{ap}) \mathbf{a}_p \quad (4.2)$$

where  $m_p$  and  $m_{ap}$  are the mass and added mass of the payload.

Forces applied to each node of each tether include gravity, aerodynamic drag and internal tensions and damping forces. Damping force is created by the friction between braids of the cable [24]. It is assumed to be linear with the strain rate and calculated using [24]

$$\mathbf{P}_i = \mathbf{P}_i^z = C_v (\mathbf{v}_i^z - \mathbf{v}_{i-1}^z) \quad (4.3)$$

where  $C_v$  is the damping coefficient, 10,000 N·s/m for this application, and  $\mathbf{v}_i^z$  is the velocity of the  $i$ -th node in the tangential  $Z_{ti}$ -direction (Figure 2.1).

Summing up all the forces in the inertial frame, the motion equation for node  $i$  can be written as

$$\mathbf{T}_i + \mathbf{P}_i - (\mathbf{T}_{i-1} + \mathbf{P}_{i-1}) + \frac{1}{2} (\mathbf{W}_i + \mathbf{D}_i + \mathbf{W}_{i-1} + \mathbf{D}_{i-1}) = (m_i + m_{ai}) \mathbf{a}_i \quad (4.4)$$

where  $\mathbf{W}_i$ ,  $\mathbf{D}_i$ ,  $\mathbf{T}_i$  and  $\mathbf{P}_i$  are the weight, drag, tension and damping force in the  $i$ -th segment respectively,  $m_i$  and  $m_{ai}$  are the lumped mass and its added mass at node  $i$ , while  $\mathbf{a}_i$  is the acceleration of the node.

The above Equations (4.1), (4.2) and (4.4) contain 90 motion equations set up at 30 node points: each main tether is discretized into 10 segments and the leash is modelled using 2 segments. Thus each of the main tethers has 11 nodes and the leash has 3 nodes. The motion equations are set up at each node except the base node of the main tethers. The top nodes of the tethers and the bottom node of the leash are the same point as the

payload node. The top node of the leash is also the aerostat node. These 90 motion equations are second-order ordinary differential equations (ODEs). In order to use a conventional numerical integrator, each of the motion equations is rewritten as two first order differential equations, thus resulting in 180 first-order ODEs.

Moreover, PID controllers are implemented to control the winches, which are assumed to be located at the base of tethers. The winches adjust the unstretched length of each tether and thus control the position the payload platform. In particular, the winch controllers operate on the position errors of the CP [24]. A 2-D illustration of the control scheme is shown in Figure 4.3. Assuming the desired location of the CP is at  $\mathbf{p}_d (x_d, y_d, z_d)$ , its actual location is at  $\mathbf{p} (x, y, z)$ , and the  $i$ -th winch ( $i = 1, 2, 3$ ) is at  $\mathbf{w}^i (x_w^i, y_w^i, z_w^i)$ , we can define the desired and actual distances from each winch to the CP as [24]

$$L_d^i = \|\mathbf{p}_d - \mathbf{w}^i\|, \quad L^i = \|\mathbf{p} - \mathbf{w}^i\| \quad (4.5)$$

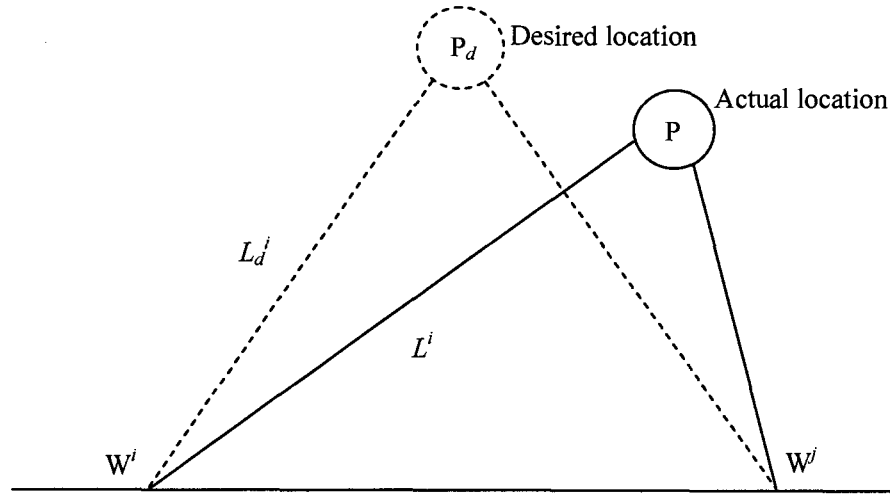


Figure 4.3 Controller 2-D illustration [24]

And the winch controller operates according to [24]

$$\dot{l}_{u1}^i = \dot{l}_{u10}^i - k_d(\dot{L}_d^i - \dot{L}^i) - k_p(L_d^i - L^i) - k_i \int (L_d^i - L^i) dt \quad (4.6)$$

where  $l_{u1}^i$  is the unstretched length of the first (lowermost) segment of tether  $i$ , while  $l_{u10}^i$  is its initial unstretched length, and  $k_d$ ,  $k_p$  and  $k_i$  are the PID controller gains. In order to integrate the error, 3 more first order differential equations are added to the system.

These 183 first order differential equations are solved using a fourth order Runge-Kutta integrator [27], which gives accurate solutions to a wide range of scientific problems.

Some main findings of the dynamics simulation are [24]:

- 1) The system is less well behaved at large zenith angles of the payload platform while it is not very sensitive to changes of the azimuth angle;
- 2) The system acts as a low-pass filter to turbulent gusts; and
- 3) The motion response of the payload platform may be controlled within centimeters of its desired position in the presence of turbulent gusts.

In this chapter, we are interested in extending the prior work on a triple-tethered system [24] to a six-tethered system.

## 4.2 Redundantly Actuated System

In the LAR multi-tethered system, the tethers, the payload platform and the ground form a closed-link mechanism. If we are only interested in controlling the position of the payload platform, the system is redundantly actuated if there are more than three adjustable tethers.

### 4.2.1 Actuation Redundancy

Redundancy is a feature of systems in a variety of fields, such as aerospace engineering, electrical engineering, and mechanical engineering. Redundancy can be primarily used to improve the reliability of a system. In many applications, redundancy also improves the system performance. In mechanical systems, there exist two kinds of redundancy: kinematic redundancy and actuation redundancy [28].

Kinematic redundancy implies a mechanism has more degrees of freedom (DOFs) than the number of DOFs needed to accomplish the task. Generally speaking, kinematic redundancy improves manipulability, is used to avoid obstacles, structural limitations or to optimize various performance criteria [28], [29].

Actuation redundancy implies that the system has more actuators than DOFs. It is found only in closed-loop mechanisms, and has an important effect on the determination of the forces and moments. The difference between the number of actuators and the number of DOFs is the degree of actuation redundancy.

In the LAR multi-tethered system, when six tethers are used to control the position of the payload platform, we say the system has three degrees of actuation redundancy. The actuation redundancy brings some advantages to the system:

- 1) The reliability of the system is increased. That is, even if one of the tethers fails, the system stays controllable and can continue to operate;
- 2) The tension in each of the tethers can be decreased and the loading made more uniform among the tethers, even in the presence of asymmetric wind conditions.
- 3) The size of tethers can be smaller since the tensions in the tethers are smaller.

- 4) The accuracy of positioning the receiver may be improved, such that the system becomes more stable in the presence of wind turbulence.

However, concurrently, some disadvantages are introduced:

- 1) The total tether weight is increased;
- 2) The number of winches is increased;
- 3) The total cost to build the system is increased;
- 4) The system becomes more complicated. The amount of necessary computation increases. In particular, substantial complexity is also added in finding the static equilibrium configuration and, possibly, in controlling the system because the forces in the system cannot be determined uniquely.

#### **4.2.2 Redundancy in Statics**

The system has three degrees of actuation redundancy, i.e., there are three more tethers than the minimum number necessary to maintain its equilibrium. When considering the force balance at the confluence point, the number of force equilibrium equations is three, but we have to find the tensions in six tethers. Thus the tension in each tether can not be determined uniquely, and the problem is considered to be statically indeterminate. The redundancy gives us the opportunity to utilize optimization techniques to solve the problem.

Fitzsimmons had an alternative solution for six-tether configuration. However, that solution was not general and could not handle arbitrary zenith and azimuth angles of the six-tethered system. It is more desirable to consider a more general solution. Looking back at Fitzsimmons' statics solution for the three-tether configuration of the system

(Section 3.2), we find that only two of the main steps need to be modified to extend the solution to a six-tether configuration. These are the shadowed blocks, B and F, in Figure 3.2. In both of these blocks, for the six-tether case, we will have more unknowns than equations, and we therefore have a choice of solutions.

Optimization techniques are used to find the best tension distribution among all the solutions to achieve the desired performance. The statically indeterminate problem then becomes a constrained optimization problem. The formulation and solution of the problem are now discussed in more detail.

### 4.2.3 Constrained Optimization Problem

In a general mathematical form, a constrained optimization problem is to determine an unknown vector  $\mathbf{x}^*$  that solves the problem

$$\text{minimize } f(\mathbf{x})$$

subject to:

$$a_i(\mathbf{x}) = 0 \quad i = 1, 2, \dots, p$$

$$b_j(\mathbf{x}) \leq 0 \quad j = 1, 2, \dots, q$$

where  $f(\mathbf{x})$  is called the objective function, it is a scalar quantity which can assume different forms; the equations  $a_i(\mathbf{x}) = 0$  are the equality constraints, while  $b_j(\mathbf{x}) \leq 0$  are the inequality constraints.

### 4.2.4 Nonlinear Optimizer CFSQP

The software CFSQP (C code for Feasible Sequential Quadratic Programming) [30] is a set of C functions for the optimization of a set of smooth objective functions

subject to general smooth constraints. It was originally developed at the Institute for Systems Research, University of Maryland. We obtained the non-profit version in late 1999 at no cost. Since then, the software has been further developed and transferred to AEM Design, Atlanta [31].

In the case as our problem, CFSQP tackles optimization problems of the form

$$\text{minimize } \max\{f_i(\mathbf{x})\} \quad i = 1, 2, \dots, p$$

where  $\mathbf{x}$  must satisfy the lower and upper bounds

$$\mathbf{b}_l \leq \mathbf{x} \leq \mathbf{b}_u$$

and constraints:

$$\text{Nonlinear inequalities:} \quad g_j(\mathbf{x}) \leq 0 \quad j = 1, 2, \dots, n_i$$

$$\text{Linear inequalities:} \quad g_j(\mathbf{x}) \leq 0 \quad j = n_i+1, \dots, t_i$$

$$\text{Nonlinear equalities:} \quad h_j(\mathbf{x}) = 0 \quad j = t_i+1, \dots, n_e$$

$$\text{Linear equalities:} \quad h_j(\mathbf{x}) = 0 \quad j = n_e+1, \dots, t_e$$

All the functions, including  $f_i(\mathbf{x})$ ,  $g_j(\mathbf{x})$ ,  $h_j(\mathbf{x})$  must be smooth.

Use of this solver does not require a feasible initial guess, i.e., a value of  $\mathbf{x}$ , which satisfies all constraints. If the initial guess provided by the user is infeasible, CFSQP first generates a feasible point for these constraints; subsequently the successive iterates generated by CFSQP all satisfy these constraints. The user must provide software functions that define the objective functions and constraint functions. Further, the user may either provide software functions to compute the respective gradients of  $f_i(\mathbf{x})$ ,  $g_j(\mathbf{x})$  and  $h_j(\mathbf{x})$  or require that CFSQP estimate them by forward finite differences [30].

### 4.2.5 Implementation in the Statics

When using Fitzsimmons' approach to obtain the statics solution, it is difficult to implement a single global performance measure for the problem because the statics problem has been split into sub-problems, two of which (Blocks B and F) need modification. We must therefore choose the objective functions in these sub-problems with caution. The approach taken to do this is now described.

#### **Block B: No-wind Analysis**

In the sub-problem of Block B in Figure 3.2, we choose to minimize the sum of the tether tensions squared, with the intention of minimizing the internal forces. This is chosen after comparing the results from different objective functions, as will be shown in Section 4.2.8.

Thus, the objective function to be minimized is

$$f_B = \sum_{i=1}^6 (H_{xi}^2 + H_{yi}^2 + V_i^2) \quad (4.7)$$

while the constraints are the force equilibrium equations at the CP:

$$\begin{aligned} \sum_{i=1}^6 H_{xi} &= 0 \\ \sum_{i=1}^6 H_{yi} &= 0 \\ \sum_{i=1}^6 V_i + W_p + T_L &= 0 \end{aligned} \quad (4.8)$$

where  $H_{xi}$  and  $H_{yi}$  are the components of  $H_i$ ;  $W_p$  is the weight of the payload platform;  $T_L$  is the leash tension under the no-wind condition.



The Equations (3.1) relating tension components  $H_i$ ,  $V_i$  and the unstretched lengths  $L_{0i}$  also become equality constraints, two for each tether (repeated here for convenience):

$$\begin{aligned} l_i &= \frac{H_i L_{0i}}{EA_0} + \frac{H_i L_{0i}}{W_i} \left[ \sinh^{-1} \frac{V_i}{H_i} - \sinh^{-1} \left( \frac{V_i - W_i}{H_i} \right) \right], \quad i = 1, \dots, 6 \\ h_i &= \frac{W_i L_{0i}}{EA_0} \left( \frac{V_i}{W_i} - \frac{1}{2} \right) + \frac{H_i L_{0i}}{W_i} \left\{ \left[ 1 + \left( \frac{V_i}{H_i} \right)^2 \right]^{1/2} - \left[ 1 + \left( \frac{V_i - W_i}{H_i} \right)^2 \right]^{1/2} \right\} \end{aligned} \quad (4.9)$$

where  $W_i$  is the weight of the tether,  $l_i$  and  $h_i$  are the horizontal and vertical components of the distance between the two endpoints of a tether (see Figure 3.3). Thus, equations (4.8) and (4.9) constitute 15 equations in 18 unknowns ( $H_i$ ,  $V_i$  and  $L_{0i}$  for  $i = 1, \dots, 6$ ), and the optimal solution will be found by minimizing the objective function Equation (4.7).

Furthermore, in order to avoid obtaining a solution with slack tethers, we place a constraint on each tether, to ensure that the vertical tension  $V_i$  at the top end of the tether is greater than the weight of the tether  $W_i$ . Therefore, we include six more constraints as follows:

$$W_i - V_i \leq 0 \quad i = 1, \dots, 6 \quad (4.10)$$

Thus, the underdetermined problem noted previously with 18 unknowns and 15 equality constraints is augmented to include these 6 inequality constraints.

#### **Block F: Unstretched Tether Length Adjustment**

The sub-problem of Block F in Figure 3.2, in which we must determine the unstretched tether length changes, also becomes indeterminate. This problem consists of

finding six unknowns,  $\Delta L_{0i}$  for  $i = 1, \dots, 6$ , while satisfying the three equality constraints which are the force equilibrium equations at the CP:

$$\begin{aligned} \sum_{i=1}^6 H_{xi} + D_{px} + T_{lx} - EA_0 \sum_{i=1}^6 \frac{d_{xi} \Delta L_{0i}}{L_{0i} (L_{0i} + \Delta L_{0i})} &= 0 \\ \sum_{i=1}^6 H_{yi} + D_{py} + T_{ly} - EA_0 \sum_{i=1}^6 \frac{d_{yi} \Delta L_{0i}}{L_{0i} (L_{0i} + \Delta L_{0i})} &= 0 \\ \sum_{i=1}^6 V_i + W_p + T_{lz} - EA_0 \sum_{i=1}^6 \frac{d_{zi} \Delta L_{0i}}{L_{0i} (L_{0i} + \Delta L_{0i})} &= 0 \end{aligned} \quad (4.11)$$

In general, for the triple-tethered system, we find that the winch forces and the unstretched lengths of the tethers in the final statics solution are very close to those in the no-wind analysis. This implies that the effect of the wind on the tether equilibrium is not very significant. For this reason, in this sub-problem, we choose to minimize the sum of the length change squared as

$$f_F = \sum_{i=1}^6 \Delta L_{0i}^2 \quad (4.12)$$

in the expectation that the optimal solution thus obtained will be close to the solution of the no-wind analysis. This makes the minimization of the tension norms in Block B approximately global.

When implementing CFSQP in the existing program to solve this problem, we again provide the exact analytical form for the Jacobian matrix instead of using a finite difference method which might slow down the convergence.

It should be noted that the optimizer can also be used for cases in which there exists a unique solution (e.g. the triple-tethered case). In the interest of consistency, we use this optimization solver to solve the determinate statics problem of the triple-tethered systems as well.

#### 4.2.6 Dynamics of the Six-Tethered System

The tethered aerostat dynamics model in [24] was set up in such a way that it is very easy to expand the model from a three-tether configuration to a six-tether configuration. In Nahon's model, forces exerted on each segment of the tethers, tension and drag, are calculated in generic subroutines. Except for some minor changes, the dynamics model of the tethered aerostat system stays almost untouched when simulating the six-tethered aerostat system. It should be noted that the controller used, described in Section 4.1, is purely kinematically based. Normally, we would expect that a redundantly-actuated system should also include some form of force control.

#### 4.2.7 Statics Results and Verification

We are now interested in seeing how the statics and dynamics solutions correspond to each other, as we did in the case of 3 tethers. Some parameter changes used for the six-tether cases are listed in Table 4.1. They include a decrease in the tether base radius and the cable diameter. These are indicative of one advantage that the 6-tether configuration brings to the system: with more tethers employed in the system, the system size can be reduced [23].

Table 4.1 Parameter changes

Parameter Configuration	Base radius (m)	Cable diameter (m)
3-tether configuration	1200	0.0185
6-tether configuration	635	0.0142

Figure 4.4 shows the dynamic simulation results for the six-tethered system with the new statics solution as the initial condition. The same simulation cases are used as those in Table 3.1 for easy comparison. From Figure 4.4, we can see that the largest steady-state error in the focal plane is about 1.1 mm which occurs in Case 2; the largest error out of the focal plane is close to 2.1 mm which occurs in Case 3.

The mismatch is of the same order as that in the three-tether configuration (Figure 3.10). This verifies the correctness of the statics and dynamics models of the six-tethered aerostat system.

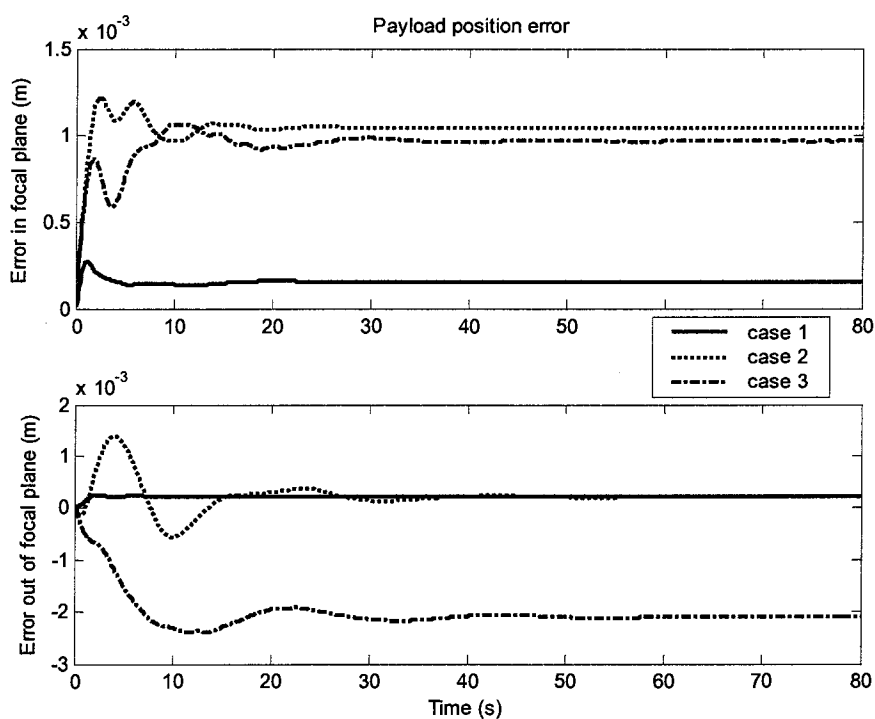


Figure 4.4 Matching simulations for the six-tethered spherical aerostat system

### 4.2.8 Optimization Results and Discussion

A few different objective functions were evaluated in the no-wind analysis, Block B in Figure 3.2, before deciding on the objective function described in Section 4.2.5. Some results of the study are presented and discussed in this section. The different objective functions evaluated are shown in Table 4.2, where  $T_i$  is the magnitude of the tension at the top node of tether  $i$ ,  $T_i = \sqrt{H_i^2 + V_i^2}$ ,  $d_i$  is the straight line distance between the base node (winch point) and the top node of tether  $i$  (Figure 3.4). Objective functions 1 and 2 are chosen with the intention to minimize the internal forces; objective functions 3 and 4 are chosen with the intention to maximize the stiffness of the system since the shorter  $L_{0i}$ , the higher tension in tether  $i$ , and the stiffer the system.

Table 4.2 Objective functions for no-wind analysis

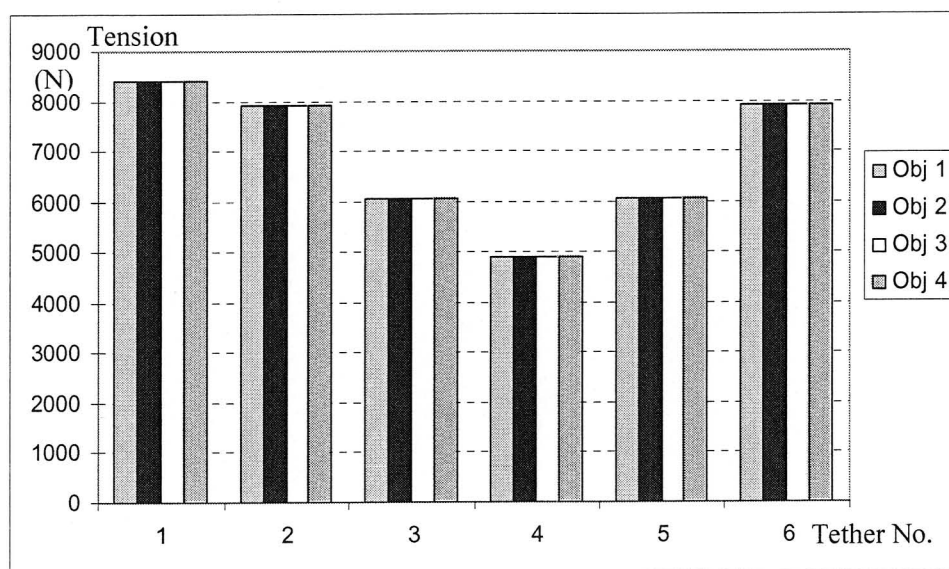
No.	Objective Function	Note
1	$\sum_{i=1}^6 T_i$	To minimize the sum of tensions
2	$\sum_{i=1}^6 T_i^2$	To minimize the sum of tensions squared
3	$\sum_{i=1}^6 L_{0i}^2$	To minimize the sum of unstretched tether lengths squared
4	$\sum_{i=1}^6 \left( \frac{L_{0i}}{d_i} \right)^2$	To minimize the sum of squared ratios between the unstretched length and the straight-line distance between the two ends of the tether

Figure 4.5 shows the resulting tensions in the tethers with different objective

functions used in Block B (the no-wind analysis) as discussed in Section 4.2.5 and with the consideration of the wind. Again, the cases shown are the same as described in Table 3.1.

From the statics results shown in Figure 4.5, we can see:

- 1) The same result is obtained for the case with zero zenith angle and azimuth angle with all the objective functions tested.
- 2) The results with objective function 2 show the most evenly distributed tensions among all tethers in all the cases tested. The most tensioned tether, tether 1 in Case 2 or tether 2 in Case 3, has the smallest tension; the least tensioned tether, tether 6 in Case 2 or tether 3 in Case 3, has the highest tension. This more even distribution led us to select objective function 2 for the no-wind analysis.



(a) Case 1:  $\theta_{za} = \theta_{az} = 0$

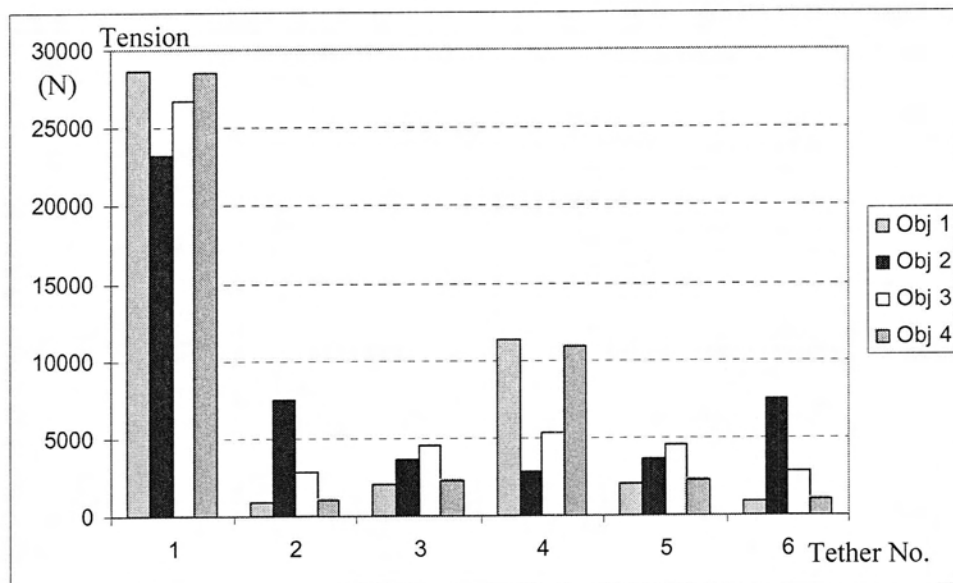
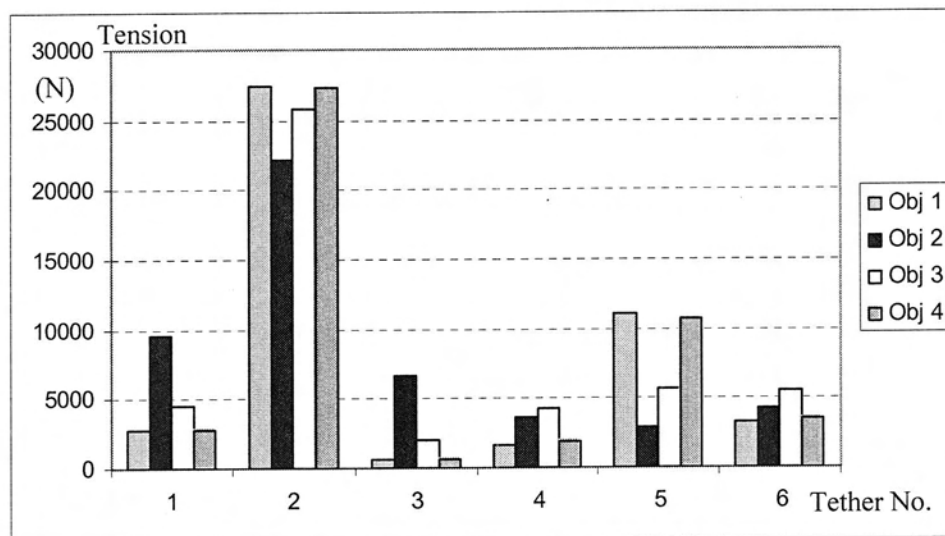
(b) Case 2:  $\theta_{za} = 60^\circ, \theta_{az} = 0$ (c) Case 3:  $\theta_{za} = \theta_{az} = 60^\circ$ 

Figure 4.5 Tether tensions in statics using different objective functions

(Conditions: wind speed = 10 m/s, wind angle =  $180^\circ$ )

The results for Case 1 led to the question whether the solution for the configuration  $\theta_{za} = \theta_{az} = 0^\circ$  is unique. We notice that in all the objective function in Table 4.2, all tethers are treated equally. We therefore choose an asymmetric objective function in which we only minimize the square of the tension in tether 1, i.e.,  $f = T_1^2$ . The result using this objective function is shown in Figure 4.6, marked as “Obj 5” in the graph, and compared to that from objective function 2. This result was then used as an initial state for the dynamics simulation. The steady state payload position error was less than 1 mm and can therefore be considered be a true equilibrium. Since the results for these two objective functions are different, we conclude that the solution we previously obtained is not unique for this system configuration.

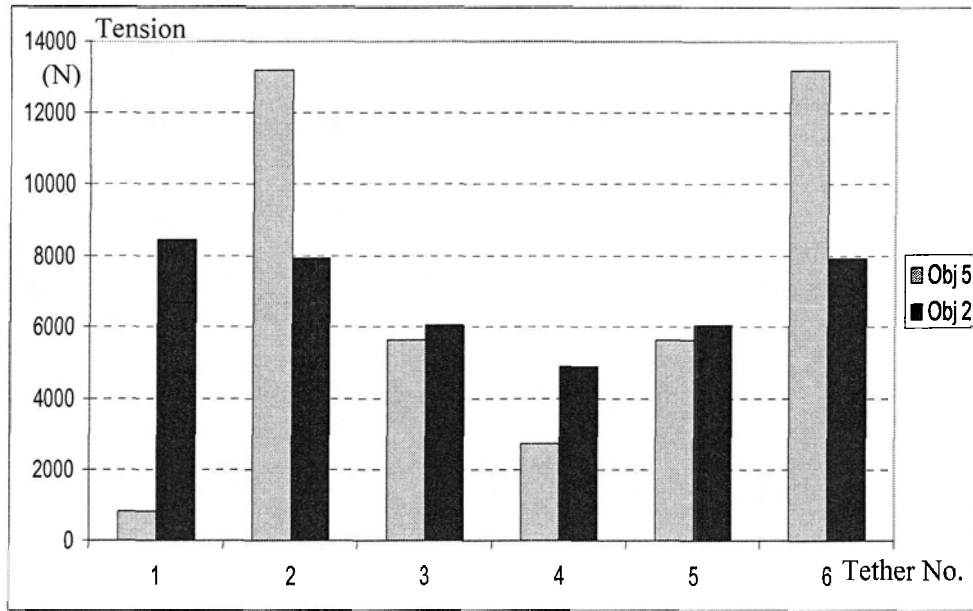


Figure 4.6 Results for different objective functions,  $\theta_{za} = \theta_{az} = 0$



Dynamics simulations with a wind speed of 10 m/s and wind direction of  $180^\circ$  and different zenith and azimuth angles were also performed with these different objective functions. The results are shown in Figure 4.7 and 4.8. The case numbers in those figures are defined in Table 4.3. The objective function numbers in Table 4.3 correspond to those in Table 4.2.

Table 4.3 Case number definitions for Figure 4.7

		$\theta_{za} = \theta_{az} = 0$	$\theta_{za} = 60^\circ, \theta_{az} = 0$	$\theta_{za} = \theta_{az} = 60^\circ$
	No.	1	2	3
Objective function	1	11	12	13
	2	21	22	23
	3	31	32	33
	4	41	42	43
Notes		Case 1 in Figure 4.4	Figure 4.7 (a)	Figure 4.7 (b)

From the dynamics results shown in Figure 4.7 and 4.8, we can see:

- 1) The maximum payload position error in the focal plane is 6.8 mm for objective function 1, zenith angle  $60^\circ$  and azimuth angle  $60^\circ$ . The maximum error out of the focal plane is 2.3 mm for the same objective function with the same system configuration.
- 2) Objective functions 1 and 4 result in similar magnitude of errors in both configurations, and these are worse than objective functions 2 and 3.

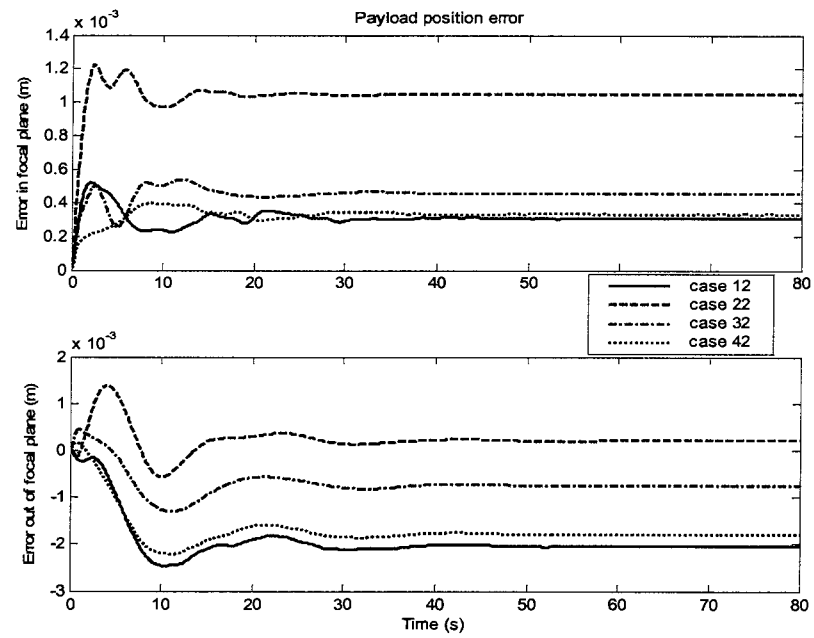
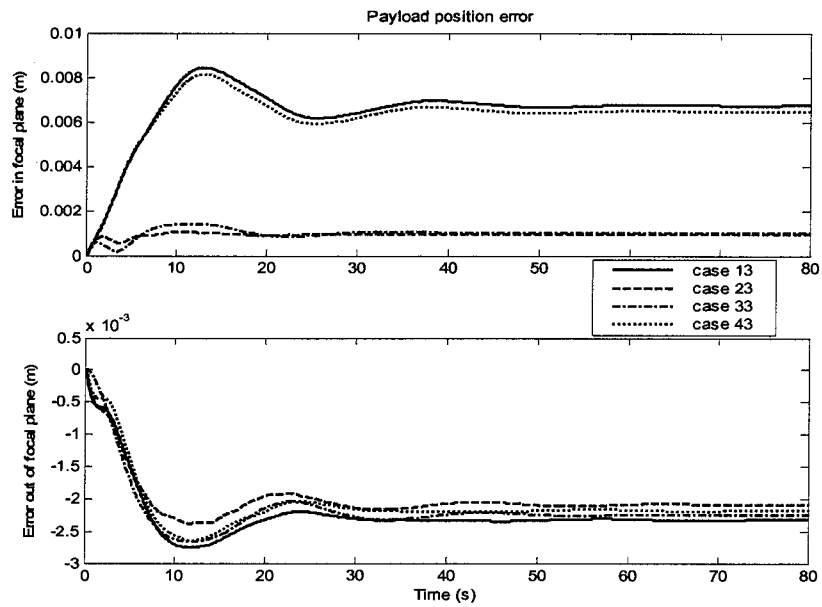
(a)  $\theta_{xa} = 60^\circ, \theta_{az} = 0$ (b)  $\theta_{xa} = \theta_{az} = 60^\circ$ 

Figure 4.7 Dynamics simulation results of the payload position using different objective functions for the statics initial condition

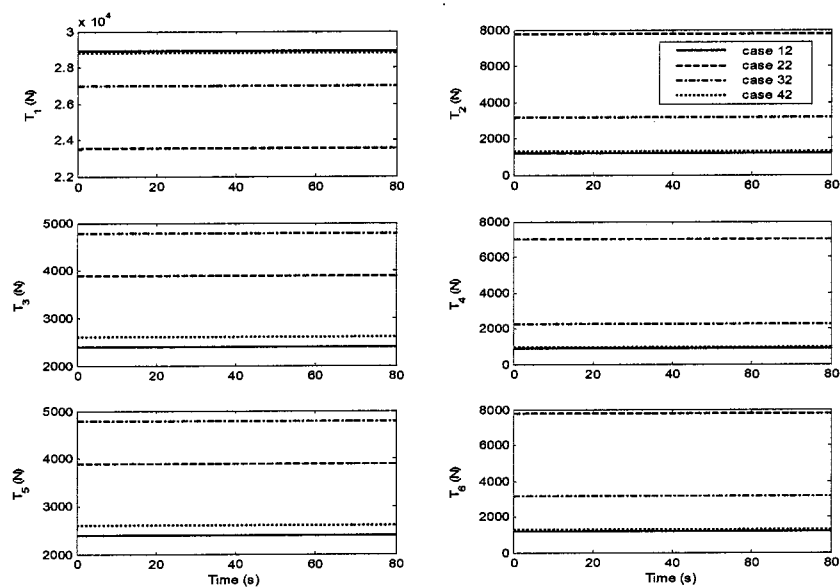
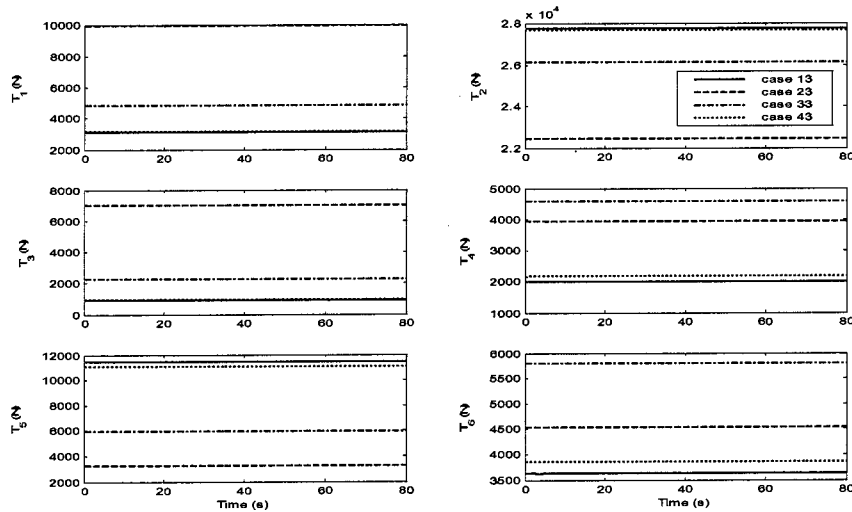
(a)  $\theta_{za} = 60^\circ, \theta_{az} = 0$ (b)  $\theta_{za} = \theta_{az} = 60^\circ$ 

Figure 4.8 Dynamics simulation results of the tether tensions using different objective functions for the statics initial condition

- 3) The tension seems to stay at their initial values throughout the simulation for all cases. The fluctuations are so small that they are not apparent in the graphs.

The errors in some cases are larger than those previously shown in Figures 3.10 and 4.4. Besides the contribution from the model differences between the statics and dynamics model, this is largely due to the bigger error tolerance  $\varepsilon_f$  in Inequality (3.13) when smaller  $\varepsilon_f$  can not be satisfied within 50 iterations. Nevertheless, these errors are still quite small in comparison with the system scale. The results shown in Figure 4.7 further verify the correctness of our system model including both the statics and dynamics components.

#### 4.2.9 Dynamics Results and Discussion

Dynamics simulation results are further investigated for the redundantly actuated system in order to examine its performance with and without control. As discussed in Section 4.2.5 and 4.2.8, Objective function 2 in Table 4.2 is selected for the no-wind analysis. A turbulence model presented in [24] was superimposed on the wind profile for all the simulations. All simulations shown used the same wind condition: a mean wind speed of 10 m/s and a wind angle of 180°.

Figures 4.9 and 4.10 present the simulation results with and without a controller for zero zenith angle and zero azimuth angle ( $\theta_{za} = \theta_{az} = 0$ ). Figures 4.11 and 4.12 present the simulation results with and without a controller for 60° zenith angle and 0 azimuth angle ( $\theta_{za} = 60^\circ$ ,  $\theta_{az} = 0$ ). The controllers in these cases are the same as those used in Nahon's triple-tethered system simulation [24], which are  $k_d = 2$  s,  $k_p = 5$ ,  $k_i = 5$  s<sup>-1</sup> for  $\theta_{za} = \theta_{az} = 0$

and  $k_d = 4 \text{ s}$ ,  $k_p = 1$ ,  $k_i = 1 \text{ s}^{-1}$  for  $\theta_{za} = 60^\circ$ ,  $\theta_{az} = 0$  for easy comparison. The position errors for the triple-tethered system are also shown along with those for the six-tethered system in Figures 4.9 and 4.11.

Table 4.4 lists the payload position errors for the cases considered (see also Figures 4.9 and 4.11). It is interesting to see that the payload position errors are relatively small even in the uncontrolled cases with compared to those for the triple-tethered system. For the controlled cases, results for  $\theta_{za} = \theta_{az} = 0$  show similar magnitude of payload position error for the 3-tether and 6-tether cases; for  $\theta_{za} = 60^\circ$ ,  $\theta_{az} = 0$ , the maximum error in the focal plane is about 0.02 m for the six-tethered system and 0.28 m for the triple-tethered system, the maximum error out of the focal plane is 0.12 m for the six-tethered system and 0.23 m for the triple-tethered system. The errors for the six-tethered system may be further reduced by tuning the controller gains. These results suggest that the six-tethered system is much stiffer than the triple-tethered system.

Table 4.4 Payload position errors for the redundantly actuated system

Conditions		Maximum position error for <i>uncontrolled</i> system		Maximum position error for <i>controlled</i> system	
Payload position	Wind condition	<i>in</i> the focal plane (m)	<i>out</i> of the focal plane (m)	<i>in</i> the focal plane (m)	<i>out</i> of the focal plane (m)
$\theta_{za} = 0$ $\theta_{az} = 0$	$U_g = 10 \text{ m/s}$	0.26	0.14	0.02	0.04
$\theta_{za} = 60^\circ$ $\theta_{az} = 0$	$\theta_w = 180^\circ$	0.09	0.35	0.02	0.12

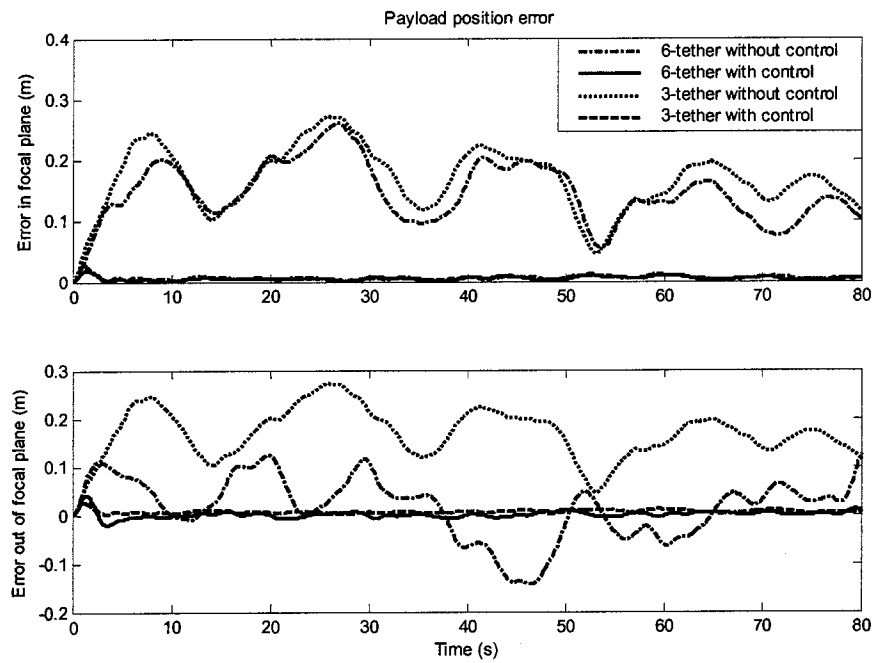


Figure 4.9 Payload motion for  $\theta_{zd} = \theta_{az} = 0$

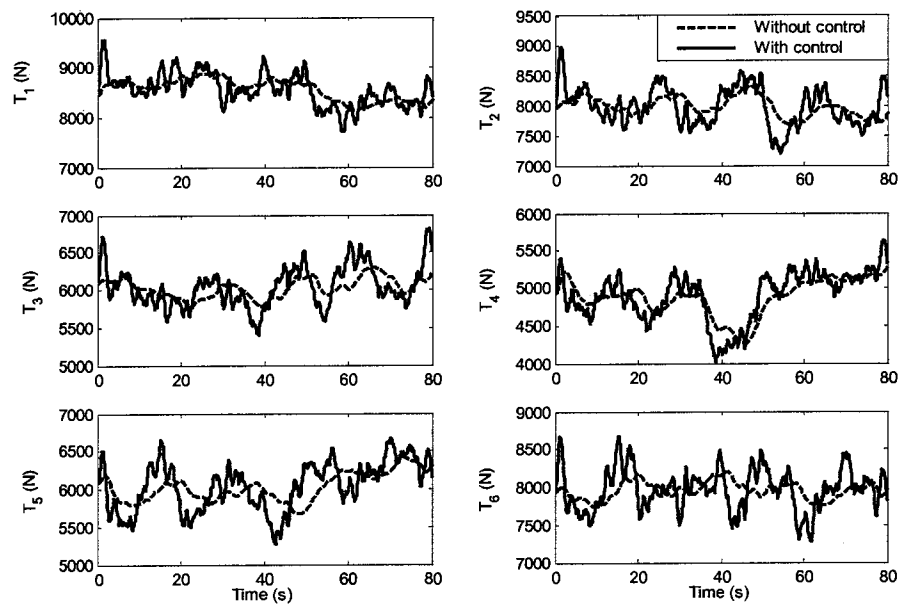


Figure 4.10 Tether tension for  $\theta_{zd} = \theta_{az} = 0$

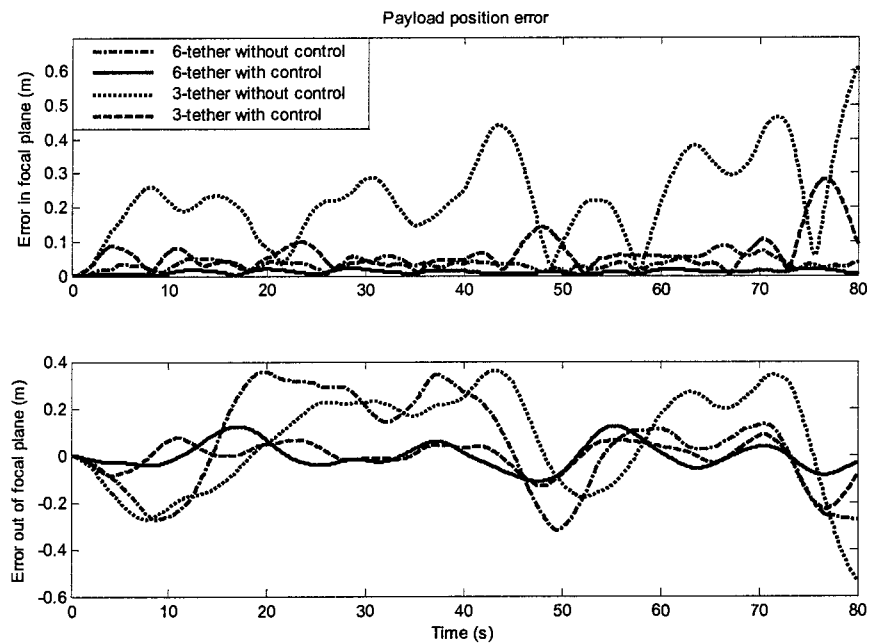


Figure 4.11 Payload motion for  $\theta_{za} = 60^\circ$ ,  $\theta_{az} = 0$

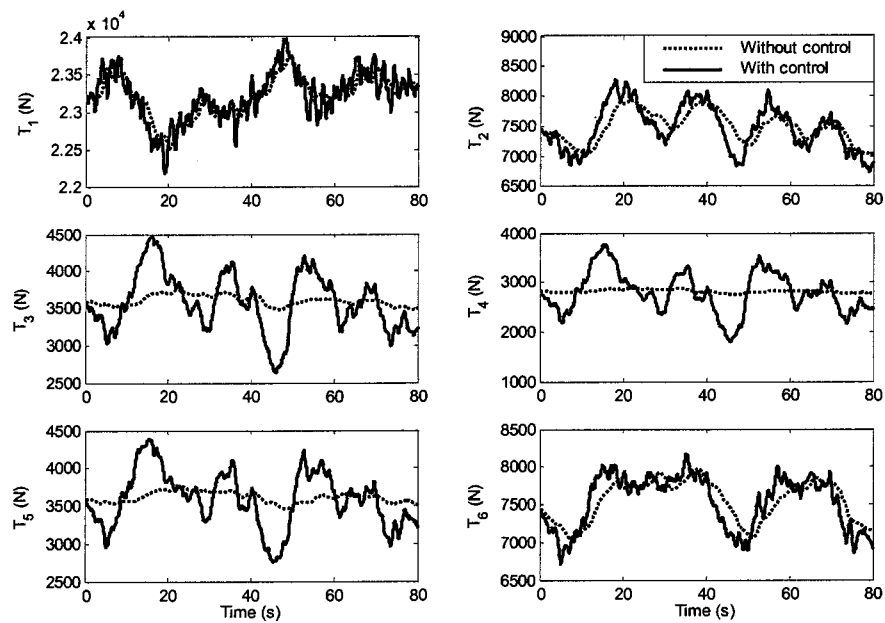


Figure 4.12 Tether tension for  $\theta_{za} = 60^\circ$ ,  $\theta_{az} = 0$

It should also be noted that the vortex-induced oscillations typical of the spherical aerostat are not included in the spherical aerostat model used here. The results would be worsen as shown in [32] if they were included.

As expected, the tensions (Figures 4.10 and 4.12) are much smaller than those for the triple-tethered system (shown later in Figures 5.14 and 5.18) due to the increase in the number of tethers.

### 4.3 Determinate System

With the use of six tethers, it is not only possible to control the position of the payload platform, but also to control its orientation. In this case, the system becomes a determinate system: using six adjustable tethers to control the six DOFs of the airborne platform (Figure 4.9).

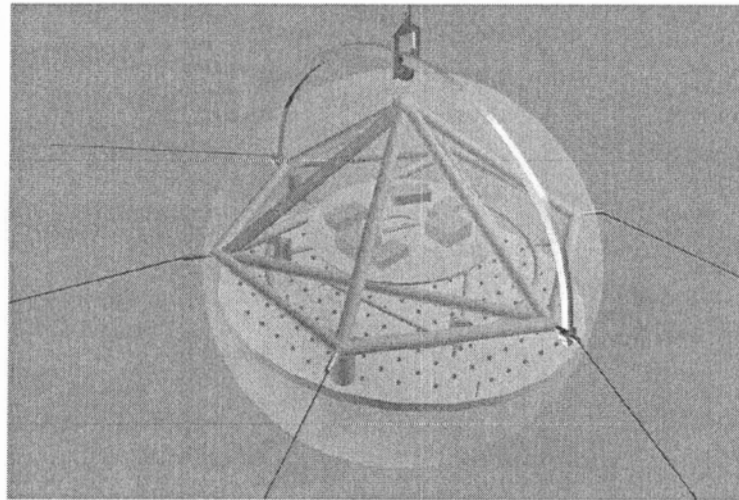


Figure 4.13 The Airborne platform view [5]



### 4.3.1 Purpose

The airborne payload platform of the telescope contains the LAR feed which receives the radio signal from the reflector on the ground. The axis of symmetry of the feed has to remain pointed to the center of the reflector [33], thus requiring feed orientation control. We are therefore interested in knowing how well we can achieve the desired orientation by adjusting the tether length alone, without using any additional orienting mechanism. This will give us the information needed to later design a mechanism to fine tune the feed orientation.

### 4.3.2 The 6-DOF Payload Platform Model

The payload platform is subject to gravity, aerodynamic forces and tensions from the tethers attached to it as presented in Section 3.1. When modelling the platform's 6 degrees of freedom, it is assumed that the six main tethers are attached to the payload platform at the edge of a disk, evenly distributed,  $60^\circ$  apart from each other (Figure 4.9). The leash is assumed to be attached at the mass center of the payload platform. The orientation of the payload platform is defined by a Z-Y-Z Euler angle set  $(\alpha, \beta, \gamma)$  discussed in Section 2.3.2.

In this study, we set the desired orientation of the airborne platform to be  $(\alpha = \theta_{az}, \beta = \theta_{za}, \gamma = -\theta_{az})$  where  $\theta_{za}$  and  $\theta_{az}$  are the zenith and azimuth angles of the airborne platform respectively (Figure 1.3). The first two angles  $(\alpha = \theta_{az}, \beta = \theta_{za})$  ensure that the axis of symmetry of the payload (the feed) points to the center of the reflector. Keeping the third angle at  $\gamma = -\theta_{az}$  will keep each attachment point approximately aligned with the winch to which it is connected.

As we did for the redundantly actuated system, we would like to start the dynamics simulation from a static equilibrium. In the next section, we discuss how the statics solution was modified to handle the determinate system.

#### 4.3.2.1 Statics

As discussed in Section 4.2.5, Blocks B and F in Figure 3.2 have been modified to use the CFSQP optimization solver to accommodate the six-tethered redundantly-actuated system. In order to add the consideration of the payload platform orientation into the statics solution, we need to make some modifications to the procedure detailed in Figure 3.2.

When the payload platform is modelled as an object with 6-DOF, not only should the resultant force acting on it be zero in equilibrium, but also the resultant moment should be zero. We therefore added the moment equations in Blocks B and F, which made Block B a determinate problem with 18 unknowns and 18 equality constraints and Block F with 6 unknowns and 6 equality constraints. As well, we added a check for the resultant moment about the mass center in Block E. With these modifications, the optimization solver CFSQP employed in Blocks B and F should yield a unique solution that would satisfy all the constraints. However, tests showed that the solver would not converge when the zenith angle of the payload platform becomes large ( $>45^\circ$ ). This result was verified by also trying to find a solution using Matlab's 'fsolve' command, which had similar difficulties.

The reason we have difficulty in obtaining a static equilibrium for some cases may be due to the approach used in Fitzsimmons' solution. It may also be because of

system limitations. Even though we have six tethers to control the six degrees of freedom of the payload platform, the orientation workspace may be quite limited.

As a compromise solution, we chose to ignore the payload platform moment equations in the statics solution. Instead, we simply changed the positions of the tether top nodes from the CP to the positions of the attachment points on the payload platform. Everything else in the statics remained unchanged from the redundantly-actuated system. Thus we did not include the moment equations of the payload platform in Block B or F, nor did we check the resulting moment in Block E. Therefore, Block B remains a redundant problem with 15 equations and 18 unknowns as discussed in Section 4.2.5, the objective function used for the redundant problem is the same as  $f_B$  in Equation (4.7); Block F remains the same as for the redundantly-actuated case with 3 equations and 6 unknowns, and using objective function  $f_F$  as in Equation (4.12). In this approach, although the moment about the CP is not accounted for, the desired attachment points are a function of the desired payload platform orientation. Therefore, we can expect to observe an initial transient motion in the dynamics since this solution is not a true equilibrium. That transient should occur primarily in the payload platform rotational motion. The translational motion should be reasonably steady since the forces are balanced by the statics solver.

#### 4.3.2.2 Dynamics

There are two main modifications to the dynamics model for this determinate system relative to that for the redundantly actuated system.

Firstly, the rotational motion equations of the payload platform are added in the dynamics model. The moments of all forces are summed up about the center of the payload in the body-fixed frame of the payload platform. The vector form of the moment equation can be written as

$$\mathbf{M}_p = \mathbf{I}_p \dot{\boldsymbol{\omega}}_p + \boldsymbol{\omega}_p \times \mathbf{I}_p \boldsymbol{\omega}_p \quad (4.13)$$

where  $\mathbf{M}_p$  is the sum of moments applied to the payload platform about its center of mass;  $\mathbf{I}_p$  is the moment of inertia tensor;  $\boldsymbol{\omega}_p$  is the angular velocity vector. There is no added moment of inertia tensor considered in Equation (4.10) since the added moment of inertia for a sphere is zero [34]. The external forces that contribute to the sum of moments are the tether tensions from the six main tethers. All other forces including the aerodynamic drag and tension from the leash are applied to the center of mass, thus have no contribution to the sum of moments. Therefore,  $\mathbf{M}_p$  can be expressed as

$$\mathbf{M}_p = \sum_{i=1}^6 \mathbf{r}_i \times \mathbf{T}_i \quad (4.14)$$

where  $\mathbf{r}_i$  is the position of the  $i$ -th attachment point from the payload mass center, and  $\mathbf{T}_i$  is the tension at the top node of tether  $i$ .

Secondly, the winch controllers have to be modified since our control objective is no longer the CP position only, but also includes the desired orientation of the payload platform. Winch controllers similar to those discussed in Section 4.1 are implemented to achieve this.

Instead of using the CP as the desired position of the top nodes of the tethers, the desired positions of the top nodes of the tethers become the attachment points on the payload platform. The attachment points are fixed in the body-fixed frame of the payload.

They become functions of the desired position and orientation of the payload platform when mapped into the inertial frame  $O_I X_I Y_I Z_I$  (Figure 2.1) by the transformation matrix  ${}^I_B \mathbf{T}_{zyz}$  which is a function of the Z-Y-Z Euler angle set  $(\alpha, \beta, \gamma)$  of the payload platform as defined in Equation (2.5).

Figure 4.14 depicts this approach. The desired top node position of the  $i$ -th tether can be calculated by

$$\mathbf{p}_d^i = \mathbf{p}_{CP} + {}^I_B \mathbf{T}_{zyz} \mathbf{r}_i \quad i = 1, \dots, 6 \quad (4.15)$$

where  $\mathbf{p}_d^i$  is the position vector of the desired top node position of the  $i$ -th tether in the inertial frame;  $\mathbf{p}_{CP}$  is the center of payload position in the inertial frame.

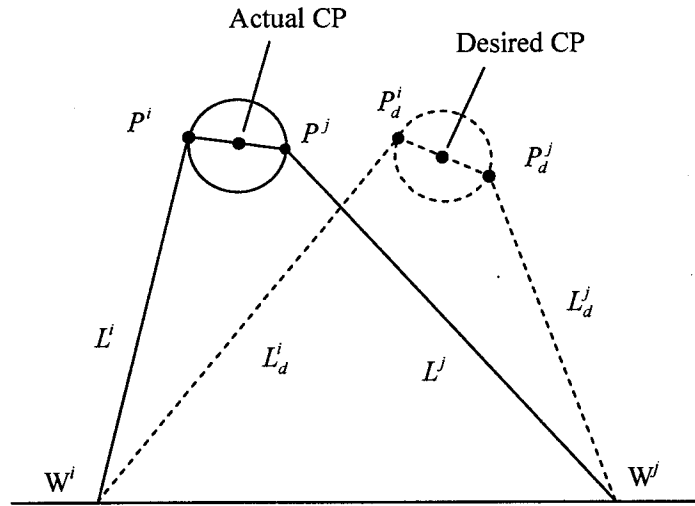


Figure 4.14 2-D illustration of the winch controller

Assuming  $\mathbf{p}_d^i = (x_c^i, y_c^i, z_c^i)^T$ , the actual location of the top node of the  $i$ -th tether is at  $\mathbf{p}^i (x^i, y^i, z^i)$ , and the  $i$ -th winch is at  $\mathbf{w}^i (x_w^i, y_w^i, z_w^i)$ , we can define the desired and actual distances from each winch to  $\mathbf{p}_d^i$  as

$$L_d^i = \|\mathbf{p}_d^i - \mathbf{w}^i\|, \quad L^i = \|\mathbf{p}^i - \mathbf{w}^i\| \quad (4.16)$$

The same control scheme as Equation (4.6) can be applied to this case, which is rewritten here for the  $i$ -th winch controller:

$$\dot{L}_{u1}^i = \dot{L}_{u10}^i - k_d(\dot{L}_d^i - \dot{L}^i) - k_p(L_d^i - L^i) - k_i \int (L_d^i - L^i) dt \quad (4.17)$$

The motivation of this approach is that when positions of the top nodes of all tethers are controlled to their desired positions, the payload platform would be at its desired position and with its desired orientation.

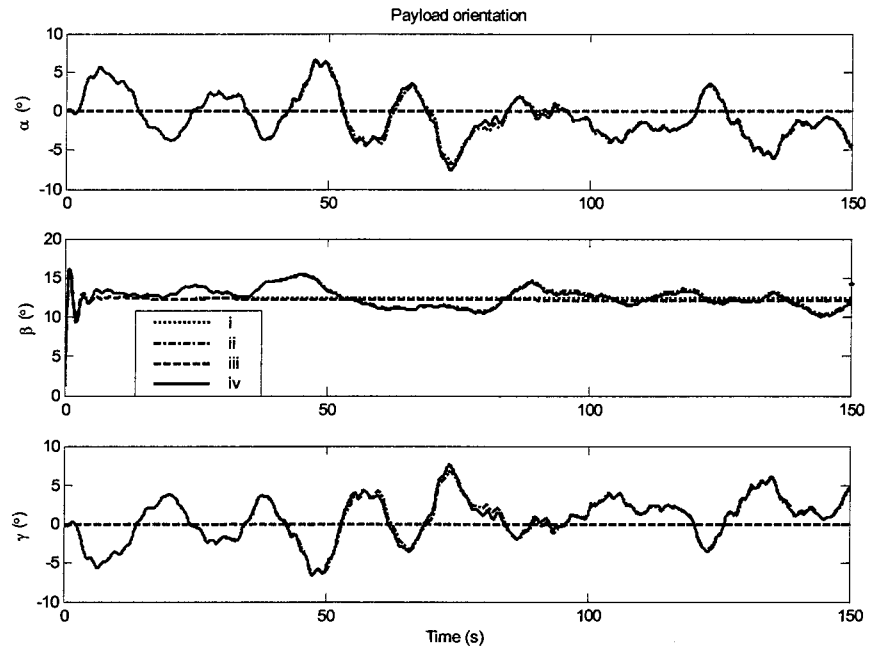
### 4.3.3 Results and Discussion

To investigate the performance of the determinate 6-tether solution, dynamics simulations were performed for configurations with different zenith and azimuth angles with the same wind conditions as in previous simulations: a gradient wind speed of 10 m/s and a wind angle of 180°.

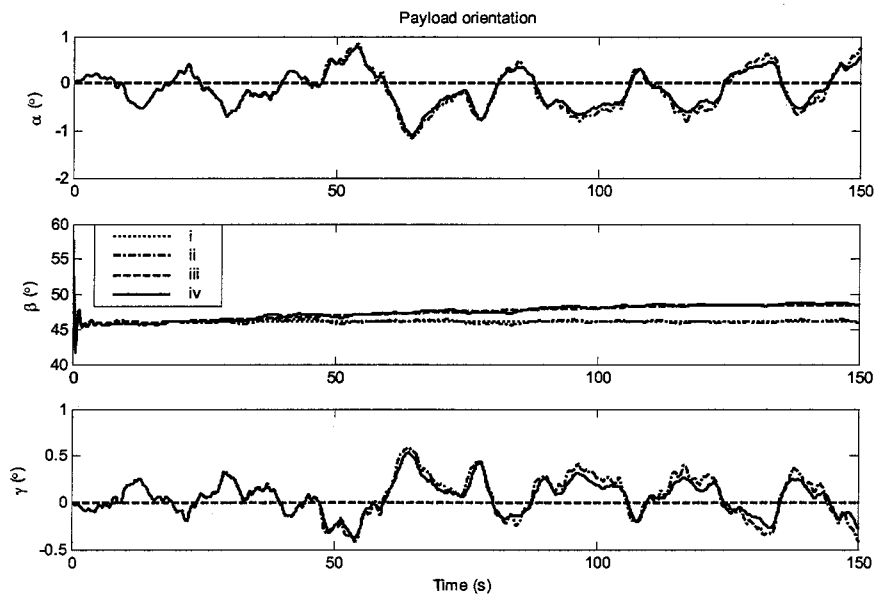
Figures 4.15 – 4.17 show the results of dynamics simulations for the conditions shown in Table 4.5 for each of the three cases of Table 3.3.

Table 4.5 Simulation conditions

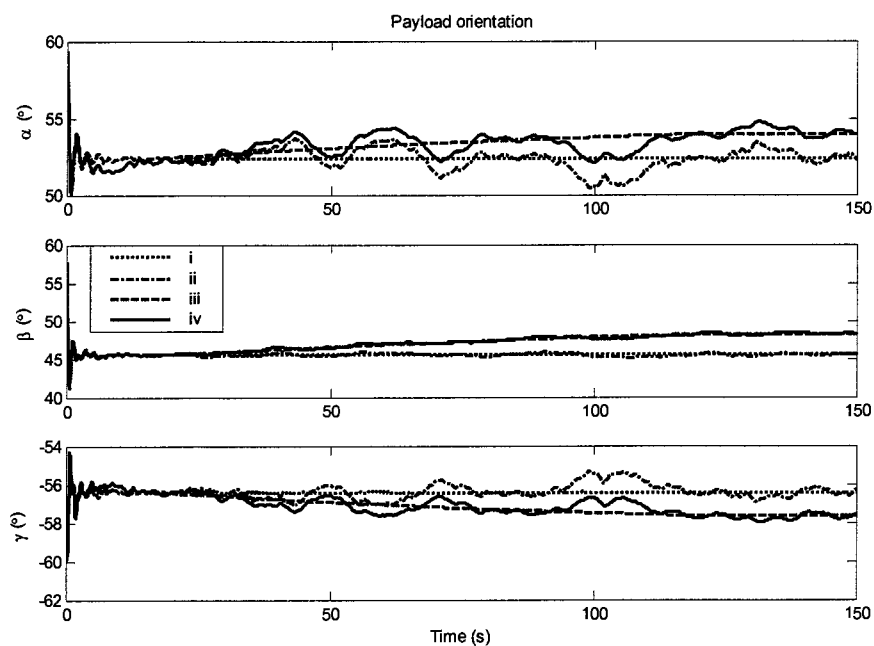
Condition	Turbulence	Winch controller	Plot line style
i	No	No	Dotted
ii	No	Yes	Dashed
iii	Yes	No	Dash-dotted
iv	Yes	No	Solid



(a) Case 1:  $\theta_{za} = \theta_{az} = 0$

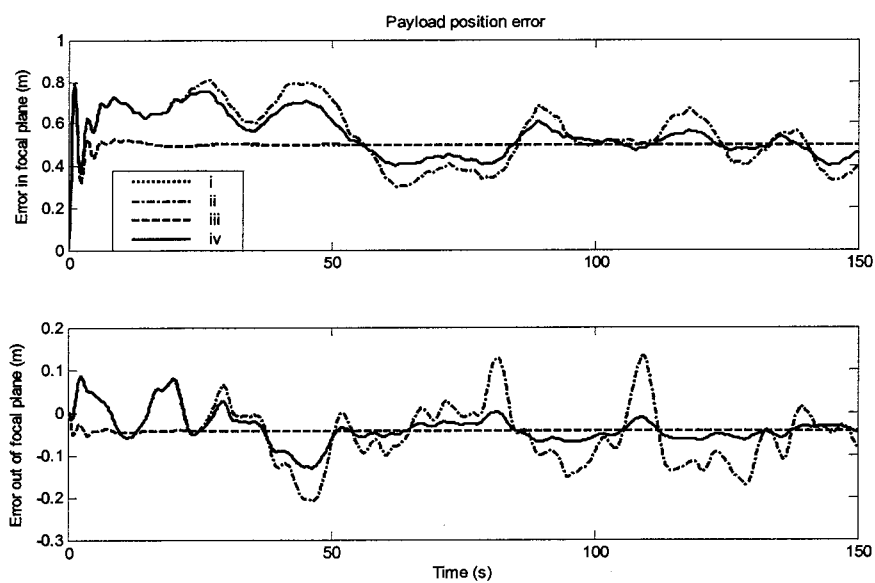


(b) Case 2:  $\theta_{za} = 60^\circ$ ,  $\theta_{az} = 0$



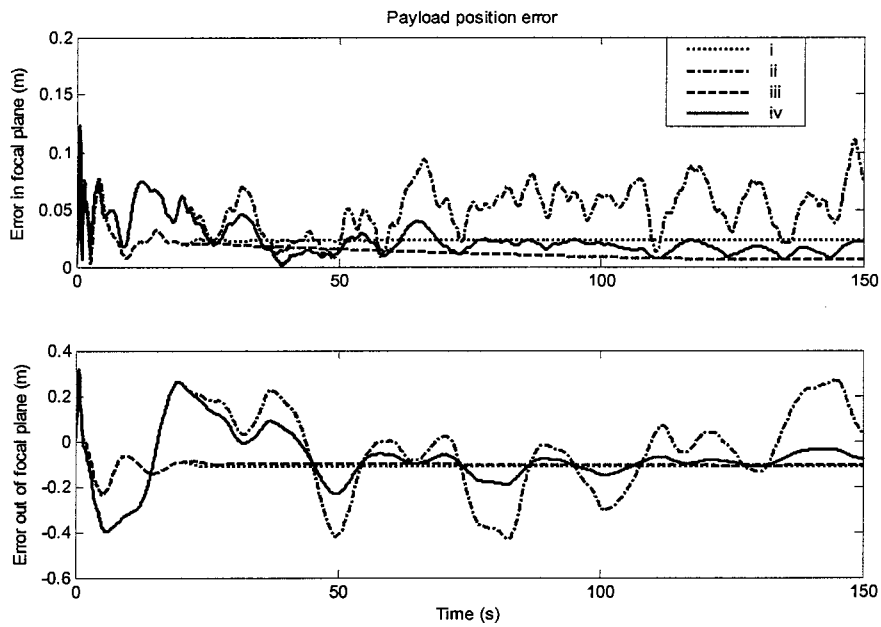
(c) Case 3:  $\theta_{za} = \theta_{az} = 60^\circ$

Figure 4.15 Payload platform orientation

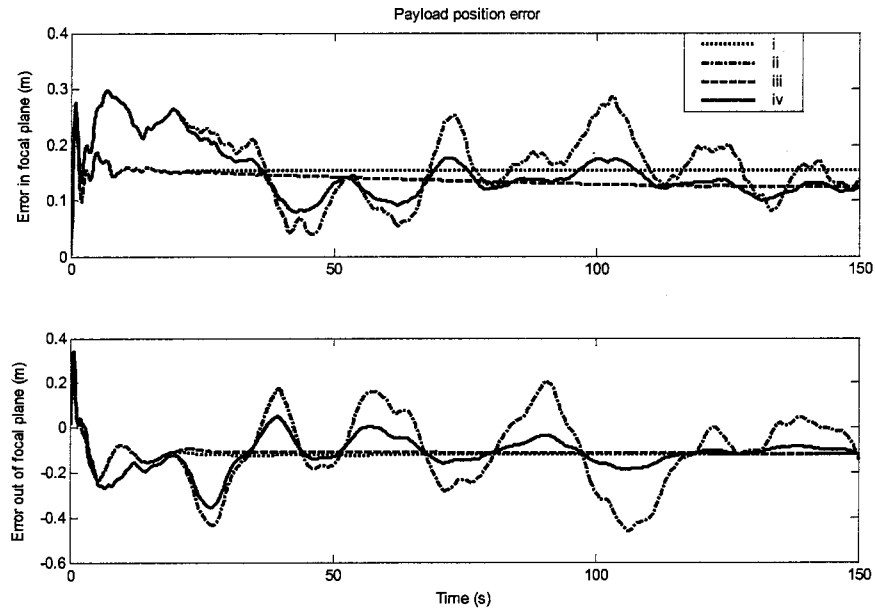


(a) Case 1:  $\theta_{za} = \theta_{az} = 0$



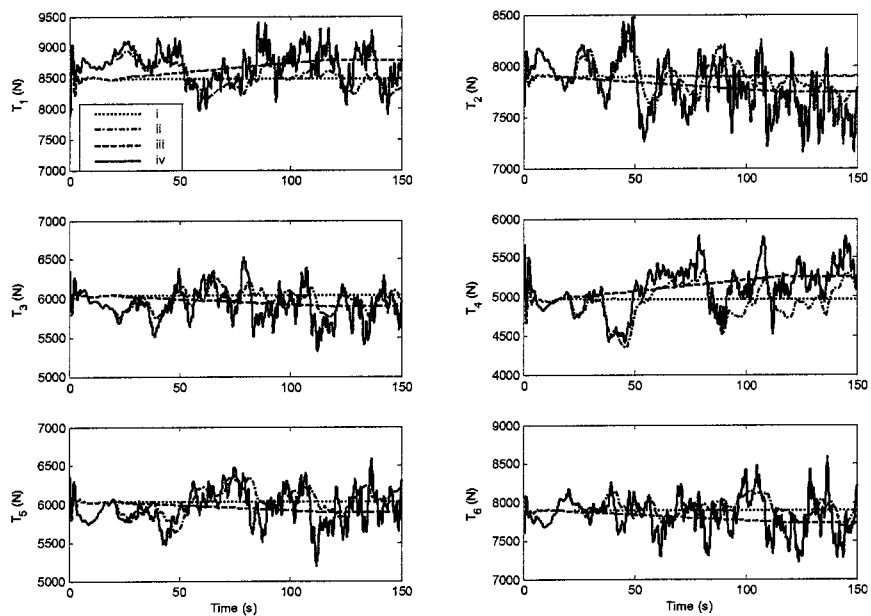
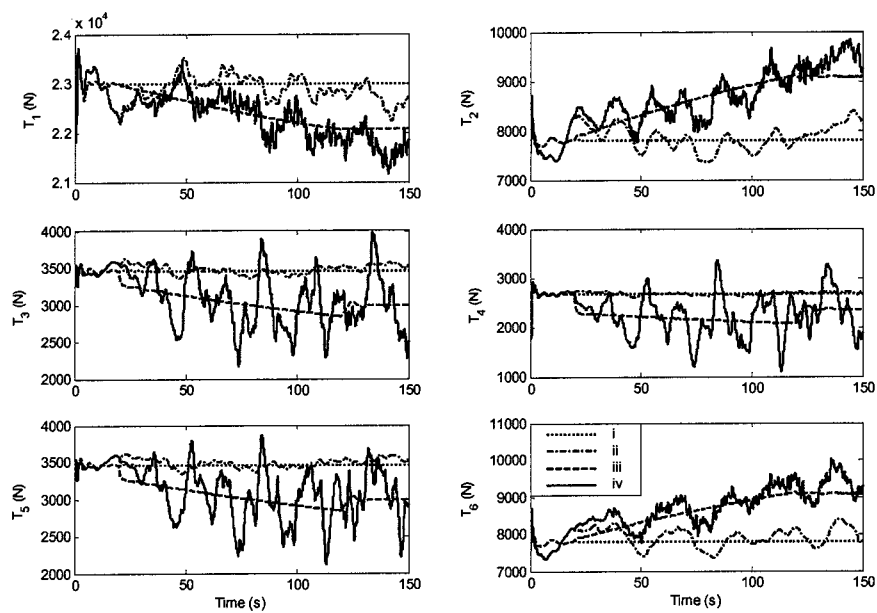


(b) Case 2:  $\theta_{za} = 60^\circ$ ,  $\theta_{az} = 0$



(c) Case 3:  $\theta_{za} = \theta_{az} = 60^\circ$

Figure 4.16 Payload position error

(a) Case 1:  $\theta_{za} = \theta_{az} = 0$ (b) Case 2:  $\theta_{za} = 60^\circ$ ,  $\theta_{az} = 0$

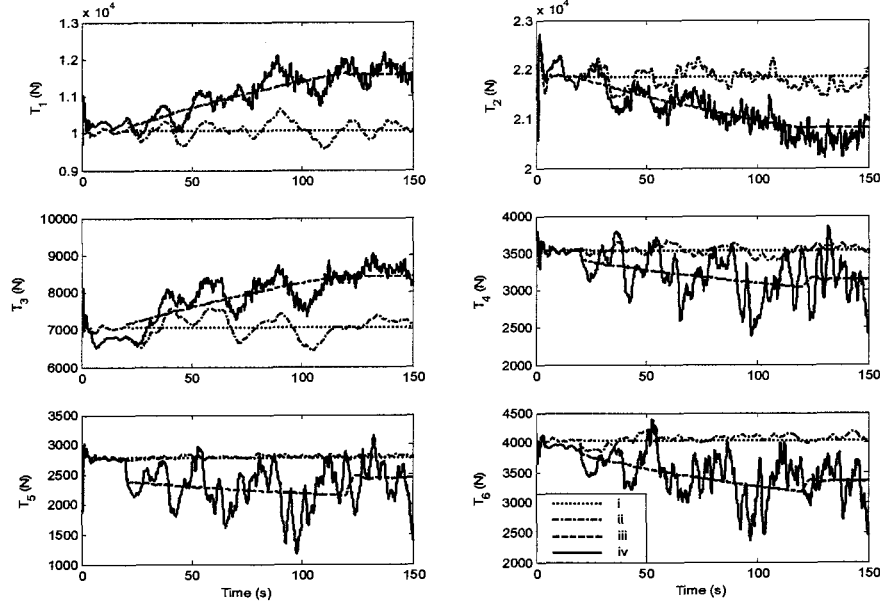
(c) Case 3:  $\theta_{za} = \theta_{az} = 60^\circ$ 

Figure 4.17 Tether tensions

In the absence of control and turbulence, we can see from the dotted lines in Figures 4.15-4.17 (in Figure 4.15 (a), (b) and Figure 4.16 (a) the dashed lines overlay the dotted lines) that the system deviates from the initial condition (the statics solution) and stabilizes to a steady states condition in 10- 20 seconds. The transition is reasonable since the statics solutions were not true equilibria of the system but compromise solutions that ignored the moment equilibrium condition as discussed in Section 4.3.2.1. If we define orientation errors as the difference between the desired angles ( $\alpha = \theta_{az}$ ,  $\beta = \theta_{za}$ ,  $\gamma = -\theta_{az}$ ) and the rotational angles  $\alpha$ ,  $\beta$ ,  $\gamma$  at the end of the simulation, then  $\beta$  shows significant errors of  $12^\circ$ ,  $14^\circ$  and  $14^\circ$  respectively for Cases 1, 2 and 3, while Cases 1 and 2 show no error in  $\alpha$  or  $\gamma$ . The zero error in  $\alpha$  and  $\gamma$  is due to the symmetry of the system (Figure

4.18) in these cases. The wind vector is directed from Tether #1 to Tether #4 while Tethers #2, #3 oppose Tethers #5, #6. As mentioned previously, the moment equations were ignored in the statics. In the dynamics, the resultant moments cause the payload platform to rotate and settle in true equilibria with steady-state errors in orientation and position. The tensions show some fluctuations before settling. Less clear from Figure 4.17 due to scaling, the steady-state tensions are very close to those obtained from the statics with the maximum difference being about 200 N. This is consistent with the small CP position errors shown in the figures.

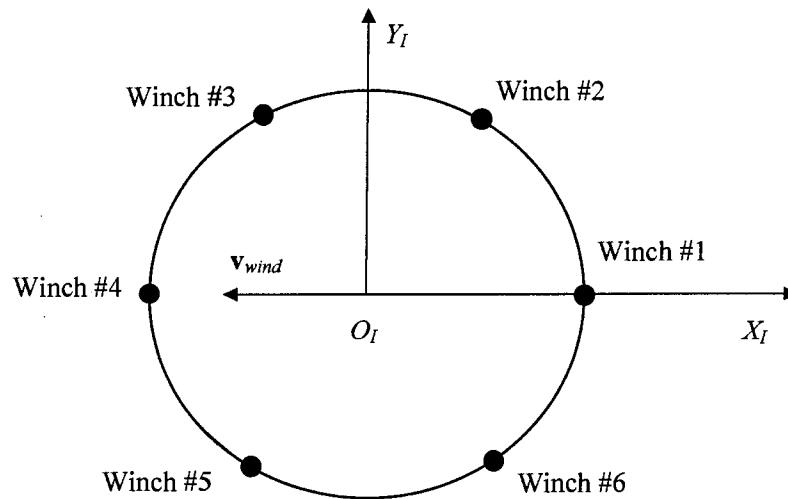


Figure 4.18 Top view of the six-Tether configuration

When turbulence is introduced, the simulation results (dash-dotted lines in Figures 4.15-4.17) show that in the first 5 seconds or so, the evolution of each variable is still dominated by the transition from the initial conditions to the true equilibria from the dynamics. Beyond that initial transition, the orientations in Case 1 show more

fluctuations than the other two cases, and in particular,  $\alpha$  and  $\gamma$  show fluctuations of about  $\pm 5^\circ$ . The position errors are substantially larger for the cases with turbulence in comparison to those without turbulence. Tether tensions exhibit fluctuations due to turbulence as well. The tensions in Tethers #3, #4 and #5 in Case 2, and those in Tethers #4, #5 and #6 in Case 3 show much less fluctuations than those in the other tethers. Those tethers are longer than the others, and also have the lowest tensions, which seems to make them more robust than others. Generally, it is important to note that the uncontrolled system is well behaved and all tethers remain taut.

As mentioned earlier, the system has a transient period of about 10-20 seconds. Therefore, when controllers are considered, we wait 20 seconds for the system to stabilize from its initial condition before introducing the controllers. In addition, the controller gains are ramped from zero to their full values in 100 seconds. This ramp time was determined after examining the system performance through simulations. It was found that bigger the gains or smaller the ramp time would cause slack tethers in the system. The winch controllers in all closed-loop cases have the same controller gains:  $k_d = 4$  s,  $k_p = 5$ ,  $k_i = 0$ . The gains are carefully chosen to make sure that all tethers are maintained at a tension of at least 1,000 N.

When winch controllers are introduced in the absence of the turbulence, we can see a reduction of errors of about  $3^\circ$  by the end of the simulation for  $\beta$  in Case 2 and all angles in Case 3 from the dashed lines in Figures 4.15-4.17. By contrast, the  $12^\circ$  error in  $\beta$  in Case 1 remains nearly unchanged. Overall the position errors of the payload platform are still small ( $< 0.2$  m). The controlled Cases 2 and 3 show small improvements in the position errors in the focal plane. Tether tension changes are smooth and moderate (less

than 20%).

When the controllers are used in the presence of turbulence, we can see from the results (solid lines in Figures 4.15-4.17) that the winch controllers have little effect on the orientation oscillations due to turbulence. However, the improvements in orientation error observed in the controlled cases without turbulence remain in these results. The oscillations due to turbulence in payload platform errors are significantly reduced. Fluctuations in tether tensions are reasonable since the tethers are actively controlled to regulate the effects of the turbulence in the system, but we can see that the controllers have introduced more high frequencies in these tensions

Overall, we can see that the controllers can exert some moderate control on the position error of the payload platform, but have only a small effect on the orientation of the payload platform.

If better control is required, a number of options exist: (1) a better controller design may improve control authority or, (2) a rearrangement of the tether attachment points at the payload and/or on the ground could improve matters. If these options are still ineffective, orientation control via the tethers may have to be abandoned.

## **Chapter 5   Incorporation of a Streamlined Aerostat**

An aerostat is used to provide lift for the entire tethered system in the LAR design. Of the two main types of aerostat available, streamlined and spherical, the spherical aerostat is a cheaper option. However, recent studies show that a tethered sphere has significant oscillations in a steady fluid flow [21], [22]. As a result, a streamlined aerostat may perform better than a spherical one. There are a number of possible advantages to a streamlined aerostat. A streamlined aerostat with the same lift as that of a spherical one will have much less drag due to its lower drag coefficient and lower frontal area. As well, a tethered streamlined aerostat may not introduce the oscillations typical of the spherical one [21], [22]. In this chapter, we will study the use of a streamlined aerostat and compare its performance to that of the spherical one.

### **5.1   Vehicle Introduction**

The streamlined aerostat used in this study is the TCOM 71M aerostat. TCOM has been a pioneer in tethered aerostat system for decades [35]. The TCOM 71M aerostat (Figure 5.1) is the largest aerostat in the TCOM aerostat family, with a length of 71 metres, a hull volume of about 16,000 cubic metres, and a fineness ratio of 3.3. The

TCOM 71M is typically used as a long endurance high altitude platform for long range radars, passive surveillance payloads and communications relay [35].

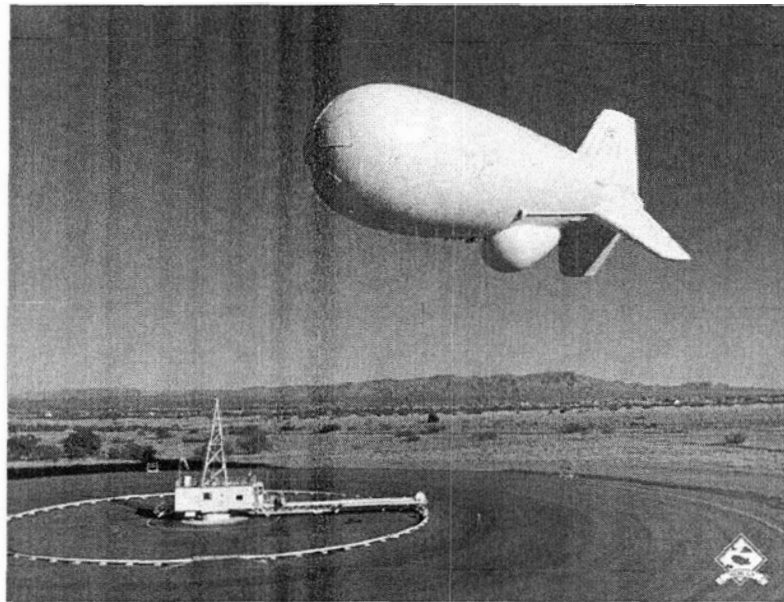


Figure 5.1 The TCOM 71M aerostat [35]

There is a great deal of information on this aerostat's characteristics in the open literature [16], [17], [18], [36], thus making it possible to validate our computer model to some degree.

The TCOM 71M structure includes the hull, the inverted-Y-shaped fins, and the bulge under the hull (Figure 5.1). Inside the hull, there is a helium compartment which makes up most of the volume and contains the helium gas which gives the aerostat its lifting capability. The three fins at the aft end of the aerostat provide aerodynamic stability and additional lift. The round bulge at the underside of the aerostat is typically



used to protect payload equipment from environmental exposure. Table 5.1 lists the characteristics of the 71M taken from reference [17] and [36].

Table 5.1 The TCOM 71M aerostat parameters [17], [36]

Volume	15,688	m <sup>3</sup>
Overall Length	71	m
Fineness ratio	3.3	
Helium lift	88,964	N
Gross structural weight	52,355	N
Mass (including gases)	17,688	kg
Fin half-span	17	m
Fin dihedral	45	deg
Single fin area	180	m <sup>2</sup>

In our model, the buoyancy of the aerostat is defined as difference between the weight of the air displaced by the helium gas and helium gas weight. The weight is defined as being the aerostat gross structural weight; while the mass used in the motion equations is the mass including the structure and all gases. By crosschecking with [37], we believe the mass provided by [17] and [36] (i.e. 17688 kg) includes the gases and also the payload mass. However, that payload will not be installed in our application, and so we subtract the mass of the payload from the mass listed in Table 5.1 for our purposes.

The helium lift given by [17] and [36] is used to obtain the helium volume in the aerostat and we then use this volume to calculate the aerostat buoyancy.

The TCOM 71M provides about the same amount of lift as the spherical aerostat discussed in previous chapters. The net lift (defined as the helium lift minus the gross structural weight) of the TCOM 71M is 35806 N, while the spherical aerostat discussed in previous chapters had 34895 N of net lift at 600 m altitude.

## 5.2 Modelling the TCOM 71M Aerostat

Before incorporating the aerostat model into our system, we first model it alone and validate the model against published data.

Since the TCOM 71M is a streamlined aerostat, a component breakdown method, proposed by Nahon [38] for streamlined underwater vehicles, can be used to model it. In this method, the aerodynamic characteristics of each component (the hull, fins, etc) are represented by a resultant aerodynamic force applied at its center of pressure. The force and center of pressure of each component are determined by well-known relations based on its geometry. The summation of all component effects determines the total forces and moments acting on the vehicle. Some techniques developed especially for aerostats and airships in [13], such as the hull-fin effect and the choice of the fin's center of pressure, can also be used when modelling the aerostat.

Figure 5.2 shows the structure of the aerostat [36]. In the aerodynamic model, the aerostat is broken down into components including the hull, the three aft fins, and the bulge. We now discuss the modelling of the TCOM 71M aerostat in more detail.

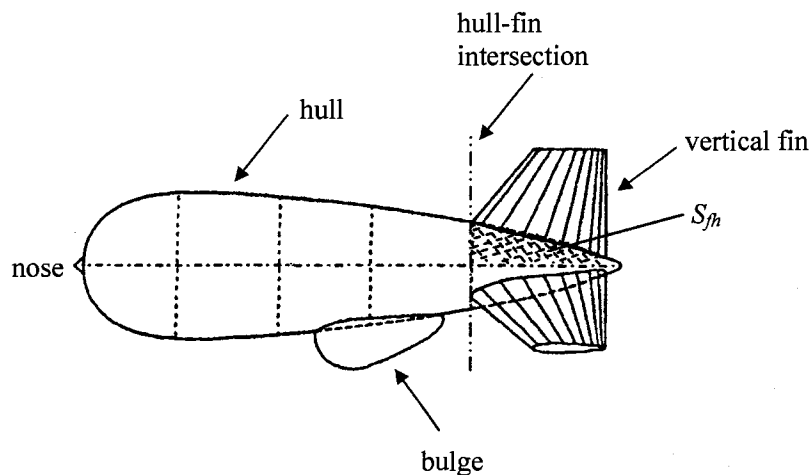


Figure 5.2 The structure of the TCOM 71M aerostat

### 5.2.1 Reference Frames

Two body-fixed reference frames are used to when describing the modelling process in the following sections (Figure 5.3).

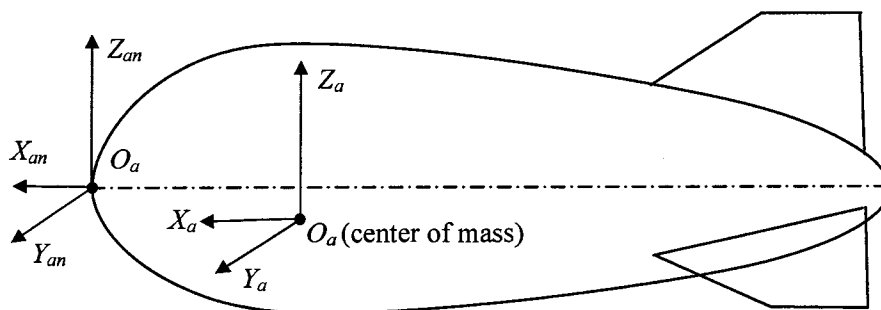


Figure 5.3 Reference frames of the aerostat

The body-fixed frame  $O_a X_a Y_a Z_a$  in Figure 5.3, as discussed in Chapter 2 and also shown in Figure 2.2, is used to sum all the forces acting on the TCOM 71M aerostat. The

origin of frame  $O_a X_a Y_a Z_a$  is fixed at the mass center of the aerostat, with  $O_a X_a$  pointing forward,  $O_a Z_a$  pointing upwards and  $O_a Y_a$  pointing left to complete this right-handed reference frame (Figure 5.3).

Frame  $O_{an} X_{an} Y_{an} Z_{an}$ , shown in Figure 5.3, is used in later sections to describe the location of the center of mass of the aerostat and the center of buoyancy. This frame is parallel to the body-fixed frame  $O_a X_a Y_a Z_a$  with its origin at the nose of the aerostat.

### 5.2.2 Scaled Parameters

Most of the information about the TCOM 71M aerostat was available from open sources [17], [36]. However, some parameters such as the location of the center of mass and the magnitude of the moments of inertia of the aerostat were not available from these papers. We therefore estimated these properties by scaling those of a similarly-shaped balloon shown in Figure 5.4 [39]. This tethered balloon is smaller but looks very similar to the TCOM 71M except that it has four aft fins while the TCOM 71M has three. Its main properties are listed in Table 5.2.

Table 5.2 Balloon properties [39]

Hull volume	5,663 m <sup>3</sup>
Maximum hull length	49.5 m
Maximum hull diameter	16.1 m
Total mass	5,641 kg

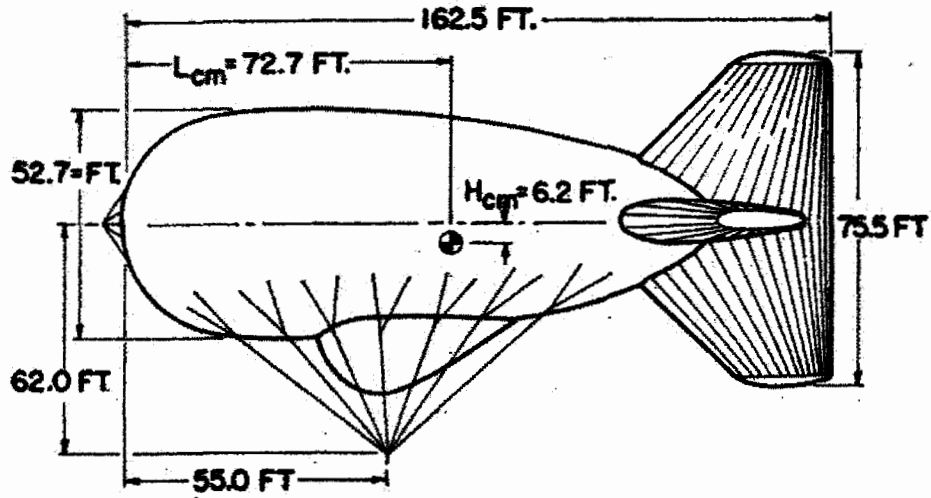


Figure 5.4 Tethered balloon layout [39]

The scaled parameters are the center of mass, the moments of inertia and the leash attachment location in the model. The scaling procedure is elaborated as follows.

#### 5.2.2.1 Moments and Products of Inertia

From the TCOM 71M aerostat figures [30] [36], it can be assumed that the aerostat has a longitudinal plane of symmetry, the  $X_a Z_a$ -plane. Therefore, we have the products of inertia  $I_{xy} = I_{yz} = 0$ . The moments and product of inertia that remain to be determined are  $I_{xx}$ ,  $I_{yy}$ ,  $I_{zz}$  and  $I_{xz}$ .

We first need to find the scale factor by which the balloon's moments of inertia should be scaled. The parameters pertaining to the moments of the two vehicles are listed in Table 5.3.

Table 5.3 Ratios between the two vehicles

	TCOM 71M	Balloon [39]	Ratio	Notes
Hull Volume (m <sup>3</sup> )	15,688	5,663	1.40	Size ratio = (volume ratio) <sup>1/3</sup>
Length (m)	71	49.5	1.43	Size ratio
Maximum Diameter (m)	21.5	16.1	1.34	Size ratio
Mass (kg)	15,200	5,641	2.69	Mass ratio

The middle value 1.40 is used for the size ratio. The mass ratio is 2.69. The moments of inertia are proportional to mass and distance squared. A scale factor for the moments and product of inertia is therefore determined by combining the mass ratio and size ratio as  $2.69 \cdot 1.40^2 = 5.3$ .

The moments and product of inertia of the TCOM 71M aerostat are thus obtained as shown in Table 5.4.

Table 5.4 Moments and product of inertia

	Balloon [39]	Scale factor	TCOM 71M
$I_{xx}$ (kg·m <sup>2</sup> )	120,749.1	5.3	639,970
$I_{yy}$ (kg·m <sup>2</sup> )	648,094.4		3,434,900
$I_{zz}$ (kg·m <sup>2</sup> )	572,900.8		3,036,374
$I_{xz}$ (kg·m <sup>2</sup> )	77,024.0		408,227

### 5.2.2.2 The Center of Mass

Reference [39] gives the mass center of the balloon in the  $O_{an}X_{an}Y_{an}Z_{an}$  coordinate system, as -22.14 m in the  $X_{an}$ -direction, and -1.88 m in the  $Z_{an}$ -direction.

If the size ratio 1.40 is used, the mass center of the TCOM 71M aerostat would be located at

$$X_{an}\text{-direction} \quad -22.14 \text{ m} * 1.40 = -31.00 \text{ m}$$

$$Z_{an}\text{-direction} \quad -1.88 \text{ m} * 1.40 = -2.63 \text{ m}$$

An alternative is to use the length ratio to obtain the mass center location in the  $X_{an}$ -direction, and maximum diameter ratio to obtain its location in the  $Z_{an}$ -direction.

Using this method, the center of mass would be located at

$$X_{an}\text{-direction} \quad -22.14 \text{ m} * 1.43 = -31.66 \text{ m}$$

$$Z_{an}\text{-direction} \quad -1.88 \text{ m} * 1.34 = -2.52 \text{ m}$$

Taking a median value, the location of center of mass in the  $O_{an}X_{an}Y_{an}Z_{an}$  frame for the aerostat is chosen to be -31.3 m in the  $X_{an}$ -direction, and -2.6 m in the  $Z_{an}$ -direction.

### 5.2.2.3 The Leash Attachment Point

It is assumed that the leash attaches to the aerostat at a point with coordinates ( ${}^a x_l$ , 0,  ${}^a z_l$ ) in the body-fixed frame  $O_a X_a Y_a Z_a$ . This leash attachment point in our model is deemed as a point on a rigid body extension of the TCOM 71M aerostat. As a result, its motion can be found, using kinematic relations from the motion of the aerostat.

The tethered balloon has its attachment point position available in Frame

$O_{an}X_{an}Y_{an}Z_{an}$  as (-16.76 m, 0, -18.90 m) [39]. As we did for the determination of the location of the mass center, we scale the attachment point location by the size ratio of 1.40,

$$X_{an}\text{-direction} \quad -16.76 \text{ m} * 1.40 = -23.46 \text{ m}$$

$$Z_{an}\text{-direction} \quad -18.90 \text{ m} * 1.40 = -26.46 \text{ m}$$

And also use the length ratio of 1.43 for the  $X_{an}$ -direction and the diameter ratio of 1.34 for the  $Z_{an}$ -direction to find,

$$X_{an}\text{-direction} \quad -16.76 \text{ m} * 1.43 = -23.97 \text{ m}$$

$$Z_{an}\text{-direction} \quad -18.90 \text{ m} * 1.34 = -25.33 \text{ m}$$

Taking the median values, the leash attachment point is chosen to be at (-23.7m, 0, -25.9 m) in Frame  $O_{an}X_{an}Y_{an}Z_{an}$ . Therefore, the location in the body-fixed frame  $O_aX_aY_aZ_a$  would be (7.6 m, 0, -23.3 m).

### 5.2.3 Estimated Center of Buoyancy

The location of the center of buoyancy of the TCOM 71M is not available in the open literature, and that of the balloon is not specified in [39]. Therefore, the location of the center of buoyancy has to be estimated using other means. It is assumed that the center of buoyancy is located on the longitudinal symmetric  $X_{an}$ -axis. The exact location on the  $X_{an}$ -axis is chosen in order to have the aerostat settle at a small nose-up pitch angle under different wind conditions. Simulations with different center of buoyancy locations on the  $X_{an}$ -axis were carried out with these considerations in mind. This resulted in a choice of the location of the center of buoyancy at (4.5 m, 0, 2.6 m) in the body-fixed frame  $O_aX_aY_aZ_a$  for the center of buoyancy of the aerostat.



## 5.2.4 Aerostat Component Breakdown

The aerostat is modelled by a component breakdown method introduced by Nahon [38]. It consists of the hull, three aft fins, and a bulge. The aerodynamics characteristics of these components are represented by forces acting at their center of pressure.

### 5.2.4.1 The Hull

The hull of the aerostat is a body of revolution. There are a few methods for modelling the aerodynamics for bodies of revolution. One of the first attempts to use potential flow theory to estimate the lift and moment for bodies of revolution was made by Munk [15]. Several methods were developed thereafter [14] [40] [41], which also accounted for the effects of viscosity.

Jones and DeLaurier presented an analytical model for finned axisymmetric bodies which showed good agreements with wind tunnel data on five aerostats and airships [9]. That model is used to model the hull in this work. The aerodynamics equations given by Jones and DeLaurier include the effects of the hull and fins, but we only use their formulation for the hull effects.

Due to the hull-fin interaction, the aerodynamic forces acting on the hull are calculated based on the geometry of the main part of the hull only, i.e., the part of the hull from the nose to the hull-fin intersection point (Figure 5.2). The section behind the fin leading edge is considered as part of the fin's aerodynamic forces. Therefore, we use the following equations for the hull forces (see Figure 5.5 for reference):

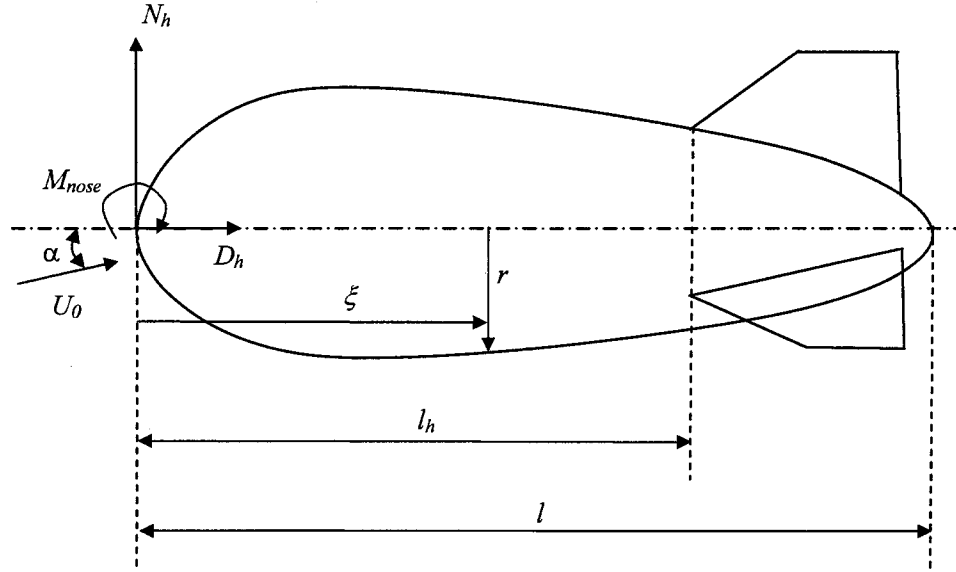


Figure 5.5 Modelling the hull

normal force,  $N_h$ ,

$$N_h = q_0 \{ (k_3 - k_1) \eta_k I_1 \sin(2\alpha) \cos(\alpha/2) + (Cd_c)_h J_1 \sin \alpha \sin|\alpha| \} \quad (5.1)$$

axial force,  $D_h$ ,

$$D_h = q_0 \{ (Cd_c)_0 S_h \cos^2 \alpha - (k_3 - k_1) \eta_k I_1 \sin(2\alpha) \sin(\alpha/2) \} \quad (5.2)$$

moment about the nose (positive nose up),  $M_{nose}$ ,

$$M_{nose} = -q_0 \{ (k_3 - k_1) \eta_k I_3 \sin(2\alpha) \cos(\alpha/2) + (Cd_c)_h J_2 \sin \alpha \sin|\alpha| \} \quad (5.3)$$

where

$q_0$  = steady state dynamic pressure =  $\rho U_0^2 / 2$ , where  $U_0$  is the flow speed

$\alpha$  = angle of attack of the hull

$k_l, k_3$  = axial and lateral apparent-mass coefficients respectively,  $k_3 - k_l = 0.71$

as  $k_3$  is 0.82,  $k_l$  is 0.11 for this aerostat which has a fineness ratio of

3.3 [15]

$S_h$  = hull reference area, the frontal area,  $\pi d_{max}^2/4 = 363 \text{ m}^2$

$\eta_k$  = hull efficiency factor accounting for the effect of the fins on the hull,

1.12 [13]

$(Cd_c)_h$  = hull cross-flow drag coefficient, referenced to  $J_l$ , 0.23 [13], [40], [41]

$(Cd_h)_0$  = hull zero-angle axial drag coefficient, referenced to  $S_h$ , 0.035 [42]

Also,

$$\begin{aligned} I_1 &= \int_0^{l_h} \frac{dA}{d\xi} d\xi, & I_3 &= \int_0^{l_h} \xi \frac{dA}{d\xi} d\xi \\ J_1 &= \int_0^{l_h} 2r d\xi, & J_2 &= \int_0^{l_h} 2r \xi d\xi \end{aligned}$$

where  $l_h$  is the hull length,  $A$  is the cross-sectional area,  $r$  is the hull radius,  $\xi$  is the axial distance along the hull from the nose (Figure 5.5). The values are estimated based on the geometry of the aerostat shown in Figure 5.2, and come to

$$\begin{aligned} I_1 &= 129 \text{ m}^2, & I_3 &= -6700 \text{ m}^3 \\ J_1 &= 912 \text{ m}^2, & J_2 &= 22804 \text{ m}^3 \end{aligned}$$

In order to conveniently use Nahon's component breakdown method, we would like to transform the aerodynamic characteristics of the hull to forces at its center of pressure.

As a slender body of revolution, we assume the center of pressure is on the longitudinal  $X_{an}$ -axis as defined in Figure 5.3. We have Equations (5.1), (5.2) and (5.3) representing the aerodynamics characteristics and we know that

$$M_{nose} = N_h x_{cp}$$

where  $x_{cp}$  is the location of the center of pressure. Therefore,

$$x_{cp} = M_{nose} / N_h$$

The solid line in Figure 5.6 is the plot of  $x_{cp}/l$  as a function of the angle of attack  $\alpha$  in degrees, where  $l$  is the hull length as shown in Figure 5.5. We derive a linearized relation between  $x_{cp}$  and  $\alpha$  from the solid line in Figure 5.6:

$$x_{cp}/l = 0.76 - 0.94|\alpha| \quad (5.4)$$

where  $\alpha$  is the angle of attack in radians. This relation is plotted in Figure 5.6 as the solid line.

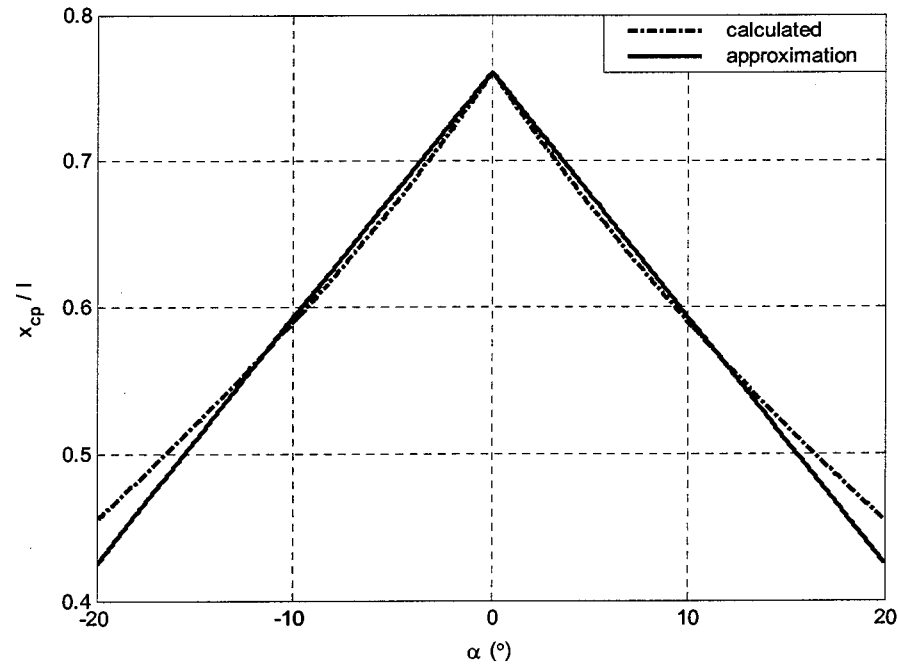


Figure 5.6 Center of pressure of the hull

The actual relation implemented in the simulation is

$$^a x_{cp} = 34 + (0.76 - 0.94|\alpha|)l \quad (5.5)$$

where  $x_{cp}$  along the  $X_{an}$ -axis is transformed to  ${}^a x_{cp}$  in the body-fixed frame  $O_a X_a Y_a Z_a$  of the aerostat. Therefore, we have the center of pressure of hull located at  $({}^a x_{cp}, 0, 5.8 \text{ m})$ .

#### 5.2.4.2 The Fins

The three fins are all the same size with an inverted ‘Y’ configuration. Each of the two lower fins has an anhedral angle of 45 degrees. In the model, the planform area of one fin includes the fin’s actual planform area and the planform area of the rear part of the hull, denoted as  $S_{fh}$  in Figure 5.2. However, referring to [13], the position of the center of pressure is that of the fin without considering the hull area  $S_{fh}$  that is, on the quarter-chord line, half-way between the fin’s root and tip (Figure 5.7).

The lift and drag of each fin are calculated using equations [42], [43]:

$$\begin{aligned} L &= q_0 S C_L \\ D &= q_0 S C_D \end{aligned} \quad (5.6)$$

where

$$\begin{aligned} C_L &= C_{l\alpha} \frac{A}{A + 2(A + 4)/(A + 2)} \alpha = C_{L\alpha} \alpha \\ C_D &= C_{D0} + \frac{C_L^2}{\pi A e} \end{aligned} \quad (5.7)$$

and

$A$  = aspect ratio of the fin, the square of the fin span divided by the fin reference area, 2.4

$S$  = the fin reference area, which is the planform area of each fin including  $S_{fh}$  (Figure 5.2), 243 m<sup>2</sup>

$C_{l\alpha}$  = the slope of the 2-D section lift curve,  $2\pi$  [42], [43]

$C_{D0}$  = the parasite drag coefficient, 0.012 for this study

$e$  = Oswald efficiency factor, 0.86 in this study [42]

Substituting all the parameters in to Equation (5.7), we have  $C_{L\alpha} = 2.8$ . Since the fins operate in a region where the flow is disturbed by the hull, the 3-D lift coefficient of the fins is further reduced to about 70% of its calculated value,  $C_{L\alpha} = 2.0$  [44].

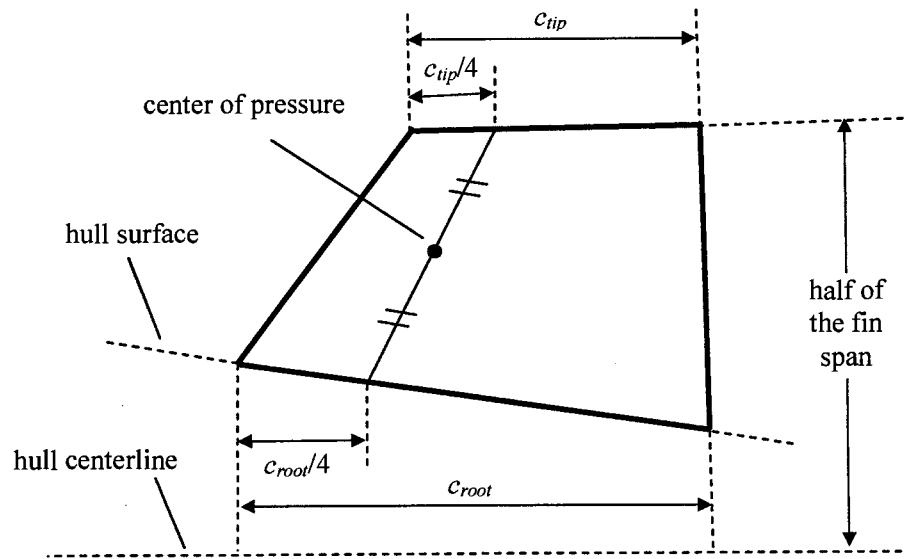


Figure 5.7 Center of pressure of the fin

#### 5.2.4.3 The Bulge

The bulge is rounded and small. It is modelled as a low aspect ratio plane for simplicity. Thus the Equations (5.6) for calculating lift and drag of a plane are applied to the bulge. As well, the center of pressure is chosen to be the quarter-chord line, half-way

between the bulge's root and tip. The bulge parameters are listed in Table 5.5 along with those of the fins:

Table 5.5 Parameters of the fins and the bulge

Parameters	Fin	Bulge
Reference area $S$ (m <sup>2</sup> )	243	67
Aspect Ratio $A$	2.4	1
Parasite drag coefficient $C_{D0}$	0.012	0.012
Oswald efficiency factor $e$	0.86	0.86
Calculated 3-D lift coefficient $C_{L\alpha}$	2.8	1.5
Actual 3-D lift coefficient $C_{L\alpha}$	2.0	1.0

### 5.2.5 Added Mass and Moments

When an object moves in a fluid, there exist forces and moments, which are proportional to the acceleration of the body and the amount of displaced fluid. They are usually expressed as added mass and moments of inertia in the motion equations [34]. For a 6-DOF body, the added mass and moments of inertia can be described by an added mass and moment of inertia tensor:

$$[m_{ij}]: i, j = 1, 2, 3, 4, 5, 6$$

where  $m_{ij}$  relates the force on the body in the  $i$ -direction to the acceleration in the  $j$ -direction. The indices 1, 2, 3 correspond to the  $X_a$ -,  $Y_a$ - and  $Z_a$ -axis translational

acceleration directions in the aerostat body-fixed frame; and indices 4, 5, 6 correspond to the rotational acceleration directions about the  $X_a$ -,  $Y_a$ - and  $Z_a$ -axis as illustrated in Figure 2.2.

For the TCOM 71M aerostat model, an approximation of the added mass and moments of inertia is made based on the hull shape with consideration of the fins. The hull of the aerostat is regarded as an ellipsoid of revolution with a fineness ratio of 3.3, the fins are equivalent to plates. Using the coefficients and formula provided in [34], and ignoring the coupling between the principal modes of motion, we then have

$$m_{ii} = k_{i|h} \rho V_h + k_{i|f} \rho V_f, \quad i = 1, \dots, 6 \quad (5.8)$$

where  $V_h$  is the hull volume,  $V_f$  is the equivalent volume of the fins normal to the motion axis  $i$ . The coefficient  $k_{i|h}$  is the added mass coefficient along motion axis  $i$  for the hull which can be found in [34] based on the fineness ratio of the hull, and  $k_{i|f}$  is the added mass coefficient along motion axis  $i$  for the fins which is approximated using a strip theory synthesis discussed in [34]. Therefore, we have the added mass tensor as:

$$\mathbf{M}_a = \begin{bmatrix} \mathbf{m}_a & \mathbf{0} \\ \mathbf{0} & \mathbf{I}_{acm} \end{bmatrix}$$

where

$$\begin{aligned} \mathbf{m}_a &= \begin{bmatrix} m_{11} & 0 & 0 \\ 0 & m_{22} & 0 \\ 0 & 0 & m_{33} \end{bmatrix} = \begin{bmatrix} 1797 & 0 & 0 \\ 0 & 14268 & 0 \\ 0 & 0 & 14142 \end{bmatrix} kg \\ \mathbf{I}_{acm} &= \begin{bmatrix} m_{44} & 0 & 0 \\ 0 & m_{55} & 0 \\ 0 & 0 & m_{66} \end{bmatrix} = \begin{bmatrix} 151650 & 0 & 0 \\ 0 & 2691900 & 0 \\ 0 & 0 & 2781600 \end{bmatrix} kg \cdot m^2 \end{aligned}$$

This added mass tensor is added to the inertia tensor of the aerostat when setting up the motion equations.



### 5.3 Model Validation

The normal force coefficient and pitch moment coefficient for the entire aerostat can now be validated by comparing them with those shown in [36].

Figure 5.8 shows the results of our model.  $C_n$  in Figure 5.8 is the normal force coefficient as a function of the angle of attack;  $C_m$  is the pitching moment coefficient about the nose as a function of the angle of attack. They are nondimensionalized using the following relations:

$$C_n = N / (q_0 S)$$

$$C_m = M / (q_0 S l)$$

where

$N$  = the total normal force, includes the normal force of the hull and those of the port and starboard fins, positive downward as in [36]

$M$  = the total pitching moment, includes the effects from the hull, the 3 fins and the bulge, positive nose up

$q_0$  = dynamic pressure

$S = (\text{hull volume})^{2/3}$

$l$  = hull length

Figure 5.9 shows the graphs of the same coefficients from [36], the circles are data points from wind tunnel tests, the lines are from their dynamic model.  $\hat{Z}_0$  in Figure 5.9(a) is the vertical force coefficient,  $C_n$ , in our notation;  $\hat{M}_0$  in Figure 5.9(b) is the pitching moment coefficient,  $C_m$ , in our notation. The coefficients shown in Figure 5.8 for our model match those from [36] very well.

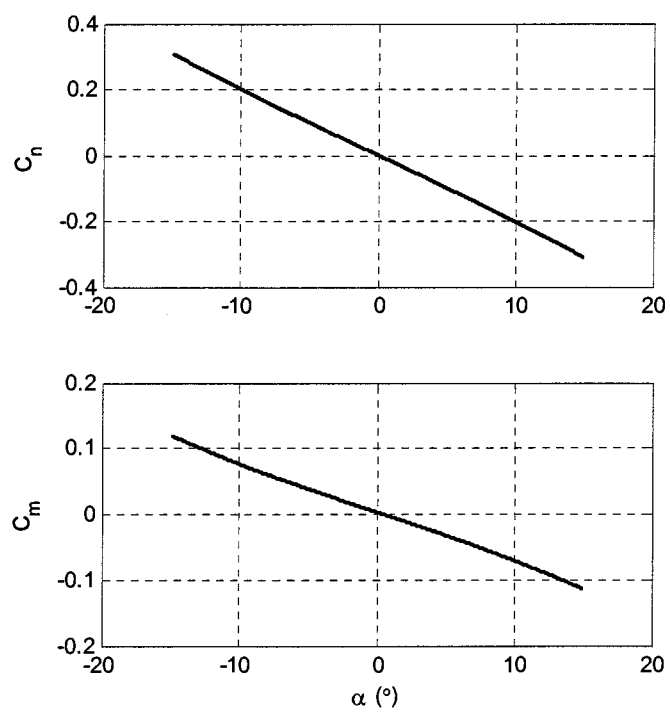
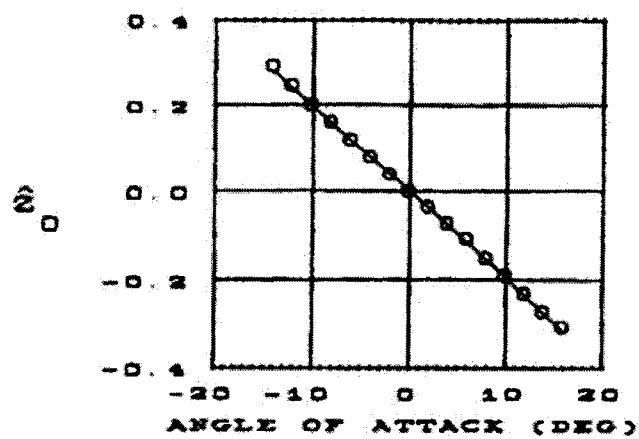
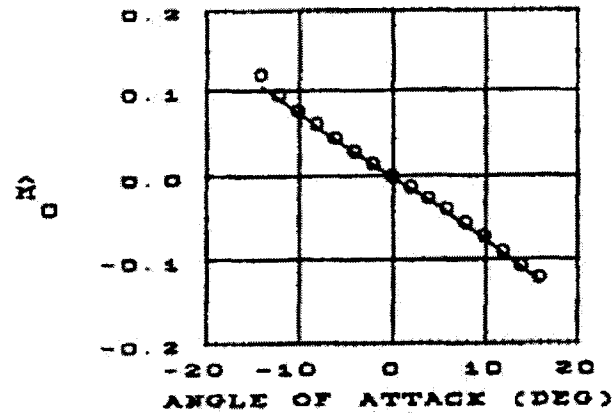


Figure 5.8 Normal force coefficient and pitching moment coefficient about the nose of the TCOM 71M



(a) Normal force coefficient



(b) Pitching moment coefficient about the nose

Figure 5.9 Aerodynamic model of [36] compared with wind tunnel data [36]

## 5.4 Implementation and Incorporation

The TCOM 71M aerostat model was incorporated into the existing multi-tethered aerostat system to replace the spherical aerostat for our study. In the original work [24], the spherical aerostat was modelled as a point mass attached to the top of the leash (Figure 4.2). That was appropriate for the spherical aerostat because it is spherically symmetric and has straightforward aerodynamics. In the case of the streamlined aerostat, we must model it as a rigid body with translational and rotational DOFs. To make the code more generic, the rotational DOFs are also applied to the spherical aerostat in the dynamics. It is implemented in such a way that switching between the spherical or streamlined aerostat is easily achieved by turning on or off a predefined variable in the code.

The incorporation was done in both the statics and dynamics components of the simulation.

### 5.4.1 Statics

The statics solution described in Chapter 3 relates to a spherical aerostat. In the case of a spherical aerostat, the drag and lift do not vary with its orientation due to its spherical symmetry, and this was the reason why its orientation was not considered. For a streamlined aerostat, the aerodynamic forces change with orientation. This implies that we have extra unknowns in the statics problem, and we must solve for the orientation of the aerostat.

In an equilibrium condition we know that the aerostat will be facing into the wind with zero roll angle and possibly a small nonzero pitch angle. Thus, we only need to solve for the pitch angle in the statics solution. We used an approximate solution to avoid making too many changes in the statics. We used the dynamics simulation to find the steady state pitch angle for different wind speeds and zenith angles. The zenith angle affects the wind applied to the aerostat because we use a boundary layer wind profile (Figure 3.9), and it also affects the air density at the aerostat height. These factors have a small effect on the resulting pitch angle of the aerostat. The magnitude of the wind speed used has a more significant effect. Table 5.6 shows the resulting pitch angles under a range of conditions.

It is noted that at zenith angles 0 and 30°, the steady state pitch angles are very close to each other for a given wind speed. In the case of a zenith angle of 0, the aerostat altitude is about 623 m; in the case of a zenith angle of 30°, the aerostat altitude is about

556 m. These altitudes are above the boundary layer of the wind model which is 500 m (Figure 3.9), which means the aerostat would experience the same wind speed in these two cases. This then implies that the air density effect is very small. In the case of 60° zenith angle, the aerostat altitude is about 373 m, and the actual wind speed for the aerostat is

$$U = U_g \left( \frac{h}{h_g} \right)^{0.19} = 0.946 U_g \quad (5.9)$$

Table 5.6 Aerostat pitch angles under different conditions

Wind speed $U_g$ (m/s)	Zenith angle(°)	Pitch angle(°)	Average pitch angle (°)
10	0	-7.70	-7.70
	30	-7.70	
	60	-7.63	
8	0	-7.40	-7.40
	30	-7.40	
	60	-7.35	
6	0	-7.13	-7.13
	30	-7.13	
	60	-7.10	
4	0	-6.91	-6.91
	30	-6.91	
	60	-6.90	

Due to the minimal effect of the zenith angle, we chose to only consider the variation of pitch angle with wind speed. At each wind speed, we use the average pitch angle for the 0 and 30° zenith angle cases. An approximate relationship is calculated based on the wind speeds and average pitch angles from Table 5.6:

$$\theta_{ss} = -6.716 - 0.0005833U - 0.01375U^2 + 0.0003958U^3 \quad (5.10)$$

where  $\theta_{ss}$  is the steady state pitch angle in degrees.

The pitch angles obtained using Equations (5.9) and (5.10) are checked against their exact values in Table 5.6, and the maximum difference is 0.01°, which is very small.

### 5.4.2 Dynamics

In the dynamics, the forces and moments of all components, calculated using the methods discussed in Section 5.3, are summed up at the center of mass. The aerostat motion is governed by [38]

$$\begin{aligned} \mathbf{F}_{cm} &= (\mathbf{m} + \mathbf{m}_a) \dot{\mathbf{v}}_{cm} \\ \mathbf{M}_{cm} &= (\mathbf{I}_{cm} + \mathbf{I}_{acm}) \dot{\boldsymbol{\omega}} + \boldsymbol{\omega} \times \mathbf{I}_{cm} \boldsymbol{\omega} \end{aligned} \quad (5.11)$$

where

$\mathbf{F}_{cm}$  = the sum of external forces applied to the aerostat, including aerodynamic forces, buoyancy, weight, and tether tension (Figure 5.10)

$\mathbf{m}$  = aerostat mass matrix,  $m\mathbf{I}$

$\mathbf{m}_a$  = the added mass matrix as described in section 5.2.4

$\mathbf{v}_{cm}$  = the velocity of its mass center with respect to the inertial frame  $O_I X_I Y_I Z_I$

$\mathbf{M}_{cm}$  = the sum of external moments applied to the aerostat about its center of mass, including moments due to aerodynamic forces, buoyancy, and tether tension

$\mathbf{I}_{cm}$  = the inertia tensor of the aerostat about its center of mass

$\mathbf{I}_{acm}$  = the added moments of inertia matrix as described in section 5.2.4

$\boldsymbol{\omega}$  = the aerostat's angular velocity vector

The sum of external forces  $\mathbf{F}_{cm}$  (Figure 5.10) and the sum of external moments  $\mathbf{M}_{cm}$  can be expressed as

$$\begin{aligned}\mathbf{F}_{cm} &= \mathbf{B} + \mathbf{W} + \mathbf{F}_h + \mathbf{F}_{lb} + \mathbf{F}_{pf} + \mathbf{F}_{sf} + \mathbf{F}_{uf} + \mathbf{T} \\ \mathbf{M}_{cm} &= \mathbf{M}_B + \mathbf{M}_h + \mathbf{M}_{lb} + \mathbf{M}_{pf} + \mathbf{M}_{sf} + \mathbf{M}_{uf} + \mathbf{M}_t\end{aligned}\quad (5.12)$$

where

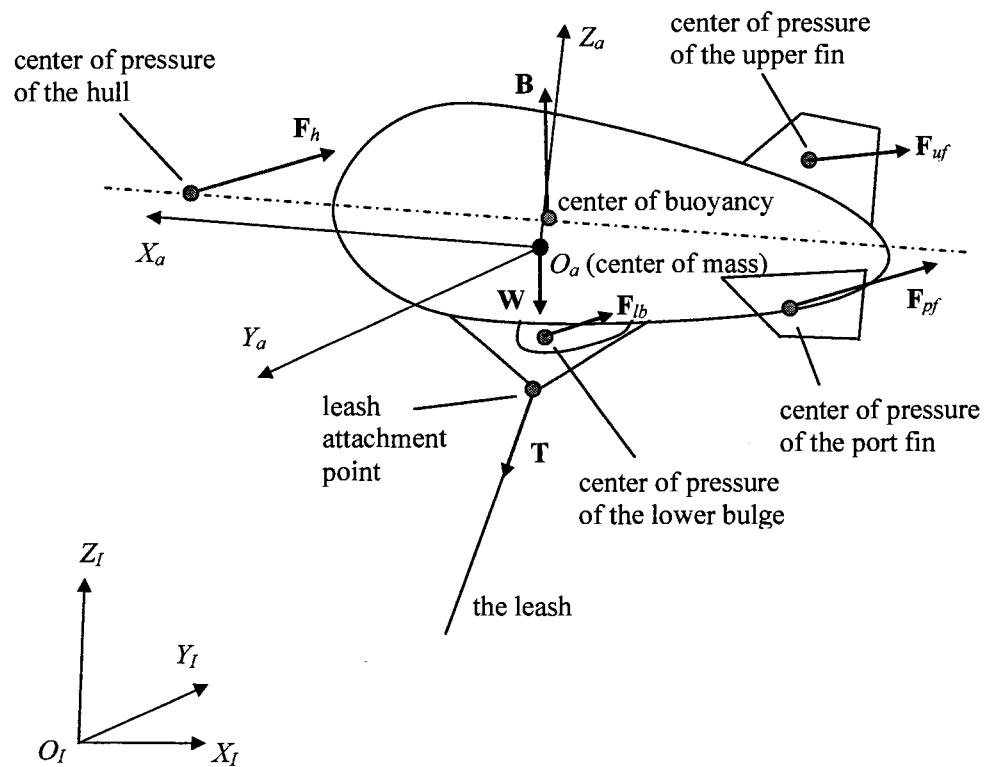


Figure 5.10 External forces applied to the aerostat

$\mathbf{B}, \mathbf{M}_B$  = buoyancy of the aerostat and resulting moment

$\mathbf{W}$  = weight of the aerostat

$\mathbf{F}_h, \mathbf{M}_h$  = aerodynamic force and moment of the hull

$\mathbf{F}_{lb}, \mathbf{M}_{lb}$  = aerodynamic force and moment of the lower bulge

$\mathbf{F}_{pf}, \mathbf{M}_{pf}$  = aerodynamic force and moment of the port fin

$\mathbf{F}_{sf}, \mathbf{M}_{sf}$  = aerodynamic force and moment of the starboard fin

$\mathbf{F}_{uf}, \mathbf{M}_{uf}$  = aerodynamic force and moment of the upper fin

$\mathbf{T}, \mathbf{M}_t$  = tension from the leash and its resulting moment

Figure 5.10 depicts external forces applied to the aerostat except for  $\mathbf{F}_{sf}$ .

## 5.5 Results & Discussions

The simulations for this streamlined aerostat were all performed with the same system parameters as for the spherical aerostat discussed in chapter 3. A turbulence model presented in [24] was superimposed on the wind profile for all the simulations.

Figures 5.11 - 5.14 present the simulation results with and without a controller, a zenith angle of zero and an azimuth angle of zero ( $\theta_{za} = \theta_{az} = 0$ ). Figures 5.15 - 5.18 present the simulation results with and without a controller for a zenith angle of  $60^\circ$  and an azimuth angle of zero ( $\theta_{za} = 60^\circ, \theta_{az} = 0$ ). The wind condition used in all cases is the same: a mean wind speed of 10 m/s and a wind angle of  $180^\circ$ . The winch controllers in all cases use the same gains of  $k_d = 6$  s,  $k_p = 30$  and  $k_i = 3$  s<sup>-1</sup> using the strategy previously discussed in Section 4.1. Position errors and tensions for the spherical aerostat case are also shown in Figures 5.13, 5.14 and 5.17, 5.18 for easy comparison.



From the results (Figures 5.11 - 5.18), we can see that the uncontrolled cases do not show much response to high-frequency turbulent wind gusts. This is consistent with the spherical aerostat studied in [24]. This large scale tethered system acts as a low-pass filter and rejects the high-frequency disturbances applied to the system. It is also apparent that, without control, the streamlined aerostat leads to much larger confluence point error than does the spherical aerostat.

Table 5.7 lists the payload position errors in the cases considered (see also Figures 5.13 and 5.17). The payload position errors exhibit more oscillation at a zenith angle of  $60^\circ$  (Figure 5.17) than at a zenith angle of zero (Figure 5.13). This is consistent with the results obtained with the spherical aerostat. In separate tests not shown here, it was also obvious that the wind speed has a large effect on the system behaviour. The higher the wind speed, the worse the system control precision.

Table 5.7 Payload position errors

Conditions		Maximum position error for <i>uncontrolled</i> system		Maximum position error for <i>controlled</i> system	
Payload position	Wind condition	<i>in</i> the focal plane (m)	<i>out</i> of the focal plane (m)	<i>in</i> the focal plane (m)	<i>out</i> of the focal plane (m)
$\theta_{za} = 0$ $\theta_{az} = 0$	$U_g = 10$ m/s	0.55	3.0	0.012	0.41
$\theta_{za} = 60^\circ$ $\theta_{az} = 0$	$\theta_w = 180^\circ$	3.4	2.6	0.38	0.28

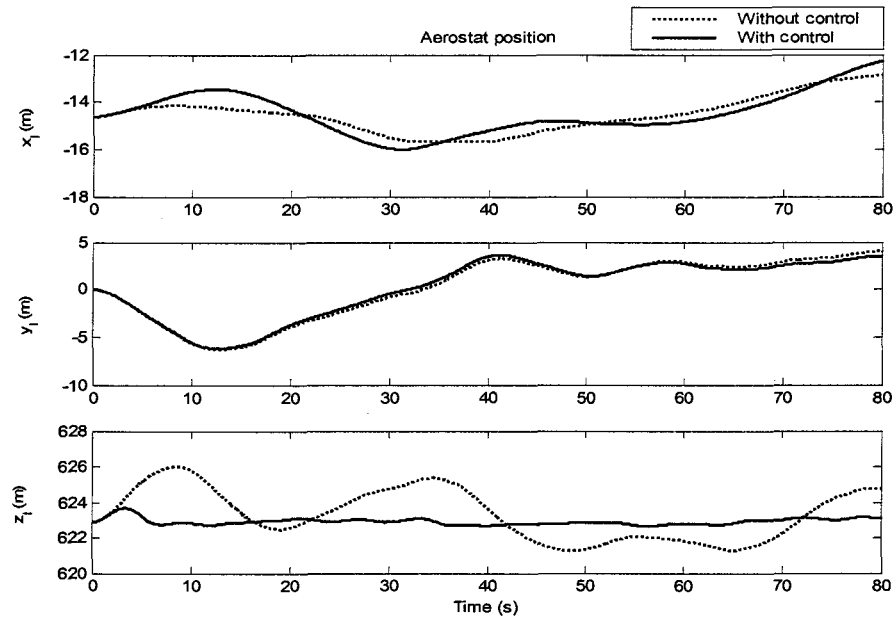


Figure 5.11 Aerostat translational motion for  $\theta_{za} = \theta_{az} = 0$

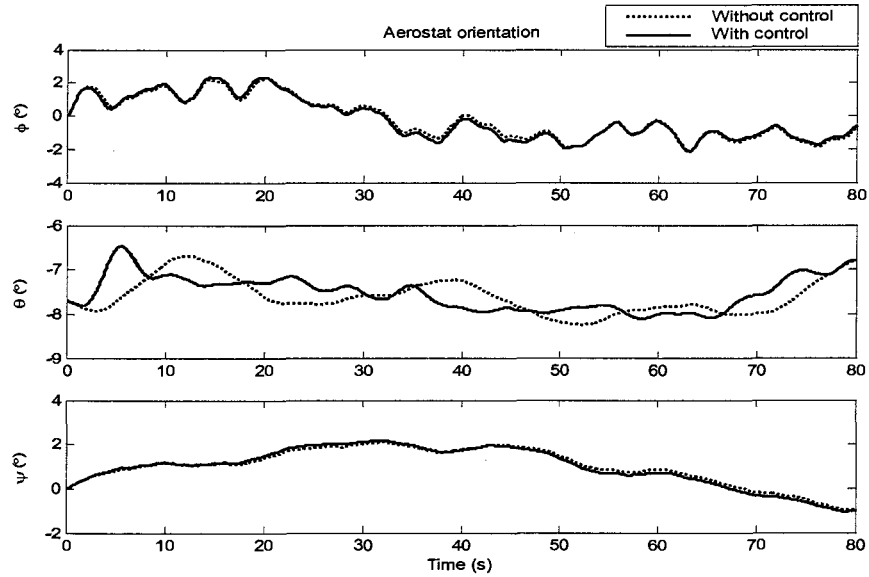


Figure 5.12 Aerostat rotational motion for  $\theta_{za} = \theta_{az} = 0$

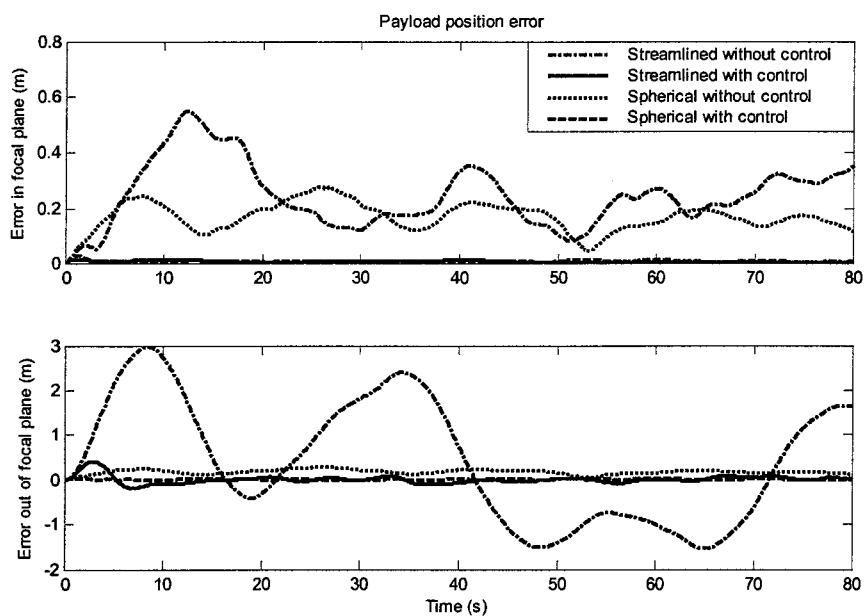


Figure 5.13 Payload position error for  $\theta_{zd} = \theta_{az} = 0$

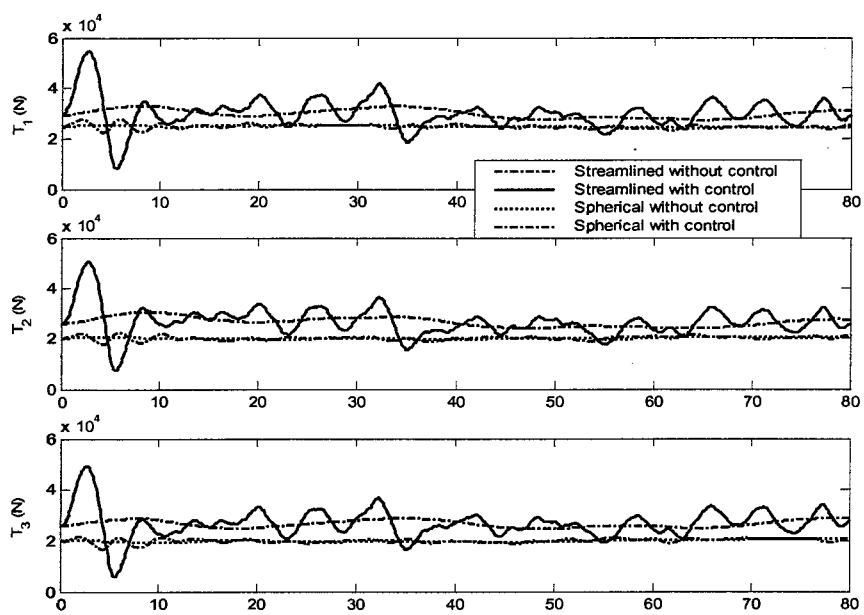


Figure 5.14 Tether tensions for  $\theta_{zd} = \theta_{az} = 0$

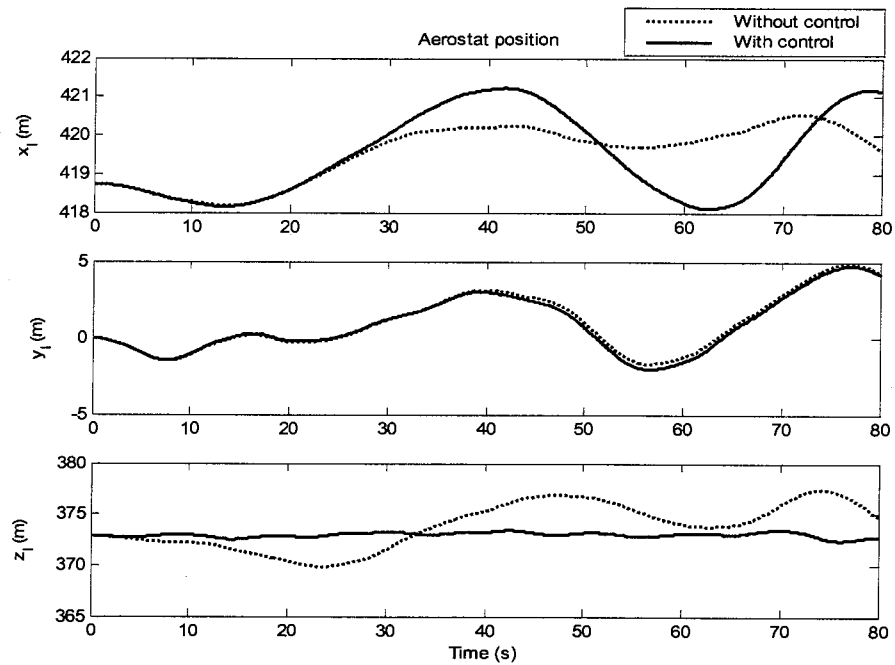


Figure 5.15 Aerostat translational motion for  $\theta_{za} = 60^\circ$ ,  $\theta_{az} = 0$

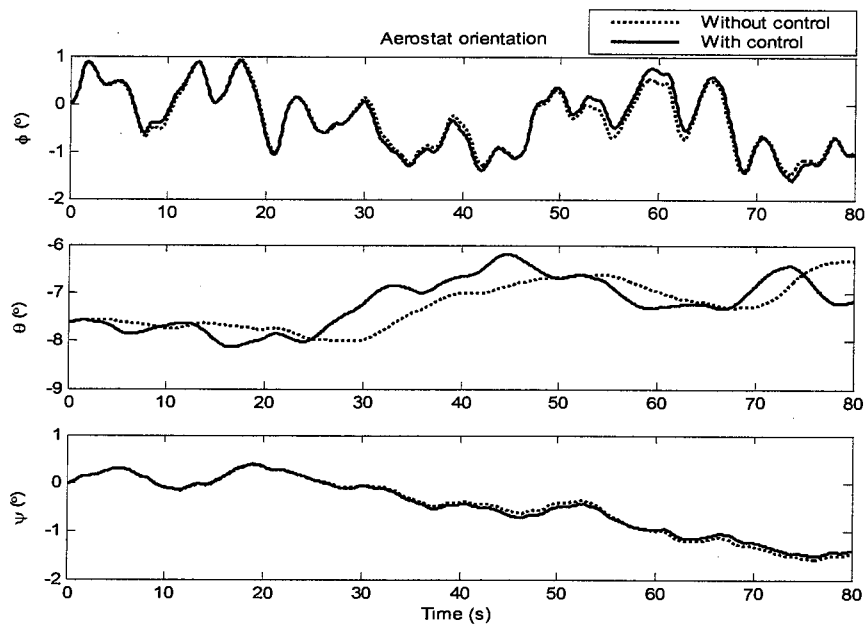
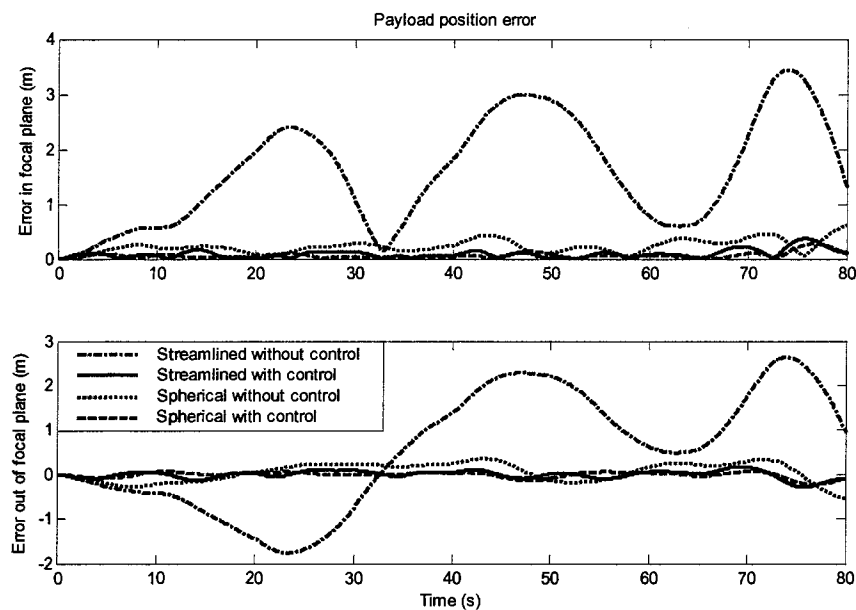
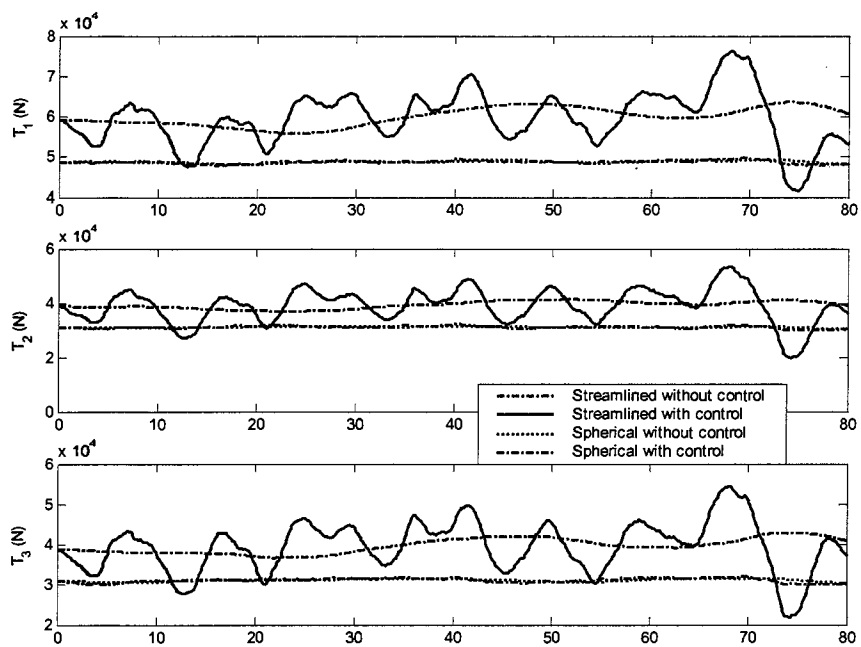


Figure 5.16 Aerostat rotational motion for  $\theta_{za} = 60^\circ$ ,  $\theta_{az} = 0$

Figure 5.17 Payload position error for  $\theta_{zd} = 60^\circ$ ,  $\theta_{ad} = 0$ Figure 5.18 Winch tensions for  $\theta_{zd} = 60^\circ$ ,  $\theta_{ad} = 0$

From the figures of aerostat motions (Figures 5.11, 5.12, 5.15, 5.16), we can see that the aerostat exhibits moderate lateral displacement, the maximum y-axis displacements are 6.1 m, and 4.7 m for  $(\theta_{za} = \theta_{az} = 0)$  and  $(\theta_{za} = 60^\circ, \theta_{az} = 0)$  respectively; the controller has little effect on the aerostat's lateral motions. By contrast, the payload position is effectively controlled, thus demonstrating the stiffness of the cable structure.

The tensions (Figures 5.14 and 5.18) in the uncontrolled cases with 10 m/s mean wind speed are slightly higher in magnitude compared to those in the spherical aerostat system although the net helium lifts of the two aerostats are close. The reason is that the hull and fins of the TCOM 71M aerostat provide extra lift to the system at a non-zero pitch angle which is around  $-7^\circ$  (nose up) in our cases. The tension variations are much bigger than those in the spherical aerostat system, due to the higher controller gains. It was found that higher gains had to be used to effectively control the payload positions. As mentioned earlier, the gains used for the system with the TCOM are  $k_d = 6$  s,  $k_p = 30$  and  $k_i = 3$  s $^{-1}$  for all cases, and those for the system with the spherical aerostat are  $k_d = 2$  s,  $k_p = 5$ ,  $k_i = 5$  s $^{-1}$  for  $\theta_{za} = \theta_{az} = 0$  and  $k_d = 4$  s,  $k_p = 1$ ,  $k_i = 1$  s $^{-1}$  for  $\theta_{za} = 60^\circ, \theta_{az} = 0$ . For the controlled system, the payload errors shown with the streamlined aerostat are similar in magnitude to those in the spherical aerostat system. The higher control gains indicate that the use of a streamlined aerostat requires more power to control the system under turbulence. The simulation results show that the maximum power is about 92 and 65 kW for  $(\theta_{za} = \theta_{az} = 0)$  and  $(\theta_{za} = 60^\circ, \theta_{az} = 0)$  respectively.

Lambert presented some vortex shedding study results in [32] with a one-third scale model of the LAR system with a spherical aerostat. His scaled system results showed that the system has lateral oscillations at a frequency at about 0.2 Hz. Results of

our simulation do not show such oscillations at all. This verifies that one of the advantages of the streamlined aerostat is that it does not introduce the oscillations typical of a spherical one.

## **Chapter 6   Conclusions**

### **6.1   Conclusions**

The research reported in this thesis dealt with the dynamics and control of a multi-tethered aerostat system. An existing statics model of the triple-tethered aerostat system developed by Fitzsimmons [23] was incorporated into the dynamics model developed by Nahon [24]. This provided a convenient means of obtaining an initial equilibrium for dynamics simulations. Some changes to the wind model and an improvement of the Jacobian matrix calculations were made in order to make the two models more consistent. There were minor differences in the way the cables were modelled in the statics and dynamics models. In the statics model, the mass is lumped at the center of the segments when discretizing, while in the dynamics model, it is lumped at the ends of the segments. Despite this difference, simulation results which were generated by starting the dynamics simulation from initial conditions obtained from the statics analysis demonstrated very good matches between the two models. This gave us confidence that both models are good representations of the system under study. The coalesced model was then used as a new base for further development of the multi-tethered aerostat system.



The model of the combined triple-tethered aerostat system was further developed to simulate a six-tethered aerostat system. As shown by Fitzsimmons [23], the use of six tethers allows a reduction of the tether base radius as well as the tether diameter. The study of the six-tethered system was divided into two topics: the redundantly actuated system using six tethers to control the payload platform position only, and the determinate system using six tethers to control both the position and orientation of the payload platform.

The redundancy in actuation gives us a statically indeterminate system in the statics solver. We used optimization techniques to obtain an optimum statics solution. Simulation results of the redundantly actuated system showed that we were able to achieve similar magnitude of payload position error between the statics model and the dynamics model for the six-tethered system. The dynamics simulation results showed that the six-tethered system is much stiffer than the triple-tethered system with much smaller payload position errors both with and without controllers.

The study of the determinate system raised some issues. We had difficulty in obtaining a static equilibrium for some cases. This may be due to the manner in which we break down the statics problem in order to fit into Fitzsimmons' existing structure. It may also be because of limitations of the system. Although we have six tethers to manipulate the six degrees of freedom of the payload platform, the orientation workspace may be quite limited. Due to the difficulty in obtaining a statics solution, we developed a compromise statics solution which neglects the moment balance of the payload platform. In the dynamics solution, PID winch controllers were used to control the desired positions of the top nodes of the tethers which include a consideration of the desired payload

platform position and orientation. The dynamics simulation showed that we can effectively control the position error of the payload platform, but have only a small effect on the orientation of the payload platform. Therefore, it may be undesirable to use the tethers to control the payload platform orientation. An orientation adjustment mechanism installed at the payload platform may be more practical.

The investigation of a streamlined aerostat was done to investigate the possible benefits of replacing the spherical aerostat in the original model. A streamlined aerostat TCOM71M which provides the same magnitude of lift to the system was modelled using a component breakdown method [38] and incorporated into the triple-tethered aerostat system. Results showed no oscillations which would be typical of a spherical aerostat present in the system. This indicates that a streamlined aerostat may perform better than a spherical one in some respects. We also found that the gains of the winch controllers had to be quite large in order to maintain the same magnitude of payload position errors as that of the system with a spherical aerostat in the presence of turbulence. This then implies we would need more power to control the system with a streamlined aerostat than with a spherical one.

## 6.2 Future Work

Suggested future research work would include the improvement of the winch controllers for the multi-tethered system. The current simulation uses simple PID controllers and the same gains for all winches. Since the lengths and tensions vary significantly between the tethers when the desired payload platform position changes, having different gains for each winch might achieve better system performance.

Investigation of adaptive model-based controllers might also be desirable for such a large-scale complex system. It is also recommended to have the vortex-induced oscillation effects included in the spherical aerostat model.

Actuation redundancy can also be exploited to make the system fail-safe. It would be interesting to simulate the failure of one of the tethers in the redundantly actuated system to evaluate the controllability and performance of the system in this case.

In the current determinate system model, the leash is attached to the center of mass of the payload platform, which implies it does not contribute to the moment balance of the payload platform. It may be worthwhile to investigate the potential benefits of different leash attachment points on the payload platform. It is recommended to move the leash attachment position away from the center of mass to investigate this configuration for the determinate six-tethered system. A rearrangement of the main tether attachments at the payload platform and/or on the ground could also be investigated. It would also be interesting to simulate the case with more than six tethers in the system. This would yield a redundantly actuated system for controlling both the position and orientation of the payload platform. It might lead to a better ability to control the payload orientations.

In the streamlined aerostat system, we were not able to obtain all necessary parameters of the aerostat we incorporated, and so some of them were estimated. It would be the best if we could have the accurate parameters for a streamlined aerostat for the simulation. Further work can also be done to study the reasons why higher gains were required to achieve good control accuracy of the payload platform position.

As is true for all simulations, validation is of great importance. Although this work has some degree of numerical validation, it would be of great benefit if an experimental system could be built to further validate the simulation results.

## Bibliography

- [1] The Square Kilometre Array Home Page, <http://www.skatelescope.org/>
- [2] "Memorandum of Agreement to Cooperate in a Technology Study Program Leading to a Future Very Large Radio Telescope", signed by participants from Australia, Canada, China, India, the Netherlands, the USA, <http://www.atnf.CSIRO.AU/SKA/archive/moa.html>
- [3] The web site of the National Radio Astronomy Observatory / Associated Universities, Inc. / National Science Foundation, <http://www.nrao.edu/>
- [4] T. H. Legg, "A proposed New Design for a Large Radio Telescope", *Astronomy & Astrophysics Supplement Series* 130, pp. 369-379, 1998.
- [5] The Large Adaptive Reflector Web Site at <http://www.drao.nrc.ca/science/ska/>
- [6] J. W. Leonard, *Tension Structures, Behaviour and Analysis*, McGraw-Hill, 1988.
- [7] B. Veidt and P. Dewdney, "Steady-State Stability Analysis of a Triple Tethered Balloon Platform", available at [http://www.drao.nrc.ca/science/ska/statics\\_report/](http://www.drao.nrc.ca/science/ska/statics_report/), Sept 1996
- [8] J. V. Sanders, "A Three-Dimensional Dynamic Analysis of a Towed System", *Ocean Engineering*, Vol. 9, No. 5, pp. 483-499, 1982.

- [9] T. S. Walton and H. Polacheck, "Calculation of Transient Motion of Submerged Cables", *Mathematics of Computation*, Vol. 14, No. 69, 1960, pp. 27-46.
- [10] J. W. Kamman, T. C. Nguyen, and J. W. Crane, "Modeling Towed Cable Systems Dynamics", *Proceedings of Oceans '89*, Published by IEEE Piscataway NJ USA, pp. 1484-1489, 1989.
- [11] B. Buckham, M. Nahon, and M. Seto, "Three-Dimensional Dynamics Simulation of a Towed Underwater Vehicle", *Proceedings of OMAE'99*, OMAE99/99-3068, 1999.
- [12] J. W. Kamman and R. L. Huston, "Modeling of Variable Length Towed and Tethered Cable Systems ", *Journal of Guidance, Control, and Dynamics*, Vol. 22, No. 4, pp. 602-608, 1999.
- [13] S. P. Jones and J. D. DeLaurier, "Aerodynamic Estimation Techniques for Aerostats and Airships", *Journal of Aircraft*, Vol. 20, No. 2, 1983.
- [14] H. J. Allen and E. W. Perkins, "A study of Viscosity on Flow Over Slender Inclined Bodies of Revolutions", NACA Rep. 1048, 1951.
- [15] M. M. Munk, "Aerodynamics of Airships", *Aerodynamic Theory*, Vol.6, W.F. Durand, Julius Springer, Berlin, pp. 32-48, 1936.
- [16] S. P. Jones and J. A. Krausman, "Nonlinear Dynamic Simulation of a Tethered Aerostat", *ALAA Journal of Aircraft*, Vol. 19, No. 8, pp. 679-686, 1982.
- [17] S. P. Jones, "Nonlinear Dynamic Simulation of a Moored Aerostat", AIAA-87-2505, 1987.
- [18] S. P. Jones and L. D. Schroeder, "Nonlinear Dynamic Simulation of a Tethered Aerostat: A Fidelity Study", AIAA-99-4325, 1999.

- [19] R. C. Leclaire and C. B. Rice, "The Local Motions of a Payload Supported by a Tri-tethered Natural Shape Balloon", *US Air Force Report AFCRL-TR-73-0748*, 1973.
- [20] R. C. Leclaire and H. L. Schumacher, "Local Motions of a Payload Supported by a Nolaro Tri-Tethered Balloon", *Proceedings of the Eighth AFCRL Scientific Balloon Symposium*, pp. 233-255, 1974.
- [21] C. H. K. Williamson and R. Govardhan, "Dynamics and Forcing of a Tethered Sphere in a Fluid flow", *Journal of Fluids and Structures*, Vol. 11, pp. 293-305, 1997.
- [22] R. Govardhan and C. H. K. Williamson, "Vortex-Induced Motions of a Tethered Sphere", *Journal of Wind Engineering and Industrial Aerodynamics*, Vol. 69-71, pp. 375-385, 1997.
- [23] J. Fitzsimmons, B. Veidt, and P. Dewdney, "Steady-State Stability Analysis of the Multi-Tethered Aerostat Platform for the Large Adaptive Reflector Telescope", *Proceedings of SPIE* Vol. 4015, pp. 476-487, 2000.
- [24] M. Nahon, "Dynamics and Control of a Novel Radio Telescope Antenna", AIAA-99-4120, 1999.
- [25] J. J. Craig, *Introduction to Robotics Mechanics and Control*, Addison Wesley, Second Edition, pp. 19-67, 1989.
- [26] M. Irvine, *Cable Structures*, Dover Publications, New York, pp. 16-20, 1992.
- [27] W. H. Press, S. A. Teukolsky, W. T. Vetterling, and Brian P. Flannery, *Numerical Recipes in C, The Art of Scientific Computing, Second Edition*, Cambridge University Press, 1992.

- [28] Y. Nakamura, *Advanced Robotics Redundancy and Optimization*, Addison Wesley, 1991.
- [29] T. Yoshikawa, *Foundations of Robotics, Analysis and Control*, The MIT Press, 1990.
- [30] C. Lawrence, J. L. Zhou, and A. L. Tits, "User's Guide for CFSQP Version 2.5: A C Code for Solving Constrained Nonlinear Optimization Problems, Generating Iterates Satisfying All Inequality Constraints", University of Maryland, College Park, MD, 1999.
- [31] AEM Design web site: <http://gachinese.com/aemdesign/>
- [32] C. M. Lambert, "Dynamics Modeling and Conceptual Design of a Multi-tethered Aerostat System", M.A.Sc. Thesis, Department of Mechanical Engineering, University of Victoria, 2002.
- [33] The LAR Group, "White Paper, the Large Adaptive Reflector Concept", available at: <http://www.skatelescope.org/documents/>, 2002
- [34] J. N. Newman, *Marine Hydrodynamics*, MIT press, 1977.
- [35] TCOM L.P. web site, <http://www.tcomlp.com/>
- [36] S. Badesha and S. P. Jones, "Aerodynamics of the TCOM 71M Aerostat", AIAA-93-4036-CP, 1993.
- [37] S. P. Jones, and L. D. Schroeder, "Nonlinear Dynamic Simulation of a Tethered Aerostat: A Fidelity Study", *ALAA Journal of Aircraft*, Vol. 38, No. 1, pp. 64-68, 2001.
- [38] M. Nahon, "A Simplified Dynamics Model for Autonomous Underwater Vehicle", *Proceedings of AUV'96*, pp. 373-379, 1996



- [39] J. D. DeLaurier, "A Stability Analysis for Tethered Aerodynamically Shaped Balloons", *AIAA Journal of Aircraft*, Vol. 9, No. 9, pp. 646-651, 1972.
- [40] L. H. Jorgensen, "Prediction of Static Aerodynamic Characteristics for Space-Shuttle-Like and Other Bodies at Angles of Attack from  $0^0$  to  $180^0$ ", NASA TN D-6996, 1973.
- [41] H. J. Allen, "Estimation of the Forces and Moments Acting on Inclined Bodies of Revolution of High Fineness Ratio", NACA RM A9I26, 1949.
- [42] B. W. McCormick, *Aerodynamics, Aeronautics and Flight Mechanics*, John Wiley & Sons, 1995.
- [43] R. S. Shevell, *Fundamentals of Flight*, Prentice Hall, 2nd Edition, 1989.
- [44] D. Hopkin, and V. den Hertog, "The Hydrodynamic Testing and simulation of an Autonomous Underwater Vehicle", *Proceedings of the Second Canadian Marine Dynamics Conference*, pp. 274-281, 1993.